Instabilities of finite-width internal wave beams

by

Boyu Fan

B.S., California Institute of Technology (2015)
S.M., Massachusetts Institute of Technology (2017)

Submitted to the Department of Mechanical Engineering
in partial fulfillment of the requirements for the degree of

Doctor of Philosophy in Mechanical Engineering

at the

MASSACHUSETTS INSTITUTE OF TECHNOLOGY

September 2020

Author . . . .
Department of Mechanical Engineering
July 21, 2020

Certified by . . . .
Triantaphyllos R. Akylas
Professor of Mechanical Engineering
Thesis Supervisor

Accepted by . . . .
Nicolas Hadjiconstantinou
Professor of Mechanical Engineering
Chairman, Department Committee on Graduate Theses

Instabilities of finite-width internal wave beams

by

Boyu Fan

Submitted to the Department of Mechanical Engineering
on July 21, 2020, in partial fulfillment of the
requirements for the degree of
Doctor of Philosophy in Mechanical Engineering

Abstract

Internal gravity waves are fundamental to the dynamics of density stratified fluids and the instability mechanisms by which these waves dissipate their energy are a potentially significant factor that underlies the distribution of energy and momentum in the natural environment. Recently, it has been recognized that internal waves in the oceans and atmosphere often take the form of beams: plane waves with locally confined spatial profile. While there is a large body of theoretical work concerning the instability of sinusoidal internal waves, instability mechanisms of beams are not yet fully understood. Although various nonlinear mechanisms have been proposed, it remains unclear which, if any, are dominant in the natural environment and under what circumstances. This thesis examines the instability of finite-width internal wave beams in order to extend the current understanding of internal wave instability into more realistic settings.

Part I of this thesis uses a combination of experimental and theoretical techniques to investigate finite-amplitude instabilities of beams. First, using a variant of the classical 'St. Andrew's Cross' experiment, whereby beams are generated using a harmonically oscillated horizontal cylinder, we present novel experimental observations of instability in large-amplitude internal wave beams. These results are compared against the predictions of linear stability analysis based on Floquet theory and reveal the competition between two- and three-dimensional instability mechanisms. Next, Floquet theory is used to investigate the well-known parametric subharmonic instability (PSI) for finite-width beams. Our findings show that frequency components typically ignored in standard analyses based on triad resonance are in fact crucial to the instability dynamics of fine-scale perturbations. The Floquet stability analysis also reveals that PSI is restricted to a finite range of perturbation wavenumbers and that a broadband instability dominates at large perturbation wavenumber. Furthermore, in the nearly inviscid limit, this broadband instability persists for small-amplitude beams that are not typically susceptible to PSI.

Part II focuses on the PSI of finite-width internal wave beams and investigates the role of background mean flows, which provide a more realistic setting for PSI in the natural environment. Using weakly nonlinear asymptotic theories, two types of internal wave beams are considered: nearly-monochromatic beams whose spatial profile consists of a sinusoidal carrier modulated by a locally confined envelope, and thin beams with general profile under the effects of Earth's rotation. In both cases, the presence of a uniform background mean flow has a stabilizing effect on PSI for finite-width beams, in contrast to the PSI of a purely sinusoidal plane wave where the background mean flow has no effect.

Thesis Supervisor: Triantaphyllos R. Akylas
Title: Professor of Mechanical Engineering

Acknowledgments

I am extremely fortunate and grateful to have had Professor Triantaphyllos Akylas as my thesis advisor. His insight and attention to detail are rare, even in academia, and his sense of style is inspiring. It has been under his humble guidance that I have gained the confidence to question all that is taken for granted in the search for truth.

Thomas Peacock, Karl Helfrich, and Takeshi Kataoka have been wonderful committee members and collaborators and great sources of mentorship and support. In particular, I would like to thank Professor Peacock for use of the experimental facilities and advice about the experimental set-up in Chapter 2, Rohit Supekar for guidance on the experimental methods in Chapter 2, and the NSF Graduate Research Fellowship for supporting the work in this thesis. Finally, Laura Canfield, Yadira Rivera, Lorraine Rabb, Leslie Regan, and the entire MechE Grad Office have been tremendously helpful for navigating graduate life.

My journey at MIT would not be complete without the fantastic company of my brothers- and sisters-in-arms: Rohit Supekar, Saviz Mowlavi, Suhyoun (Essie) Yu, Cameron McBride, Jerry Wang, Nisha Chandramoorthy, Margaux Filippi, and many more. I am also lucky to have been surrounded by many other wonderful friends in Cambridge and across the country and I look forward to what the future has in store for all of us.

My family is my source of strength. Mom, dad, and Ingrid, you keep me grounded and show me how to love life for all that it is. Amy, you constantly give me new perspectives and make me a better person with your love and patience.

To all my mentors, friends, and family, I could not have asked for a more fantastic first 26 years. Now that my education has finally come to a close, onto the next chapter!

Contents

1 General introduction 15

2 Finite-amplitude instabilities of thin internal wave beams: experiments and theory 17

2.1 Introduction 17
2.2 Experimental set-up 20
2.3 Stable vs. unstable beams: experimental observations 21
2.4 Stability analysis 26
2.5 Comparison of observations with Floquet analysis 28
    2.5.1 Instability dynamics 28
    2.5.2 Effects of beam amplitude and angle 30
2.6 Three-dimensional effects 31
    2.6.1 Perturbations with transverse variations 31
    2.6.2 Transverse beam variations and induced mean flows 32
2.7 Concluding remarks 34

3 Instabilities of finite-width internal wave beams: from Floquet analysis to PSI 37

3.1 Introduction 37
3.2 Floquet stability analysis 39
    3.2.1 General formulation 39
    3.2.2 Sinusoidal waves 41
    3.2.3 Locally confined beams 42
3.3 Floquet stability of beams with $\omega = 2f$ 43
    3.3.1 Results 43
    3.3.2 Floquet stability vs. near-inertial PSI 44
3.4 Small-amplitude limit of Floquet problem 46
    3.4.1 Preliminaries 46
    3.4.2 PSI regime 48
3.5 Near-inertial PSI 50
    3.5.1 Reduced eigenvalue problem 50
    3.5.2 Instability growth rates 52
    3.5.3 Instability dynamics 54
3.6 PSI of nearly monochromatic beams 56
    3.6.1 Reduced eigenvalue problem 56
    3.6.2 Comparison with Floquet analysis 57
    3.6.3 Instability for inclination angle $\theta \lesssim 43°$ 59

3.7 Broadband instability of small-amplitude beams 61
3.8 Concluding remarks 63

4 Effect of background mean flow on the PSI of nearly monochromatic internal wave beams 67
4.1 Introduction 67
4.2 Formulation 69
    4.2.1 Preliminaries 69
    4.2.2 Primary wave beam 70
    4.2.3 Subharmonic perturbations 71
    4.2.4 Additional frequency components 73
    4.2.5 Evolution equations 73
4.3 Stability eigenvalue problem 75
4.4 Results 76
4.5 Concluding remarks 78

5 Near-inertial PSI of internal wave beams in a background mean flow 81
5.1 Introduction 81
5.2 Formulation 82
    5.2.1 Preliminaries 82
    5.2.2 Primary wave beam 83
    5.2.3 Fine-scale perturbations 84
    5.2.4 Evolution equations 86
    5.2.5 Eigenvalue problem for $f \ll 1$ 87
5.3 Sinusoidal plane wave 88
5.4 Locally confined beam 89
5.5 Concluding remarks 91

6 Future directions 93

A Miscellaneous results 95
A.1 Eigenvalue problem symmetry for locally-confined beam 95
A.2 Nonlinear self-interaction terms with weak mean flow 95

List of Figures

2-1 Schematics of the experimental set-up. (*a*) Side and transverse view of the wave tank and horizontal cylinder. The cylinder is harmonically oscillated at frequency ω_0 and angle θ relative to the horizontal such that $\omega_0^2 = N^2 \sin^2 \theta$. The laser sheet is in the xy-plane at $z = 4.3$ cm. (*b*) Sketch of the uniform cylinder and (*c*) non-uniform cylinder used for the experiments. Dimensions are given in §2.2. (*d*) Sketch of the generated wave beams (in grey), which reflect off the free surface and tank bottom. The dotted-line box shows the PIV window, with the primary beam of interest propagating from the upper right to the bottom left. The beam-oriented coordinate system (ξ, η, ζ) is defined by the along-beam, cross-beam and transverse horizontal coordinates, respectively. 22

2-2 (*a*) Horizontal (x-) velocity for beam inclination angle $\theta = 45°$ and forcing amplitude $A/L = 0.45$ at $t = 8T_0$ after start of forcing. The grey box corresponds to the region around the cylinder that is masked out. (*b*) Same as (*a*) but for $A/L = 0.63$. (*c*) Theoretical beam profile used in the linear stability analysis of §2.5 to approximate the experimental beam in (*b*). (*d*) Same as (*a*) but at $t = 36T_0$ after start of forcing. (*e*) Same as (*d*) but for $A/L = 0.63$. (*f*) Time series of the horizontal velocity for $A/L = 0.45$ at the location marked with the cross in (*a*,*d*). The vertical lines indicate the times $t = 8T_0$ and $36T_0$. (*g*) Same as (*f*) but for $A/L = 0.63$ and at the location marked with the cross in (*b*,*e*). 23

2-3 (*a*) Spatially-averaged time frequency spectra for the experiments shown in figure 2-2. The dotted line corresponds to the stable case at $A/L = 0.45$ (figure 2-2*a*,*d*) while the solid line corresponds to the unstable case at $A/L = 0.63$ (figure 2-2*b*,*e*). The subharmonic frequencies $\omega_1/N = 0.26$ and $\omega_2/N = 0.45$ are labelled. (*b*) Experimentally measured horizontal velocity field from figure 2-2(*e*), filtered at $\omega_1/N = 0.26$. (*c*) Same as (*b*) but filtered at $\omega_2/N = 0.45$. (*d*) Time frequency spectrum of the fastest-growing Floquet mode. The vertical dotted line marks the primary wave frequency at ω_0/N. (*e*) Theoretically predicted spatial mode shape corresponding to the first peak (from the left) in the frequency spectrum in (*d*) at $\omega/N = 0.24$. (*f*) Same as (*e*) but for the second peak at $\omega/N = 0.47$. Dashed arrows in (*b*,*c*,*e*,*f*) indicate direction of phase propagation. Solid arrows in (*b*,*c*) indicate direction of group velocity $\boldsymbol{c}_g$. Velocity scale in (*e*,*f*) is normalized to have the same maximum velocity as in (*b*,*c*). 25

2-4 Phase diagram showing the dependence of the instability on the nondimensional beam amplitude U_0 and beam angle θ. (▲): experimental configurations where instability was visibly apparent; (+): experimental configurations where instability was not visibly apparent but small instability peaks could be seen in the time frequency spectrum; (○): stable configurations. Overlaid are contour lines of the (nondimensional) real growth rate $\sigma \equiv \max_{i,\mu} \mathrm{Re}(\lambda_i)$ as predicted by Floquet stability analysis. 31

2-5 Dependence of the instability growth rate σ on the dimensionless transverse wavenumber m as predicted by the Floquet analysis for beam angle (*a*) $\theta = 35°$, (*b*) $\theta = 45°$, (*c*) $\theta = 55°$; and dimensionless beam amplitude $U_0 = 0.15$ (dotted line), $U_0 = 0.20$ (dashed line), and $U_0 = 0.25$ (solid line). All growth rates are normalized by the two-dimensional ($m = 0$) growth rate. 32

2-6 Experimental mean horizontal velocity field at $t = 300$ s, obtained by filtering the horizontal velocity field around the zero-frequency. The uniform cylinder is used as forcing. (*a*) beam inclination angle $\theta = 35°$ and forcing amplitude $A/L = 0.72$, with $t = 300 \text{ s} \approx 26T_0$; (*b*) $\theta = 45°$ and $A/L = 0.54$, with $t = 300 \text{ s} \approx 32T_0$. In both cases, the primary wave beam has nondimensional maximum along-beam velocity $U_0 \approx 0.22$ measured 20 cm away from the cylinder, and did not exhibit any visible signs of instability. Contours of the horizontal velocity field of the primary wave beam at $\pm 1 \text{ mm s}^{-1}$ are plotted in the dotted lines. 33

2-7 Experimental velocity fields for beam inclination angle $\theta = 45°$ and forcing amplitude $A/L = 0.63$ using the uniform cylinder (*a*–*c*) and the non-uniform cylinder (*d*–*e*) at $t = 39T_0$, where T_0 is the forcing period. Plots (*a*,*d*) show the horizontal velocity field at $z = 4.3$ cm while (*b*,*e*) show the horizontal velocity field at $z = 14.3$ cm, closer to the lateral tank wall. Plots (*c*,*f*) show the mean horizontal velocity field at $z = 14.3$ cm obtained by filtering (*b*,*e*), respectively, around the zero-frequency. No significant vertical mean flows were observed. 35

3-1 (*a*) Schematic of uniform beam with frequency ω and inclination θ to the horizontal, in keeping with (3.3). The coordinate system (ξ, η, z) is defined by the along-beam, cross-beam and transverse directions, respectively. Dotted lines indicate the finite width of the beam and the arrows within show the along-beam velocity u_0. The perturbation wavevector $\boldsymbol{k}$ is inclined by the angle χ to η and by $\phi = \theta - \chi$ to the vertical y. (*b*) Beam profile (3.8) for $\epsilon = 0.1$. Solid, dashed and dotted lines correspond to the real part, imaginary part and $|U|$, respectively. 40

3-2 (a) Instability growth rates (scaled by the beam amplitude $\epsilon = 0.01$) predicted by the Floquet stability analysis as a function of the along-beam (ξ-) wavenumber μ of the perturbations, for primary beam profile (3.8), beam frequency $\omega = 0.1$, Coriolis parameter $f = 0.05$, and inviscid flow conditions ($\nu = 0$). (b) Time frequency spectrum of the fastest growing Floquet mode for $\mu = 2.4$, indicated in (a) by a vertical dashed line. Vertical dotted lines indicate the frequencies $\pm f/\omega$. (c) and (d) Same as (b) but for $\mu = 8.6$ and 17, respectively. (e) Spatial mode shapes for the top four frequencies, in order of power, of the frequency spectrum plotted in (b) for the Floquet mode at $\mu = 2.4$. From left to right, plots are shown in order of decreasing power. The spatial mode amplitudes have been normalised such that the mode corresponding to the top frequency component has maximum along-beam velocity equal to unity. The peak cross-beam (η-) wavenumber γ of each mode is listed along with the frequency. (f) Same as (e) but for the top four frequencies, in order of power, of the frequency spectrum plotted in (c) for the Floquet mode at $\mu = 8.6$. 45

3-3 Comparison of predicted instability growth rates (in terms of the scaled time $T = \epsilon t$) as a function of the scaled perturbation wavenumber κ between the near-inertial PSI theory (using beam profile (3.33)) and the Floquet analysis (using beam profile (3.8) with beam amplitude $\epsilon = 0.002$) for primary beam frequency $\omega = 0.1$. Results are shown for viscous parameter (a,c) $\alpha = 0$ corresponding to inviscid flow, and (b,d) $\alpha = 10^{-3}$. (a,b) show results for detuning parameter $\hat{\sigma} = 0$ (●, solid line), $\hat{\sigma} = 4$ (△, dashed line), $\hat{\sigma} = 10$ (□, dashed-dotted line), and $\hat{\sigma} = 20$ (◊, dotted line). (c,d) show results for $\hat{\sigma} = 0$ (●, solid line), $\hat{\sigma} = -2$ (×, dashed line), $\hat{\sigma} = -4$ (∗, dashed-dotted line). In all plots, shapes correspond to the Floquet growth rate while lines correspond to the near-inertial PSI growth rate. 53

3-4 Maximum instability growth rate as function of detuning $-6 \leq \hat{\sigma} \leq 20$ for the same primary beam as in figure 3-3. (a) Inviscid flow conditions ($\alpha = 0$). In this case, since the maximum growth rate for a given $\hat{\sigma}$ occurs as $\kappa \to \infty$ (see figure 3-3a,c), results are presented for the near-inertial PSI growth rate at $\kappa = 12$ (solid line) and $\kappa = 100$ (dotted line). Floquet results (○) are shown at $\kappa \approx 12$. (b) Viscous flow conditions ($\alpha = 10^{-3}$). In this case, since the maximum growth rate is achieved at finite κ (see §3.5.2), plotted growth rates correspond to the maximum over all κ. Solid line is the near-inertial PSI growth rate, while (○) is the Floquet growth rate. 54

3-5 Inviscid instability growth rate as a function of the scaled perturbation wavenumber κ predicted by the Floquet analysis for beam amplitude $\epsilon = 0.002$ (○), 0.01 (△), 0.05 (□), 0.1 (◊). The same primary beam profile and frequency as in figure 3-3 and 3-4 are used here. Plots correspond to detuning parameter $\hat{\sigma} = -4$ (a), $\hat{\sigma} = 0$ (b), and $\hat{\sigma} = 20$ (c). The results for $\hat{\sigma} = 0$ in (b) include Floquet growth rates for $\epsilon = 0.2$ (∗). Solid lines correspond to the near-inertial PSI growth rate. 55

3-6 Time-frequency spectra of the fastest-growing Floquet mode found at scaled perturbation wavenumber $\kappa = 10$ for the same primary beam profile and frequency used throughout §3.5. Top row show modes for beam amplitude $\epsilon = 0.05$ while bottom row shows modes for $\epsilon = 0.002$. Left, middle and right columns correspond to detuning parameter $\hat{\sigma} = -4, 0$ and 20, respectively. The vertical dotted lines indicate the frequencies $\pm f/\omega$. 56

3-7 Beam profile (3.42) for nondimensional amplitude $\epsilon = 1$ and (*a*) $N = 1$ and (*b*) $N = 7$, where N corresponds to the number of carrier wavelengths contained within the beam width. Solid lines indicate the real part, while dotted lines indicate the imaginary part. 58

3-8 (*a*) Computed instability growth rates (in terms of the scaled time $T = \epsilon t$) according to the Floquet stability analysis as a function of N, the number of carrier wavelengths contained in the beam width, for the profile (3.42) with viscosity $\nu = 10^{-5}$, beam frequency $\omega = \sin 45°$, and beam amplitudes $\epsilon = 0.025$ ($\triangledown$), 0.05 ($\circ$), 0.1 ($\Diamond$), 0.2 ($\Box$), and 0.4 ($\triangle$). The corresponding asymptotic PSI growth rates, as predicted by (3.39), are overlaid and labelled. The PSI growth rate for a sinusoidal wave (i.e. $N \to \infty$) is indicated by the horizontal dashed line. (*b*) Minimum amplitude ϵ_c for instability as a function of N for $\nu = 5 \times 10^{-4}$ ($\triangleright$, solid line), 10^{-3} ($*$, dashed line), and 2×10^{-3} ($\triangleleft$, dotted line). Shapes correspond to Floquet analysis results while lines correspond to the amplitude threshold (3.43) predicted by the PSI theory. . . 60

3-9 Time-frequency spectra of the fastest-growing Floquet mode for various configurations shown in figure 3-8(*a*). Top and bottom rows correspond to beam amplitude $\epsilon = 0.2$ and 0.05, respectively. Left, middle and right columns correspond to $N = 2$, 10 and 20. Vertical dotted lines in each plot correspond to the frequencies $\pm\omega/2$. 60

3-10 Instability growth rate predicted by the Floquet stability analysis ($\circ$) as a function of the along-beam (ξ-) wavenumber μ of the perturbation, for the beam profile (3.42) with beam frequency $\omega = 0.4$ (i.e. beam inclination angle $\theta \approx 23.6°$), amplitude $\epsilon = 0.1$, viscosity $\nu = 0$, and $N = 20$ wavelengths of the carrier contained in the beam width. The corresponding growth rates for a sinusoidal wave as predicted by Floquet analysis under the same conditions are plotted as the solid line. The vertical dashed line at $\mu \approx 0.62$ indicates the point at which the most unstable perturbations to the sinusoidal wave transitions between the 'branch-C'-like instability (for $\mu \lesssim 0.62$), where one subharmonic frequency component of the perturbation has larger wavelength than the primary wave, and the PSI-like instability (for $\mu \gtrsim 0.62$), where both subharmonic frequency components have smaller wavelength than the primary wave. 62

3-11 (*a*) Floquet growth rate ($\bullet$) as a function of the perturbation wavenumber magnitude k using beam profile (3.8) for beam amplitude $\epsilon = 0.01$, primary beam frequency $\omega = 0.1$ and no background rotation ($f = 0$) under inviscid flow conditions ($\nu = 0$). The Floquet growth rate for $f = 0.05$ ($\circ$) and the asymptotic near-inertial PSI growth rate (solid line) are plotted for comparison. Vertical dashed lines indicate the values $k = 80, 200$ and 400. (*b*) Time-frequency spectra of the most unstable Floquet mode for $f = 0$ shown in (*a*) at $k = 80$. Vertical dashed lines indicate the frequencies $\omega_p = \pm\omega/2$. (*c*) Same as (*b*) but at $k = 200$. (*d*) Same as (*b*) but at $k = 400$. 64

3-12 Effect of viscosity on the Floquet growth rates shown in figure 3-11(*a*) using the same beam profile (3.8), beam amplitude $\epsilon = 0.01$ and primary beam frequency $\omega = 0.1$, for $\alpha = 10^{-3}$ ($\blacktriangle, \triangle$) and $\alpha = 0$ ($\bullet, \circ$). Filled shapes ($\bullet, \blacktriangle$) correspond to growth rates for $f = 0$, while open shapes ($\circ, \triangle$) correspond to results for $f = 0.05$ (i.e. near-inertial conditions). 64

4-1 Schematic of the PSI geometry. (*a*) Nearly monochromatic primary wave beam of frequency ω_0 in the presence of a background mean flow $\overline{u}$. The carrier wavevector $\boldsymbol{k}_0 = \hat{\boldsymbol{e}}_\eta$ is inclined to the vertical by θ, determined by the Doppler shifted dispersion relation (4.4). Thin solid lines indicate lines of constant phase (e.g. crests) of the carrier with Λ_* as the dimensional carrier wavelength, while thick solid lines indicate the finite extent of the envelope. According to (4.5), due to the mean flow, the modulation coordinate H is inclined to the vertical by an angle Θ different from θ. (*b*) Subharmonic perturbations are short-scale wavepackets with lines of constant phase (dashed lines) inclined to the horizontal by the angle ϕ given by (4.12). 71

4-2 Eigenvalues and growth rates for the top-hat profile with $\theta = \pi/4$, $\epsilon = 0.3$, $\nu = 0.004$, and $D = 5$. When varying $\overline{u}$, the beam inclination angle θ was fixed. (*a*) Plot of the real eigenvalue branches $\hat{\lambda}_r(\kappa)$ for $\overline{u} = 0$ (thin lines), as well as the cubic $\alpha D\kappa^3/c$ (thick line) that controls viscous dissipation. Instability arises if $\hat{\lambda}_r > \alpha D\kappa^3/c$. (*b*) Same as (*a*), but for $\overline{u} = 0.2$. (*c*) Range of unstable wavenumbers (shaded in dark gray) as $\overline{u}$ is varied. The wavenumber with the maximum growth rate is indicated by the thick black line. The corresponding range for $\nu = 0$ is shown in light gray (which completely contains the dark gray region), with maximum growth rate locus indicated by the dotted line. (*d*) Plot of the maximum PSI growth rate $\lambda_{\max}$ as function of $\overline{u}$. The corresponding growth rates for $\nu = 0$ are plotted with the dotted line. 78

5-1 Schematic of the PSI geometry. (*a*) Locally confined primary wave beam of general profile with frequency ω_0 and $O(1)$ width in the presence of a small background mean flow $\overline{u}$. According to (5.5), the beam profile will feature slow variations in ξ. (*b*) Close-up view of the beam slice shown in the dotted box in (*a*). The beam geometry at any given ξ-location can be assumed to be uniform along ξ since ξ-variations have a much longer length scale than η-variations. Subharmonic perturbations with frequency $\omega_0/2$ are taken to have short vertical scale and have nearly horizontal lines of constant phase (dotted lines) since they are near-inertial. 85

5-2 Real part of the stability eigenvalues $\hat{\lambda}_r$, corresponding to the inviscid PSI growth rate, for the locally confined beam profile (5.27) as a function of the scaled perturbation wavenumber κ for $\overline{u} = 0$ ($\circ$), 0.5 ($\square$), and -1 ($*$). The dashed line plots the quadratic $\alpha\kappa^2$ for $\alpha = 0.1$. 90

5-3 (*a*) Maximum inviscid ($\alpha = 0$) PSI growth rate λ_r for the locally confined beam profile (5.27) as a function of $\overline{u}$ for $\sigma = -4$ ($*$), 0 ($\circ$), and 10 ($\square$). (*b*) Same as (*a*) but for $\alpha = 0.1$. (*c*) Same as (*a*) but for $\alpha = 0.5$. 90

5-4 (*a*) Maximum inviscid ($\alpha = 0$) PSI growth rate λ_r for the locally confined beam profile (5.27) as a function of σ for $\overline{u} = 0$ ($\circ$), -1 ($\triangle$), -2 ($\square$), -3 ($\Diamond$), and -4 ($\times$). (*b*) Same as (*a*) but for $\alpha = 0.1$. (*c*) Same as (*a*) but for $\alpha = 0.5$. 90

THIS PAGE INTENTIONALLY LEFT BLANK

Chapter 1

General introduction

Internal gravity waves are fundamental disturbances that arise in density stratified fluids such as the oceans or atmosphere. Owing to the natural anisotropy of such fluids, with gravity providing a preferred direction, internal waves exhibit a variety of interesting properties, the most famous of which is their unique linear dispersion relation

$$\frac{\omega}{N} = \sin\theta, \tag{1.1}$$

which relates the frequency ω of a sinusoidal wave, normalized by the buoyancy frequency N that characterizes the background density stratification, and the angle θ that the wavevector makes with the vertical, but is entirely independent of the magnitude of the wavevector.

As internal waves propagate through the interior of a fluid, they are key contributors to the underlying distribution of energy and momentum in the natural environment. Therefore, the instability mechanisms by which these waves dissipate their energy are of great physical relevance. While there is a large body of theoretical work concerning the instability of sinusoidal internal waves, recently, it has been recognized that internal waves in the oceans and atmosphere instead often take the form of beams, plane waves with locally confined spatial profile, whose instability mechanisms are not yet fully understood. There has been some progress detailing various nonlinear mechanisms by which beams undergo instability, but it still remains unclear which, if any, are dominant in the natural environment and under what circumstances. Therefore, the unifying aim of this thesis is to advance the understanding of internal wave instability in physically relevant settings.

This thesis is divided into two parts, corresponding to two central themes. Part I, consisting of Chapters 2 and 3, focuses on the instability dynamics of finite-width beams beyond the small-amplitude limit. Chapter 2 uses a combination of experimental and theoretical techniques to investigate internal wave beams whose spatial profile features no more than a single wavelength. Using a variant of the classical 'St. Andrew's Cross' experiment, whereby beams are generated using a harmonically oscillated horizontal cylinder, we present novel experimental observations of instability, which bears resemblance to the triadic resonant instability (TRI) of sinusoidal internal waves but is fundamentally distinct from TRI. The experimental observations agree well with linear stability computations based on Floquet theory, and evidence is presented that the presence of three-dimensional effects, in the form of transverse beam variations, induce a horizontal mean flow of the streaming type and greatly subdue the instability.

Chapter 3 uses Floquet theory to investigate finite-amplitude instabilities of finite-width beams in relation to the well-known parametric subharmonic instability (PSI). Results of the Floquet analysis are compared with previous weakly nonlinear models of PSI and show that frequency components typically ignored in standard analyses based on triad resonance are in fact crucial to the instability dynamics of fine-scale perturbations. After accounting for these components, the asymptotic PSI analysis is in excellent agreement with numerical solutions of the Floquet eigenvalue problem. The Floquet stability analysis also reveals that PSI is restricted to a finite range of perturbation wavenumbers: as the perturbation wavenumber is increased (for fixed beam amplitude), higher-frequency components eventually come into play so the instability becomes broadband. Furthermore, in the nearly inviscid limit, this broadband instability persists for small-amplitude beams that are not typically susceptible to PSI.

Part II, consisting of Chapters 4 and 5, considers PSI of finite-width internal wave beams under the influence of a background mean flow. Chapter 4 describes an asymptotic model for the PSI of a nearly monochromatic internal wave beam, whose spatial profile features a sinusoidal carrier modulated by a locally confined envelope. As a result of the background mean flow, an additional necessary condition for PSI emerges that stabilizes very short-scale perturbations and allows for a small amount of mean flow to weaken PSI dramatically. This is in contrast to the PSI of a purely sinusoidal wave, for which a background mean flow has no effect.

Finally, Chapter 5 considers the effect of a background beam flow on the near-inertial PSI of finite-width beams, in which the primary wave frequency is approximately twice that of the background rotation rate. In a similar fashion to the results of Chapter 4, the presence of a uniform background mean flow generally has a stabilizing effect on PSI for finite-width beams. However, under near-inertial conditions, it is possible for small amounts of mean flow, depending on its direction in relation to the primary wave, to induce PSI in beams that would have otherwise been stable in the absence of mean flow.

Chapter 2

Finite-amplitude instabilities of thin internal wave beams: experiments and theory

This work has been submitted to *Journal of Fluid Mechanics.*

2.1 Introduction

The classic experiment by Mowbray & Rarity (1967) of oscillating a cylinder in a stratified fluid was the first demonstration of the remarkable X-shaped pattern of internal gravity waves that is now known as 'St. Andrew's Cross'. Interestingly, the four arms of the cross are in the form of time-harmonic plane waves with locally confined spatial profile, determined by the oscillating cylinder, and stretch along specific directions relative to gravity set by the dispersion relation. Such beam-like disturbances are fundamental propagation modes that derive from the inherent anisotropy of internal wave motion, whereby energy is transported along rather than perpendicularly to surfaces of constant phase (e.g. Lighthill, 1978, §4.4). Since the original observations of Mowbray & Rarity (1967), there have been numerous experimental and theoretical investigations of internal wave beams in connection with forced internal waves by oscillating bodies and related configurations (see e.g. Kataoka *et al.*, 2017, and references therein). Furthermore, internal wave beams arise in oceans due to the interaction of the barotropic tide with bottom topography (e.g. Lamb, 2004; Peacock *et al.*, 2008; Johnston *et al.*, 2011) and in the atmosphere due to thunderstorms (e.g. Fovell *et al.*, 1992).

In an effort to shed light on the dissipation process of oceanic internal waves, a body of recent work has focused on possible instability mechanisms of internal wave beams (see e.g. Dauxois *et al.*, 2018, and references therein). Theoretically, the stability of wave beams can be viewed as an extension of the simpler, but less realistic problem of the stability of plane waves with sinusoidal profile. The latter problem has been studied systematically using Floquet theory, and a wide range of instabilities have been found for finite-amplitude sinusoidal waves (e.g. Mied, 1976; Klostermeyer, 1991; Sonmor & Klaassen, 1997). In the small-amplitude limit, these instabilities can be understood in terms of resonant triad interactions of the primary wave with two subharmonic perturbations (e.g. Staquet & Sommeria, 2002). A particular case of such triadic resonant instability (TRI) is the widely-studied parametric subharmonic instability (PSI), which involves subharmonic perturbations with half the frequency of the primary wave and very fine wavelength. In view of the possibility of transferring energy into much smaller scales, PSI has been suggested as a potentially significant factor in the dissipation of oceanic internal waves (e.g. Hibiya *et al.*, 2002; MacKinnon & Winters, 2005; Young *et al.*, 2008).

It is now recognized, however, that the finite width of an internal wave beam reduces the efficiency of PSI: subharmonic perturbations travel across the beam with their group velocity and thus have only limited time to extract energy from the primary wave. On these grounds, Karimi & Akylas (2014) argued that, in the small-amplitude nearly-inviscid limit, only beams with nearly monochromatic profile are susceptible to PSI. This possibility of PSI, which requires that the beam profile comprise large enough number of carrier wavelengths, is further limited by background mean flows (Fan & Akylas, 2019). An exception arises in the presence of background rotation for beams with frequency close to twice the inertial frequency. In this instance, which is of geophysical relevance, owing to the Earth's rotation, beams with general locally confined profile can suffer PSI because subharmonic perturbations of near-inertial frequency have group velocity close to zero (Karimi & Akylas, 2017). These conclusions regarding PSI of small-amplitude nearly-inviscid beams were confirmed by a formal linear stability analysis (Fan & Akylas, 2020*b*) using the Floquet procedure of Onuki & Tanaka (2019). In addition, however, Fan & Akylas (2020*b*) found that small-amplitude beams with general locally confined profile can develop instability far away from the inertial frequency. This instability, similar to PSI, arises in the limit of large perturbation wavenumber and is thus viable only in very high Reynolds-number environments. Furthermore, it involves not only two subharmonic perturbations, but also higher harmonics due to interactions with the underlying beam.

On the experimental side, Bourget *et al.* (2013) examined the stability of wave beams of finite width comprising about three wavelengths of a well-defined carrier, which were generated in a stratified fluid tank by a stacked-plate wavemaker (Mercier *et al.*, 2010) specially designed for this purpose. Owing to the increased importance of viscosity under laboratory flow conditions, rather than PSI, which involves perturbations of very fine spatial scale, Bourget *et al.* (2013) observed a form of TRI: the two unstable subharmonic perturbations formed a resonant triad with the beam carrier but the three waves had comparable wavelengths. Furthermore, in a follow-up study using a similar set-up, Bourget *et al.* (2014) confirmed that the finite beam width weakens this triad resonance instability, consistent with Karimi & Akylas (2014). In an earlier experiment, however, using a similar wave generator, but in a relatively wide tank where the generated nearly monochromatic beams featured significant transverse variations, Bordes *et al.* (2012) found no evidence of TRI. Instead, they observed a growing horizontal mean flow of the streaming type which also impacts the beam itself via refraction. This induced mean flow is of viscous origin and hinges on the combined effects of transverse variations and nonlinearity (Kataoka & Akylas, 2015; Fan *et al.*, 2018; Jamin *et al.*, 2020). However, as noted by Dauxois *et al.* (2018), it is unclear whether streaming and TRI can coexist, and the conditions that would favour one over the other remain largely unexplored.

In contrast to nearly monochromatic beams, there have been only few reports of instability in the original St. Andrew's Cross, which features internal wave beams whose typical width is only one or two wavelengths. Importantly, such 'thin' beams with a broadband spectrum of spatial wavenumbers are not only readily generated in the laboratory by oscillating bodies, but also typify beams that arise in oceans and the atmosphere (e.g. Fovell *et al.*, 1992; Lamb, 2004; Johnston *et al.*, 2011). Most prior laboratory experiments that used an oscillating cylinder as forcing, in particular, were concerned with small-amplitude beams. Specifically, the typical ratio of oscillation amplitude (half peak-to-peak) to cylinder radius was less than 0.2, and the generated beams agreed well with linear theory (e.g. see Sutherland & Linden, 2002). Thus, considering the theoretical findings of Karimi & Akylas (2014) and Fan & Akylas (2020*b*) for small-amplitude thin beams, it is not surprising that no instabilities have been observed under these laboratory flow conditions. At a larger amplitude-to-radius ratio of 0.66, Clark & Sutherland (2010) report an instability that resembles PSI, but experimental limitations of their synthetic schlieren technique precluded detailed quantitative measurements regarding this instability. Finally, Ermanyuk & Gavrilov (2008) used amplitude-to-radius ratios of up to 1.2. However, they did not observe instability probably because of the large viscous effects introduced by their small cylinder radius of 1 cm. The only significant nonlinear effect noted in this study was the radiation of a second-harmonic beam when the cylinder driving frequency is less than half the buoyancy frequency.

Apart from the St. Andrew's Cross, thin internal wave beams arise also in the so-called 'internal wave attractor' (e.g. Hazewinkel *et al.*, 2008; Scolan *et al.*, 2013; Brouzet *et al.*, 2016), which forms by the focusing of wave energy via wall reflections. In this setting, there have been observations of an instability of thin beams that appears to resemble TRI (i.e. satisfy the triad resonance conditions in an approximate sense). However, it remains unclear whether the observed instability can be predicted using TRI theory, which was originally developed for small-amplitude sinusoidal waves, and whether this instability persists outside of the strict geometric constraints of the attractor set-up.

The present joint experimental and theoretical investigation aims to improve the current understanding of instability mechanisms of isolated thin internal wave beams, akin to those originally observed by Mowbray & Rarity (1967). Specifically, we experimentally study internal wave beams due to a horizontal cylinder that is oscillated harmonically in the direction of propagation of the generated beam. This forcing arrangement permits the generation of coherent, finite-amplitude wave beams, which are then measured using particle image velocimetry. We present novel observations of instability above a threshold forcing amplitude-to-radius ratio depending on the driving frequency, which are compared against the predictions of a formal linear stability analysis based on Floquet theory. Although it bears resemblance to TRI, the observed instability cannot be predicted by TRI theory since thin wave beams have no well-defined carrier wavevector. This is in contrast to the Floquet stability analysis, which agrees well with the experimental observations. Finally, we present experimental evidence that transverse beam variations induce a horizontal mean flow of the streaming type and significantly weaken the observed instability.

2.2 Experimental set-up

Laboratory experiments were performed in a glass wave tank 5.46 m long and 0.51 m wide, filled to a depth of 0.54 m with salt water. Using the double-bucket method, a linear density stratification was set up with buoyancy frequency $N = 0.94\ \mathrm{s}^{-1}$. The final stratification was measured using a Precision Measurements Engineering conductivity/temperature probe. Waves were generated by oscillating a 0.5 m long horizontal cylinder (see schematic in figure 2-1) whose length spanned the transverse width of the tank with about 5 mm clearance between the ends of the cylinder and the tank walls on each side. Two thin metal rods attached to opposing ends of the cylinder were connected to a National Instruments/Axis New England based motion control system, which used a lead screw traverse to drive the cylinder oscillations. Cylinders were 3D printed using ABS plastic, allowing for precise control of the cylinder diameter along its length. We used two types of cylinders: (i) a uniform cylinder with radius 22.2 mm (figure 2-1*b*); and (ii) a non-uniform cylinder comprised of three cylindrical sections of equal length whose radii were 15.6 mm, 22.2 mm and 15.2 mm (figure 2-1*c*). We shall use $L = 22.2$ mm, the common radius in the centre section of the two types of cylinders, as the characteristic length scale for all experiments.

Cylinders were harmonically oscillated at angle θ to the horizontal with frequency ω_0 and half peak-to-peak amplitude A (figure 2-1*a*). For each experiment, θ was chosen to match the angle of inclination to the horizontal of the generated wave beams (see figure 2-1*d*), set by the linear dispersion relation

$$\omega_0^2 = N^2 \sin^2 \theta. \tag{2.1}$$

This arrangement allows for complete forcing of the fluid velocity in two of the four generated beams, since the motion of the cylinder is then exactly parallel to the direction of fluid motion. Our interest centres on one of these two preferentially excited beams (see figure 2-1*d*), which reach higher amplitude as compared to the four symmetric beams that would be generated by vertical ($\theta = 90°$) cylinder oscillations at the same forcing amplitude A. We note that an analogous result was found by Mercier *et al.* (2010) in their analysis of the forcing efficiency of a wavemaker comprised of stacked plates. In our experiments, $\theta \in \{35°, 40°, 45°, 50°, 55°\}$ and $0.36 \leq A/L \leq 1.26$. For all these forcing conditions, the wave beam amplitudes were below the threshold for overturning (see §2.5.2). Finally, the size of our wave tank was large enough to ensure that reflections of the other three beams from the tank walls and free surface do not interfere with the primary beam of study.

Flow visualization was performed using a LaVision particle image velocimetry (PIV) system. A pulsed Nd:YAG laser located beneath the wave tank was used to generate a vertical laser sheet in the xy-plane located at $z = 4.3$ cm (unless otherwise noted), where $z = 0$ specifies the midline of the tank (see figure 2-1a). The density stratification was seeded with Sphericel hollow glass oxide particles of diameter 8-12 μm and densities ranging from 1000 to 1050 kg m^{-3}. Images were captured using an Imager Pro X CCD camera at a resolution of 2048 × 2048 pixels from the start of forcing to 8 to 20 minutes later. The camera frame rate was 8 Hz, which corresponds to a minimum of 64 images per forcing period for the range of forcing frequencies used. Images were processed using LaVision DaVis software to obtain two-dimensional velocity fields in the plane of the laser sheet.

2.3 Stable vs. unstable beams: experimental observations

Figure 2-2 compares the horizontal (x-) velocity field of the internal wave beam generated using the uniform cylinder for $\theta = 45°$ at two forcing amplitudes, $A/L = 0.45$ and 0.63. For both amplitudes, at $t = 8T_0$ after start of forcing (figure 2-2a,b), where $T_0 = 2\pi/\omega_0$ is the oscillation period, the wave beam has propagated across the observation window from the upper right to the lower left (phase traveling from lower right to upper left) and has reached a quasi-steady state. At the later time $t = 36T_0$, the lower-amplitude beam (at $A/L = 0.45$) remains uniform in the along-beam direction aside from the effects of viscous dissipation, which cause slight broadening and decay of the wave profile far from the cylinder (figure 2-2d), and this steady state persisted even for larger times, e.g. $t = 120T_0$, with no noticeable instability. In contrast, at the larger forcing amplitude $A/L = 0.63$ after $36T_0$ of forcing, an instability is visibly apparent (figure 2-2e), causing breakdown of the primary wave beam. These observations are also consistent with a time series of the horizontal velocity at a position along the beam centreline roughly 20 cm away from the cylinder: the lower-amplitude forcing produces a steady time-harmonic signal (figure 2-2f), while the higher-amplitude forcing eventually results in a modulated, multi-frequency signal due to instability (figure 2-2g).

Figure 2-3(a) compares the spatially-averaged frequency spectra of the stable and unstable beams, obtained by calculating the time-frequency spectrum at each spatial point and averaging over the region of the primary wave beam. Both spectra feature a domi-

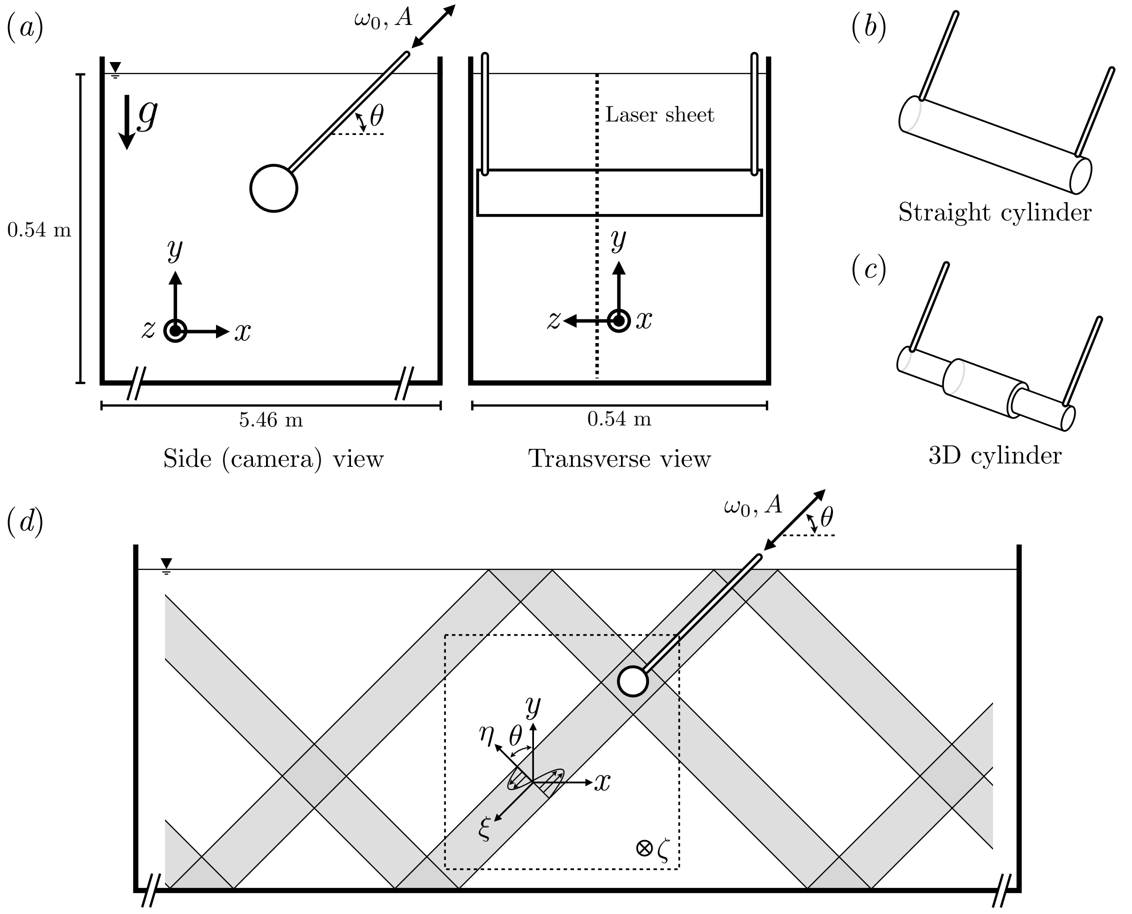

Figure 2-1: Schematics of the experimental set-up. (*a*) Side and transverse view of the wave tank and horizontal cylinder. The cylinder is harmonically oscillated at frequency ω_0 and angle θ relative to the horizontal such that $\omega_0^2 = N^2 \sin^2\theta$. The laser sheet is in the xy-plane at $z = 4.3$ cm. (*b*) Sketch of the uniform cylinder and (*c*) non-uniform cylinder used for the experiments. Dimensions are given in §2.2. (*d*) Sketch of the generated wave beams (in grey), which reflect off the free surface and tank bottom. The dotted-line box shows the PIV window, with the primary beam of interest propagating from the upper right to the bottom left. The beam-oriented coordinate system (ξ, η, ζ) is defined by the along-beam, cross-beam and transverse horizontal coordinates, respectively.

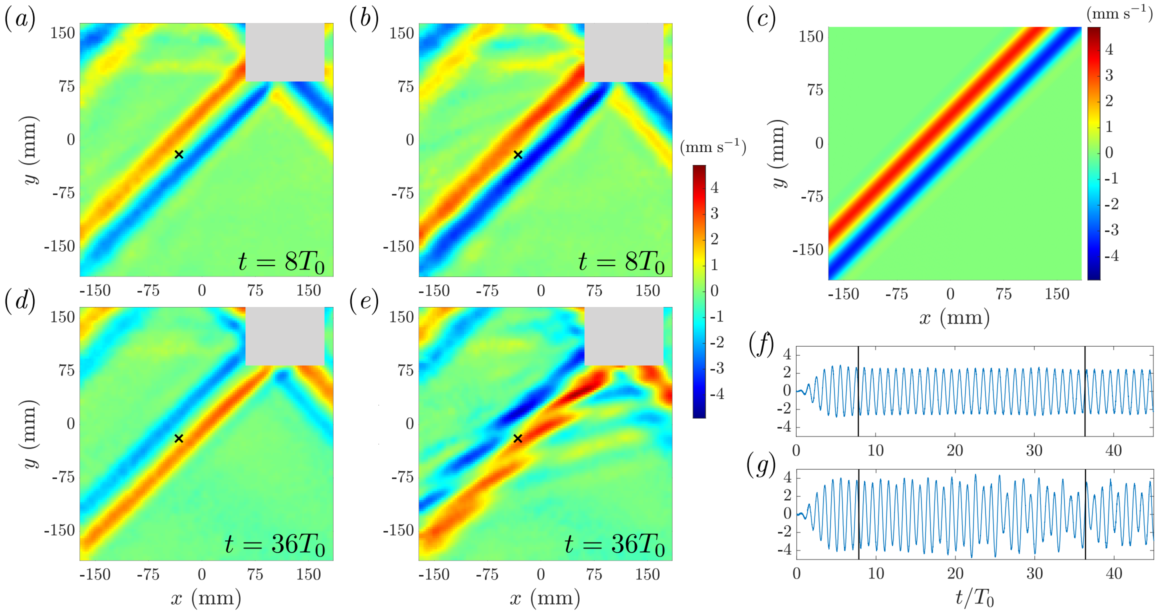

Figure 2-2: (*a*) Horizontal (x-) velocity for beam inclination angle $\theta = 45^\circ$ and forcing amplitude $A/L = 0.45$ at $t = 8T_0$ after start of forcing. The grey box corresponds to the region around the cylinder that is masked out. (*b*) Same as (*a*) but for $A/L = 0.63$. (*c*) Theoretical beam profile used in the linear stability analysis of §2.5 to approximate the experimental beam in (*b*). (*d*) Same as (*a*) but at $t = 36T_0$ after start of forcing. (*e*) Same as (*d*) but for $A/L = 0.63$. (*f*) Time series of the horizontal velocity for $A/L = 0.45$ at the location marked with the cross in (*a*,*d*). The vertical lines indicate the times $t = 8T_0$ and $36T_0$. (*g*) Same as (*f*) but for $A/L = 0.63$ and at the location marked with the cross in (*b*,*e*).

nant peak at the primary wave frequency ω_0/N, as well as smaller peaks corresponding to the second and third harmonic. As $2\omega_0 > N$ for all experiments reported in this study, these higher harmonics exist only within the primary beam and do not propagate. Given that a uniform inviscid beam involves a single harmonic (Tabaei & Akylas, 2003, see also equation (2.4) below), the observed higher harmonics arise from nonlinear self-interactions of the primary wave brought about by along-beam variations in the beam profile due to the effects of viscosity. In contrast to the lower-amplitude, stable beam (at $A/L = 0.45$), however, the frequency spectrum of the higher-amplitude, unstable beam (at $A/L = 0.63$) features several additional peaks, corresponding to multiple daughter waves spontaneously generated via instability. According to figure 2-3(a), the strongest of these peaks occur at the subharmonic frequencies $\omega_1/N = 0.26$ and $\omega_2/N = 0.45$. The corresponding spatial disturbances, obtained by filtering the experimental wave field about the selected frequency with a window of ± 0.05 rad s^{-1}, are plotted in figure 2-3(b,c). Both subharmonic waves have wavepacket-like spatial structure with smaller carrier wavelength than the width of the primary beam (carrier wavelengths measured to be approximately 44 mm for $\omega_1/N = 0.26$ in figure 2-3b and 29 mm for $\omega_2/N = 0.45$ in figure 2-3c), and they propagate in opposite directions with respect to the primary beam. Furthermore, upon estimating the inclination angle to the horizontal of their wave crests ($\theta_1 \approx 15^\circ$ for $\omega_1/N = 0.26$ and $\theta_2 \approx 27^\circ$ for $\omega_2/N = 0.45$), it is concluded that the subharmonic waves approximately satisfy the internal wave dispersion relation, $\omega^2 = N^2 \sin^2\theta$.

It is worth noting that the observed subharmonic instability disturbances along with the primary beam appear to satisfy, to a rough approximation, the conditions for TRI. Specifically, according to the classical theory of TRI (e.g. Bourget *et al.*, 2013), a sinusoidal primary wave of infinitesimal amplitude with frequency ω_0 and wavevector $\boldsymbol{k}_0$ can be unstable to subharmonic perturbations, also in the form of sinusoidal waves, with frequencies (ω_1, ω_2) and wavevectors $(\boldsymbol{k}_1, \boldsymbol{k}_2)$, if the three waves form a resonant triad:

$$\omega_1 + \omega_2 = \omega_0, \tag{2.2a}$$

$$\boldsymbol{k}_1 + \boldsymbol{k}_2 = \boldsymbol{k}_0. \tag{2.2b}$$

Here, the observed subharmonic frequencies $\omega_1/N = 0.26$ and $\omega_2/N = 0.45$ of the instability, along with the primary wave frequency $\omega_0/N = 0.71$, clearly satisfy to a good approximation the frequency resonance condition (2.2a). In regard to the spatial resonance condition (2.2b), the carrier wavevectors of the observed subharmonic disturbances, calculated using the carrier wavelength and inclination angle estimated above, are given in the coordinate system (ξ, η) by $\boldsymbol{k}_1 = (71, -124)$ m^{-1} for $\omega_1/N = 0.26$ and $\boldsymbol{k}_2 = (-67, 206)$ m^{-1} for $\omega_2/N = 0.45$. Then, taking the primary beam width of roughly 80 mm to correspond to a single wavelength, we find that $\boldsymbol{k}_0 = (0, 79)$ m^{-1}, which is approximately equal to $\boldsymbol{k}_1 + \boldsymbol{k}_2 = (4, 82)$ m^{-1}.

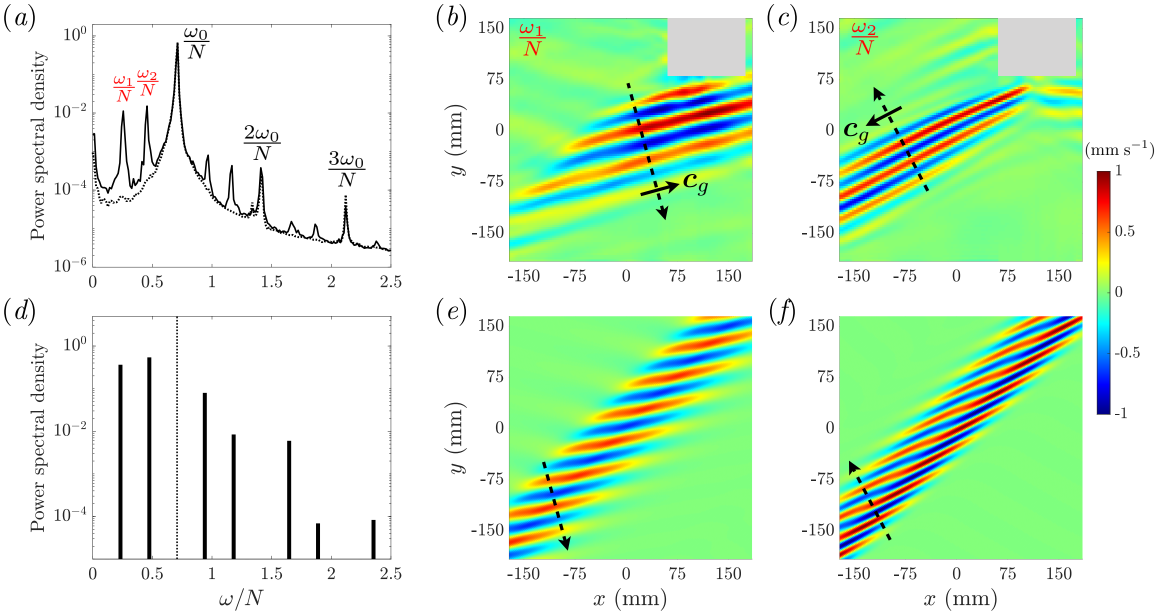

Figure 2-3: (a) Spatially-averaged time frequency spectra for the experiments shown in figure 2-2. The dotted line corresponds to the stable case at $A/L = 0.45$ (figure 2-2a,d) while the solid line corresponds to the unstable case at $A/L = 0.63$ (figure 2-2b,e). The subharmonic frequencies $\omega_1/N = 0.26$ and $\omega_2/N = 0.45$ are labelled. (b) Experimentally measured horizontal velocity field from figure 2-2(e), filtered at $\omega_1/N = 0.26$. (c) Same as (b) but filtered at $\omega_2/N = 0.45$. (d) Time frequency spectrum of the fastest-growing Floquet mode. The vertical dotted line marks the primary wave frequency at ω_0/N. (e) Theoretically predicted spatial mode shape corresponding to the first peak (from the left) in the frequency spectrum in (d) at $\omega/N = 0.24$. (f) Same as (e) but for the second peak at $\omega/N = 0.47$. Dashed arrows in (b,c,e,f) indicate direction of phase propagation. Solid arrows in (b,c) indicate direction of group velocity $\boldsymbol{c}_g$. Velocity scale in (e,f) is normalized to have the same maximum velocity as in (b,c).

However, in spite of this apparent resonant triad, the theory for TRI, strictly, is not applicable in the present setting: the primary wave is not sinusoidal but rather a thin beam with a broadband spectrum of wavenumbers and no defined carrier wavevector $\boldsymbol{k}_0$, so the meaning of (2.2b) is not clear. As noted in §2.1, the finite width of the beam dramatically affects the instability dynamics and adds new physics, namely the group velocity of the perturbations, which is ignored in the classical TRI theory (Karimi & Akylas, 2014). Furthermore, the stability predictions of TRI theory cannot be trusted: treating our thin beam as one wavelength of a primary sinusoidal wave with $\omega_0/N = 0.71$ and $\boldsymbol{k}_0 = (0, 79)$ m^{-1}, the most unstable triad according to TRI theory involves a subharmonic perturbation with wavelength greater than the primary beam width, contradicting our findings (figure 2-3b,c). Thus, to make quantitative comparisons with experimental observations, we turn to a formal stability analysis based on Floquet theory that takes into account both the finite width and finite amplitude of the primary wave beam.

2.4 Stability analysis

The analysis assumes an unbounded, incompressible, uniformly stratified Boussinesq fluid with constant buoyancy frequency N. While in the rest of the paper we use dimensional variables, here we find it more convenient to work with nondimensional variables for ease of notation. Using $1/N$ as the time scale and the cylinder radius L (see §2.2) as the length scale, the dimensionless governing equations for the velocity field $\boldsymbol{u}$, the reduced density ρ and pressure p are

$$\boldsymbol{\nabla} \cdot \boldsymbol{u} = 0, \tag{2.3a}$$

$$\rho_t + \boldsymbol{u} \cdot \boldsymbol{\nabla} \rho = \boldsymbol{u} \cdot \boldsymbol{j}, \tag{2.3b}$$

$$\boldsymbol{u}_t + \boldsymbol{u} \cdot \boldsymbol{\nabla} \boldsymbol{u} = -\boldsymbol{\nabla} p - \rho \boldsymbol{j} + \nu \nabla^2 \boldsymbol{u}. \tag{2.3c}$$

Here, $\boldsymbol{j}$ is a vertical unit vector pointing upwards and $\nu = \nu_*/NL^2$ is the inverse Reynolds number, where ν_* denotes the kinematic viscosity.

In the inviscid limit ($\nu = 0$), (2.3) supports time-harmonic plane waves in the form of uniform beams (Tabaei & Akylas, 2003)

$$u = u_0(\eta, t) = U(\eta)\mathrm{e}^{-\mathrm{i}\omega_0 t} + \text{c.c.}, \quad v = v_0 = 0, \quad w = w_0 = 0, \tag{2.4a}$$

$$\rho = \rho_0(\eta, t) = -\mathrm{i}U(\eta)\mathrm{e}^{-\mathrm{i}\omega_0 t} + \text{c.c.}, \tag{2.4b}$$

$$p = p_0(\eta, t) = \mathrm{i}\cos\theta \int^{\eta} U(\eta')\,\mathrm{d}\eta'\,\mathrm{e}^{-\mathrm{i}\omega_0 t} + \text{c.c.}, \tag{2.4c}$$

where $U(\eta)$ describes the beam profile and is related to the wave generation mechanism. Here, $\boldsymbol{u} = (u, v, w)$ are the velocity components in the beam-aligned coordinate system (ξ, η, ζ) defined by the along-beam, cross-beam and transverse horizontal coordinate, respectively (see figure 2-1*d*). These coordinates are related to (x, y, z) by $\xi = -x\cos\theta - y\sin\theta$, $\eta = -x\sin\theta + y\cos\theta$, and $z = -\zeta$, where θ is the beam inclination angle to the horizontal, specified by the forcing frequency ω_0 via the (nondimensional) dispersion relation $\omega_0 = \sin\theta$.

The uniform beam given by (2.4) will be used as the basic state for the ensuing stability analysis. The choice of $U(\eta)$ for comparison with experimental observations will be specified later in §2.5.1. As already noted, viscous effects ($\nu \neq 0$) introduce along-beam (ξ-) variations in (2.4), corresponding to broadening and a decrease in amplitude of the beam profile far from the forcing (Mowbray & Rarity, 1967; Thomas & Stevenson, 1972). However, in the interest of simplifying the stability analysis, these effects will be ignored.

To examine the linear stability of the uniform beam (2.4), we now superimpose infinitesimal perturbations in the form of normal modes,

$$u = u_0(\eta, t) + \Big\{\hat{u}(\eta, t)\mathrm{e}^{\mathrm{i}(\mu\xi + m\zeta)} + \text{c.c.}\Big\}, \tag{2.5}$$

with similar expressions for v, w, ρ and p. Here, μ and m are real parameters that specify the along-beam and transverse wavenumbers of the perturbation. Inserting (2.5) into (2.3), linearizing with respect to the perturbations and dropping the hats, we obtain the following equations governing the perturbations

$$0 = \mathrm{i}\mu u + \frac{\partial v}{\partial \eta} + \mathrm{i}mw, \tag{2.6a}$$

$$\frac{\partial \rho}{\partial t} = -\mathrm{i}\mu u_0 \rho - \frac{\mathrm{d}\rho_0}{\mathrm{d}\eta} v - u\sin\theta + v\cos\theta, \tag{2.6b}$$

$$\frac{\partial u}{\partial t} = -\mathrm{i}\mu u_0 u - \frac{\mathrm{d}u_0}{\mathrm{d}\eta} v - \mathrm{i}\mu p + \rho\sin\theta + \nu\left(-\mu^2 + \frac{\partial^2}{\partial \eta^2} - m^2\right)u, \tag{2.6c}$$

$$\frac{\partial v}{\partial t} = -\mathrm{i}\mu u_0 v - \frac{\partial p}{\partial \eta} - \rho\cos\theta + \nu\left(-\mu^2 + \frac{\partial^2}{\partial \eta^2} - m^2\right)v, \tag{2.6d}$$

$$\frac{\partial w}{\partial t} = -\mathrm{i}\mu u_0 w - \mathrm{i}mp + \nu\left(-\mu^2 + \frac{\partial^2}{\partial \eta^2} - m^2\right)w. \tag{2.6e}$$

It can be verified by eliminating p that it is sufficient to consider $\mu \geq 0$ and $m \geq 0$ owing to symmetry (see §A.1). It should be noted that (2.6) includes the full effects of viscosity on the perturbations.

To solve the stability equations (2.6), as the basic state $u_0(\eta, t)$ in (2.4) is periodic in t, it is necessary to apply Floquet theory. In the widely-studied case of a sinusoidal plane wave, i.e. $U(\eta) = U_0 \mathrm{e}^{\mathrm{i}k_0\eta}/2$ in (2.4), this task is carried out (e.g. Mied, 1976; Klostermeyer, 1991) by expressing $(\boldsymbol{u}, \rho, p)$ as infinite Fourier series in $k_0\eta - \omega_0 t$, multiplied with an exponential term that contains the Floquet exponent. After truncating the Fourier series, the resulting eigenvalue problem is solved numerically to obtain the Floquet exponents which give the instability growth rates. This procedure is then performed over a variety of parameters μ and m in order to determine the perturbations with the highest growth rate. In the present setting, however, the primary wave profile U is a general, locally-confined function of η. Thus, in addition to a Fourier expansion in t, separate discretization in η is also necessary, resulting in an eigenvalue problem that is too large to be solved efficiently.

Instead, we follow the approach recently taken by Onuki & Tanaka (2019) to study the stability of finite-amplitude internal wave beams under oceanic flow conditions and by Jouve & Ogilvie (2014) for the stability of inertial wave beams, as well as by earlier authors for Floquet problems in other contexts (e.g. Schatz *et al.*, 1995). Briefly, this approach relies on the monodromy matrix, which can be easily computed using time-integration. First, we eliminate v and p from (2.6) and discretize in η to obtain the matrix equation

$$\frac{\mathrm{d}\chi}{\mathrm{d}t} = A(t)\chi, \tag{2.7}$$

where $\chi = \{u, w, \rho\}$ is the state vector and $A(t) = A(t + T_0)$ is the periodic matrix (with period $T_0 = 2\pi/\omega_0$) that results from the right-hand side of (2.6). Based on Floquet theory, a fundamental solution matrix to (2.7) is given by $X(t) = \mathrm{e}^{Bt}P(t)$, where $X = \{\chi_1, \chi_2, ...\}$ is composed of linearly independent solutions to (2.7), B is a constant matrix whose eigenvalues are the Floquet exponents λ_i, and $P(t) = P(t + T_0) = \{P_1, P_2, ...\}$ is a periodic matrix composed of the Floquet modes. Because P is T_0-periodic, it follows that $X(T_0) = MX(0)$, where $M \equiv \mathrm{e}^{BT_0}$ is called the monodromy matrix and represents the effect of the operator A over one period (i.e. the linearized Poincaré map). To find M, we set $X(0) = I$, the identity matrix, as the initial condition, integrate (2.7) over one period to obtain $X(T_0)$, and compute $M = X(T_0)$. Next, we compute the eigenvalues of M, denoted α_i, to obtain the Floquet exponents $\lambda_i = (\log \alpha_i)/T_0$. By definition of the Floquet exponent, $\chi \propto \exp(\lambda_i t)$ so $\mathrm{Re}(\lambda_i) > 0$ implies instability. Finally, we repeat this procedure for various μ and m in order to find the instability modes with the highest growth rate. We implemented this procedure by discretizing (2.6) using a pseudo-spectral method with 512 Fourier modes in $\eta \in [-30, 30]$ and integrating (2.7) with fourth-order Runge–Kutta time stepping and a typical $\Delta t = 0.02$. The ensuing eigenvalue problem was then solved using standard MATLAB algorithms.

2.5 Comparison of observations with Floquet analysis

2.5.1 Instability dynamics

We now make comparisons between the observed instability in §2.3 and the predictions of the linear stability analysis outlined in §2.4. Taking into account the experimental parameters, the inverse Reynolds number $\nu = 0.0021$. In addition, we chose the primary beam profile $U(\eta)$ in (2.4) to be

$$U(\eta) = \frac{1}{2} U_0 \frac{\int_0^\infty J_1(K) \exp\bigl(-dK^3 + \mathrm{i}K\eta\bigr)\,\mathrm{d}K}{\max\bigl|\int_0^\infty J_1(K) \exp(-dK^3 + \mathrm{i}K\eta)\,\mathrm{d}K\bigr|}, \tag{2.8}$$

where J_1 denotes the Bessel function of order 1. Here, U_0 is an amplitude parameter that corresponds to the maximum nondimensional along-beam velocity (i.e. $\max|u_0| = U_0$) and d controls the shape of the profile. Expression (2.8) is based on the linear viscous solution by Hurley & Keady (1997) for a beam generated by an oscillating cylinder. However, rather than using their solution as originally formulated, which would give U_0 as a function of d, we instead independently fit U_0 and d using the experimentally measured beam profile at a cross-beam slice located 20 cm away from the cylinder. This allowed us to accurately approximate the experimental beam profile and to study the effect of beam amplitude independently of the profile shape (see §2.5.2). It should be noted that the agreement between the original solution of Hurley & Keady (1997) and the experimental observations is overall satisfactory, although it varies depending on the beam inclination angle and forcing amplitude, and our choice to decouple U_0 from d is primarily for convenience. Here, for $U_0 = 0.25$ and $d = 0.0137$ in (2.8), the basic state (2.4) agrees nicely with the experimentally generated unstable beam (at $A/L = 0.63$) discussed in §2.3 for all times after the initial transient (due to start-up of the forcing) and prior to the onset of instability. For comparison, figure

2-2(*c*) plots a snapshot of the theoretical beam (2.4) using the profile (2.8) at the same time as the experimentally observed beam in figure 2-2(*b*). These values of U_0 and d were used for the stability results presented in §2.5.2 below, as well as in §2.6.1. Furthermore, here we only consider two-dimensional ($m = 0$) instability modes. A discussion of the effects of transverse variations ($m \neq 0$) is presented in §2.6.1.

Figure 2-3(*d*) plots the frequency spectrum of the computed two-dimensional Floquet mode with the highest growth rate. The theoretical spectrum shows good quantitative agreement with the experimentally measured frequency spectrum (figure 2-3*a*) across all instability peaks. For instance, the strongest four frequencies, in order of power, that comprise the experimentally measured instability are $\omega/N = \{0.45, 0.26, 0.97, 1.17\}$, while the strongest four instability frequencies predicted theoretically are $\omega/N = \{0.47, 0.24, 0.94, 1.18\}$. Furthermore, the spatial disturbances associated with the strongest two predicted frequency components at $\omega/N = 0.24$ and $\omega/N = 0.47$ (figure 2-3*e*,*f*) are in excellent agreement in both length scale and direction of propagation with the experimental measurements filtered at $\omega_1/N = 0.26$ and $\omega_2/N = 0.45$ (figure 2-3*b*,*c*). The filtered experimental observations were obtained using the Hilbert transform technique (Mercier *et al.*, 2008). The velocity scale for the theoretically predicted spatial disturbances is normalized to have the same maximum velocity as the experimental measurements.

It is important to note that our theoretical predictions correspond to linear stability modes, which decay outside the primary wave beam and are valid only for limited times after the onset of instability, while the experimental observations correspond to perturbations that evolve according to fully nonlinear dynamics and may eventually propagate freely. This is evident in figure 2-3(*b*,*c*) as the perturbations extend outside the primary wave beam in the direction of their group velocity. In addition, our theory assumes an infinitely long, uniform primary beam, while the experimentally generated beam is of finite length and features slight along-beam variations in amplitude and profile shape as a result of viscosity. Accordingly, the theoretically predicted perturbations extend the entire length of the beam, whereas the experimentally observed perturbations are locally confined in the along-beam direction. Finally, although the Floquet analysis makes quantitative predictions of the instability growth rate, it is not possible to make accurate comparisons with our experimental observations. Figure 2-2(*g*) indicates that the initial (exponential) growth of the perturbations likely lasts no more than 10 periods of oscillation of the primary wave. As a result, estimation of the observed growth rate using a short-time Fourier transform yields poor temporal resolution and significant errors, especially since the observed subharmonic perturbations with frequencies $\omega_1/N = 0.26$ and $\omega_2/N = 0.45$ have even longer period than the primary wave. Instead, a qualitative discussion of growth rates is made later in connection with the threshold amplitude for instability (see §2.5.2).

Our theoretical results confirm that the Floquet stability analysis captures the observed instability of a finite-amplitude thin beam: there is excellent agreement between theory and experiment across the multi-frequency spectrum associated with the instability. Even though the classical TRI theory is not applicable for our system as argued in §2.3, the observed instability still displays similarities to TRI. Specifically, both our experimental observations and stability analysis show that the dominant components of the instability are two subharmonic disturbances in the form of modulated wavepackets. These disturbances, moreover, satisfy the frequency resonance condition (2.2a) and also very roughly satisfy the spatial resonance condition (2.2b). The observed instability thus may be regarded as a finite-amplitude form of TRI, whose dynamics still features subharmonic disturbances that satisfy triad resonance to some extent, but the finite width and amplitude of the underlying beam are major controlling factors as well.

2.5.2 Effects of beam amplitude and angle

We now assess the effects of beam amplitude and propagation angle θ (i.e. forcing frequency) on the instability dynamics. Figure 2-4 shows a phase diagram of all stable and unstable experimental configurations observed across a range of amplitudes and angles. Here, just as in §2.5.1, U_0 is the maximum nondimensional along-beam velocity ($\max|u_0| = U_0$) of the observed beam at a slice located 20 cm away from the cylinder and prior to onset of instability, if present. The stable and unstable beams shown in figure 2-2 and discussed in §§2.3 and 2.5.1 correspond to the points located at $\theta = 45°$ and $U_0 = 0.18$ and 0.25, respectively.

Figure 2-4 indicates that for given beam angle there exists a critical amplitude below which the beam is stable. This is in qualitative agreement with the analysis of Karimi & Akylas (2014), according to which weakly nonlinear (i.e. $U_0 \ll 1$) thin beams are stable to PSI, although formally, their asymptotic assumption of fine-scale perturbations (relative to the primary beam) does not hold here. Figure 2-4 also shows that beams with shallower angles of propagation (i.e. smaller θ) require higher amplitudes to undergo instability. It should be noted that all experimental wave beams were below the overturning amplitude for density inversions given by $\mathrm{d}\rho_0/\mathrm{d}y = 1$ (e.g. see Kataoka & Akylas, 2013), which occurs at $U_0 \cos\theta \approx 0.47$ for the uniform beam (2.4) with the profile (2.8).

Furthermore, figure 2-4 overlays the nondimensional growth rate $\sigma \equiv \max_{i,\mu} \mathrm{Re}(\lambda_i)$, where λ_i are the (nondimensional) Floquet exponents predicted by the Floquet stability analysis, as a function of θ and U_0 for the same primary beam profile (2.8) as in §2.5.1. Here, for simplicity, we take the parameter d, which controls the shape of the beam profile, to be fixed $d = 0.0137$ as θ and U_0 are varied. In reality, the observed beam profiles show slight dependence on θ, with the experimentally fitted d ranging between 0.012 and 0.017 at a location 20 cm away from the cylinder; however, these differences do not significantly affect the predicted growth rate and are ignored.

Although the contours of constant growth rate in figure 2-4 appear to qualitatively follow the observed transition region between stability and instability, we find that the linear

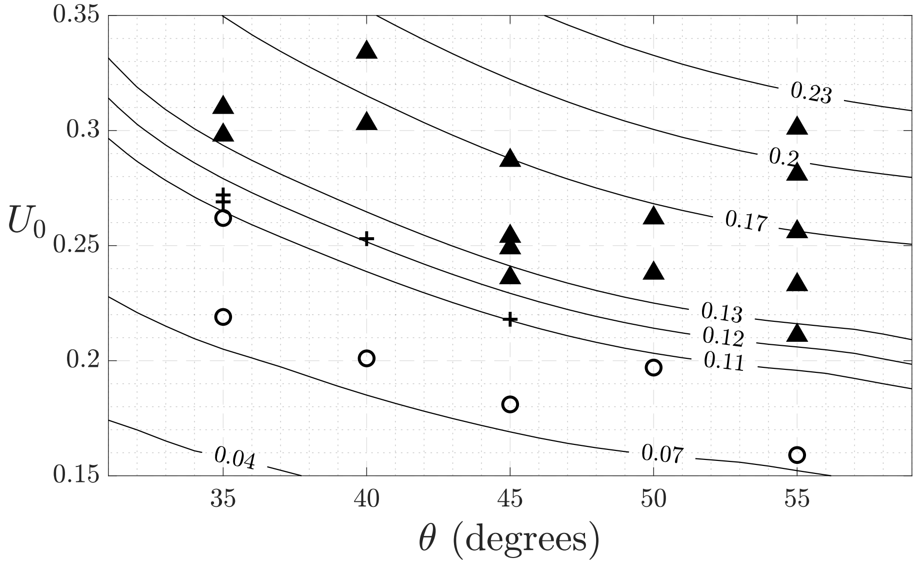

Figure 2-4: Phase diagram showing the dependence of the instability on the nondimensional beam amplitude U_0 and beam angle θ. (▲): experimental configurations where instability was visibly apparent; (+): experimental configurations where instability was not visibly apparent but small instability peaks could be seen in the time frequency spectrum; (○): stable configurations. Overlaid are contour lines of the (nondimensional) real growth rate $\sigma \equiv \max_{i,\mu} \mathrm{Re}(\lambda_i)$ as predicted by Floquet stability analysis.

stability analysis predicts instability for all experimental configurations, including those observed to be stable. According to the Floquet analysis, there is a critical amplitude for instability in qualitative agreement with observation, but the theoretical amplitude threshold is smaller than what is observed. For example, at $\theta = 45°$, the Floquet analysis predicts the critical amplitude for instability to be $U_0 \approx 0.09$, whereas the experimental observations suggest that it is between 0.18 and 0.23. This discrepancy may be attributed to various factors not accounted for in the stability analysis, including the presence of along-beam variations in the beam profile, three-dimensional (transverse) effects, and induced mean flows such as streaming. An analysis of the effects of along-beam profile variations lies outside the scope of this study. The effects of three-dimensional variations and mean flows on the instability dynamics are discussed below.

2.6 Three-dimensional effects

2.6.1 Perturbations with transverse variations

The stability results reported in §2.5 assume that the primary wave beam as well as the perturbations are purely two-dimensional, i.e. there are no variations in the transverse horizontal (ζ-) direction. While these assumptions are reasonable given the small radius-to-length ratio (≈ 0.044) of the uniform cylinder used in the experiments described thus

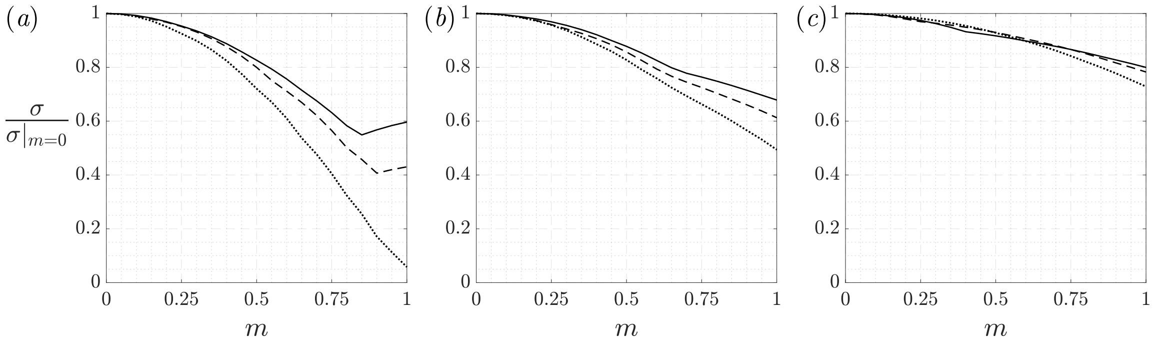

Figure 2-5: Dependence of the instability growth rate σ on the dimensionless transverse wavenumber m as predicted by the Floquet analysis for beam angle (*a*) $\theta = 35°$, (*b*) $\theta = 45°$, (*c*) $\theta = 55°$; and dimensionless beam amplitude $U_0 = 0.15$ (dotted line), $U_0 = 0.20$ (dashed line), and $U_0 = 0.25$ (solid line). All growth rates are normalized by the two-dimensional ($m = 0$) growth rate.

far, some three-dimensional effects are inevitably introduced by the finite transverse extent of the tank. First, we consider the effect of $m \neq 0$ in (2.5), corresponding to infinitesimal perturbations that vary sinusoidally in ζ on a purely two-dimensional primary beam. Using the same beam profile (2.8) with $d = 0.0137$, figure 2-5 plots the theoretically predicted growth rate as a function of the dimensionless transverse wavenumber m for various values of beam angle θ and dimensionless beam amplitude U_0. These results indicate that perturbations with transverse variations have lower instability growth rate, and this effect is more pronounced for shallower beam angles and lower beam amplitudes. As a crude estimate, by taking the tank width to be half a wavelength of transverse variation, we find that $m \approx 0.26$, which would decrease by $\lesssim 10\%$ the growth rates for $35° \leq \theta \leq 55°$ and $0.15 \leq U_0 \leq 0.25$.

2.6.2 Transverse beam variations and induced mean flows

As pointed out by recent work, transverse variations in the primary wave beam enable production of mean potential vorticity, which results in a horizontal mean flow (Bordes *et al.*, 2012; Kataoka & Akylas, 2015; Fan *et al.*, 2018; Jamin *et al.*, 2020). This induced mean flow has two components, one of inviscid and the other of viscous origin. The latter, known as streaming, grows resonantly in time and is expected to dominate in a laboratory setting where viscous effects are more pronounced (Fan *et al.*, 2018). It should be noted that along-beam modulations of a purely two-dimensional inviscid beam can also generate a mean flow, but unlike streaming this mean flow is in the along-beam direction and does not grow resonantly (Tabaei & Akylas, 2003).

Throughout our experiments using the uniform cylinder, we indeed observed a slowly evolving horizontal mean flow within the primary wave beam (e.g. see time-frequency spectra in figure 2-3*a*). Figure 2-6 plots two examples of this mean flow, obtained by filtering the horizontal velocity about the zero-frequency. As no vertical mean flows were observed, this

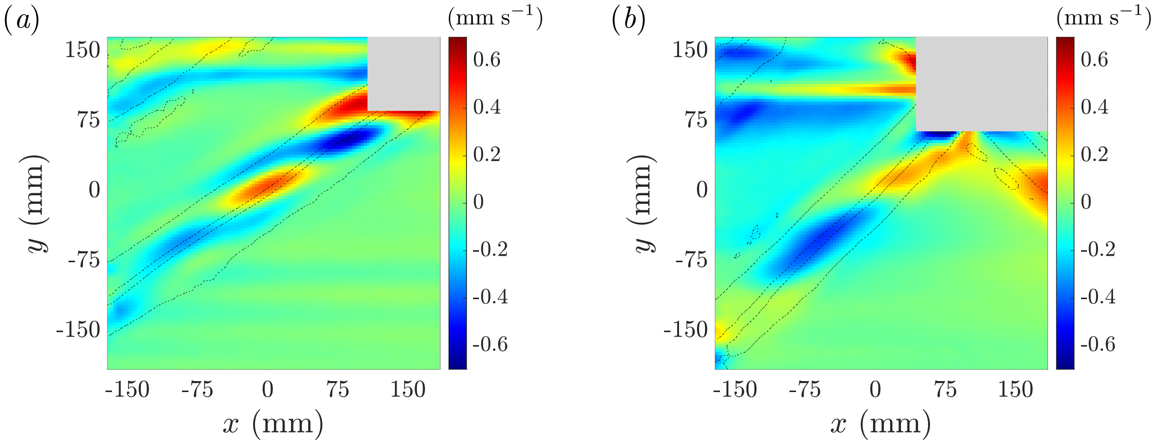

Figure 2-6: Experimental mean horizontal velocity field at $t = 300$ s, obtained by filtering the horizontal velocity field around the zero-frequency. The uniform cylinder is used as forcing. (*a*) beam inclination angle $\theta = 35°$ and forcing amplitude $A/L = 0.72$, with $t = 300$ s $\approx 26T_0$; (*b*) $\theta = 45°$ and $A/L = 0.54$, with $t = 300$ s $\approx 32T_0$. In both cases, the primary wave beam has nondimensional maximum along-beam velocity $U_0 \approx 0.22$ measured 20 cm away from the cylinder, and did not exhibit any visible signs of instability. Contours of the horizontal velocity field of the primary wave beam at ± 1 mm s^{-1} are plotted in the dotted lines.

horizontal mean flow suggests that three-dimensional effects due to the finite width of the tank are indeed present and may play a role in the instability dynamics. It is worth noting that a mean flow is also generated by near-cylinder boundary-layer effects, but it is confined to the vertical (y-) location of the cylinder (seen as the long horizontal bands at the top of figure 2-6) and remains distinct from the mean flow generated within the beam itself.

In order to more concretely assess the effect of three-dimensional variations on the instability dynamics, experiments were also conducted using a non-uniform cylinder whose middle section had the same radius as the straight cylinder, but whose end sections had smaller radius (see §2.2 and figure 2-1*c*). Figure 2-7 plots the experimentally observed wave fields using the uniform and non-uniform cylinders at $\theta = 45°$ and forcing amplitude $A/L = 0.63$. For the uniform cylinder, these forcing conditions are precisely the ones used to generate the unstable beam discussed in §2.3 and shown in figure 2-2. Here, however, PIV measurements were made at two different transverse locations: (i) $z = 4.3$ cm, where both the uniform and non-uniform cylinders have radius 22.2 mm; and (ii) $z = 14.3$ cm, where the non-uniform cylinder has radius 15.2 mm. The beam generated using the uniform cylinder undergoes instability (figure 2-7*a*,*b*), just as discussed in §2.3. Even so, transverse variations, introduced by the finite width of the tank, are visible as the instability appears to be slightly weaker at $z = 14.3$ cm (figure 2-7*b*), which is closer to the lateral tank walls, than at $z = 4.3$ cm (figure 2-7*a*). The beam generated using the non-uniform cylinder (figure 2-7*d*,*e*) is noticeably thinner at $z = 14.3$ cm than at $z = 4.3$ cm, as a result of the smaller cylinder radius at $z = 14.3$ cm. Most importantly, however, in contrast to the beam due to the uniform cylinder, the beam due to the non-uniform cylinder appears to be essentially stable, and remained so even at longer times ($t = 63T_0$). This suggests that transverse variations significantly weaken the TRI-like instability discussed in §2.3.

Furthermore, figure 2-7(*c*,*f*) compares the strength of the induced horizontal mean flow due to the uniform cylinder against that due to the non-uniform cylinder, at $t = 39T_0$ after start of forcing. As expected, the mean flow generated by the non-uniform cylinder was much stronger than its counterpart due to the uniform cylinder. For the non-uniform cylinder, this mean flow was observed to grow approximately linearly (resonantly) in early times and is therefore likely of the streaming type. Furthermore, in this instance, the strong mean flow noticeably bends the beam (figure 2-7*e*), as was found for streaming (Fan *et al.*, 2018).

Our observations thus indicate that enhancing transverse variations weakens the TRI-like instability and instead favours streaming, an effect that is likely also dependent on forcing amplitude and beam angle, as suggested by the results of §2.5.2. This provides a plausible explanation for why Bordes *et al.* (2012) observed strong streaming but not TRI: the presence of significant transverse beam variations due to their wavemaker, which spanned only about 1/6 of the tank width, as well as the shallow beam angles ($15° \leq \theta \leq 30°$) used in their study, apparently acted to completely mask TRI.

2.7 Concluding remarks

Most prior stability studies of internal gravity wave beams focused on subharmonic instabilities due to resonant triad interactions. This instability mechanism is pertinent to small-amplitude nearly monochromatic beams – either as PSI in the nearly inviscid limit appropriate to oceans (Karimi & Akylas, 2014, 2017; Fan & Akylas, 2020*b*) or as TRI under laboratory flow conditions (Bourget *et al.*, 2013). By contrast, the present investigation considered finite-amplitude wave beams whose profile comprises roughly one wavelength, akin to those originally observed by Mowbray & Rarity (1967). Such thin beams, generated in a stratified fluid tank by oscillating a cylinder in the direction of beam propagation, were observed to be unstable above a threshold wave amplitude to two subharmonic perturbations with wavepacket-like spatial structure. Despite certain similarities to the familiar TRI of small-amplitude nearly monochromatic wave beams, this novel instability can be treated theoretically only via formal stability analysis of a finite-amplitude beam based on Floquet theory. Adapting to our experimental flow conditions the computational procedure used by Onuki & Tanaka (2019) for finite-amplitude oceanic internal wave beams, the computed most unstable Floquet modes are in very good agreement with the observed subharmonic disturbances.

Our observed instability bears resemblance to recent observations of instability in internal wave attractors (Scolan *et al.*, 2013; Brouzet *et al.*, 2016), which also involve thin beams

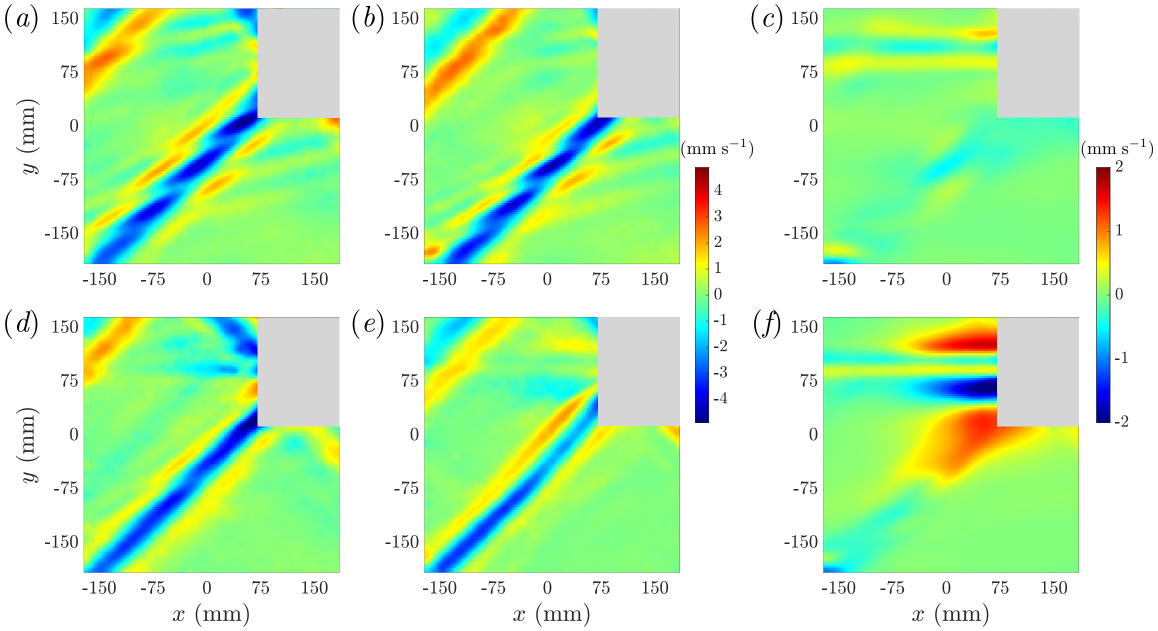

Figure 2-7: Experimental velocity fields for beam inclination angle $\theta = 45°$ and forcing amplitude $A/L = 0.63$ using the uniform cylinder (a–c) and the non-uniform cylinder (d–e) at $t = 39T_0$, where T_0 is the forcing period. Plots (a,d) show the horizontal velocity field at $z = 4.3$ cm while (b,e) show the horizontal velocity field at $z = 14.3$ cm, closer to the lateral tank wall. Plots (c,f) show the mean horizontal velocity field at $z = 14.3$ cm obtained by filtering (b,e), respectively, around the zero-frequency. No significant vertical mean flows were observed.

that feature no more than a single wavelength. In these studies, the authors report that the observed instability appears to satisfy the triad resonance conditions. However, as discussed at the end of §2.3, the TRI theory is not strictly applicable for these thin beams, and it is unclear whether the most unstable triad predicted by TRI theory matches their observed instability. In view of the results presented here, it is possible that Floquet stability analysis, which takes into full account the finite width and amplitude of the beam, may be used to predict the observed instability frequencies and wavevectors of the attractor system. This approach has been used by Jouve & Ogilvie (2014) to predict theoretically the instability found in numerical simulations of an inertial wave attractor.

We also explored the significance of three-dimensional effects on the observed subharmonic instability. According to our Floquet stability analysis, under the experimental flow conditions, infinitesimal perturbations with sinusoidal dependence in the transverse direction generally have smaller growth rates than their two-dimensional counterparts. Furthermore, finite transverse beam variations, introduced by using as forcing a cylinder with non-uniform radius, were observed to weaken the subharmonic instability and, in addition, to induce a horizontal mean flow of the streaming type. Thus, although it is possible for TRI-like subharmonic instability and streaming to co-exist, in the presence of significant transverse variations the latter effect is expected to dominate, consistent with the observations of Bordes *et al.* (2012). However, in more complex three-dimensional geometries, such as in the axisymmetric thin beams generated by an oscillating torus (Shmakova & Flór, 2019), instability of the TRI-type may still be important, particularly in the intersection region of various wave beams.

In the nearly-inviscid oceanic context, the strength of streaming probably would be greatly diminished as it hinges on the generation of mean potential vorticity by dissipative processes. On the other hand, as also hinted by the nearly inviscid stability computations of Onuki & Tanaka (2019) and Fan & Akylas (2020*b*), the finite-amplitude TRI-like instability of thin beams discussed here is likely to persist. However, as we find that the beam propagation angle θ plays an important part in the instability dynamics, a complete stability analysis for θ in the range $3^\circ \lesssim \theta \lesssim 5^\circ$, appropriate to oceanic beams, is necessary and is left to future studies.

Chapter 3

Instabilities of finite-width internal wave beams: from Floquet analysis to PSI

This work has been submitted to *Journal of Fluid Mechanics.*

3.1 Introduction

The stability of internal gravity waves in a continuously stratified fluid is a problem of fundamental and geophysical interest. Early work focused on sinusoidal plane waves in an inviscid Boussinesq fluid with constant buoyancy frequency. In this idealized setting, linear stability analysis based on Floquet theory has revealed a wide host of instabilities with varying dynamics and physical mechanisms (e.g. see Sonmor & Klaassen, 1997, for a comprehensive treatment). As first noted by Mied (1976), in the limit of small primary wave amplitude, this diverse range of instabilities reduce to triad resonant interactions: the primary wave is unstable to two sinusoidal subharmonic perturbations whose frequencies and wavevectors sum to those of the basic state. A specific form of such triadic resonant instability (TRI), where the subharmonic perturbations have half the frequency of the primary wave and very fine wavelength, is the celebrated parametric subharmonic instability (PSI). This mechanism has attracted considerable interest as it permits transfer of energy into much smaller scales (e.g. Staquet & Sommeria, 2002) and therefore may be a potentially significant factor in the dissipation of oceanic internal waves (Hibiya *et al.*, 2002; MacKinnon & Winters, 2005; Young *et al.*, 2008).

In more recent work, attention shifted from sinusoidal waves to time-harmonic plane waves with locally confined spatial profile: such wave beams arise in oceans due to the interaction of the barotropic tide with bottom topography (Lamb, 2004; Johnston *et al.*, 2011) and in the atmosphere due to thunderstorms (Fovell *et al.*, 1992), and therefore provide a more realistic setting for instability. However, compared to sinusoidal waves, formal stability analysis of wave beams based on Floquet theory is far more demanding, as it requires solving an eigenvalue problem that involves an infinite number of differential, rather than algebraic, equations.

In view of this difficulty, Karimi & Akylas (2014) (hereafter referred to as KA14) proposed a simplified treatment of PSI assuming that two fine-scale subharmonic wave packets at half the beam frequency interact with a small-amplitude beam of locally confined profile. This model brings out the significance of the finite width of a beam: the subharmonic perturbations travel with their group velocity so, to cause instability, they must interact with the beam for long enough time before leaving the beam region. By comparing the wavepacket travel time across the beam with the duration of resonant interaction in the beam vicinity, KA14 argued that small-amplitude finite-width beams generally are not susceptible to PSI. An exception arises when the locally confined beam profile is nearly monochromatic, in which case PSI is possible if the number of carrier wavelengths within the beam width is sufficiently large. The stabilizing effect of the finite width of a beam is also supported by laboratory experiments (Bourget *et al.*, 2014), although the nearly inviscid flow scalings assumed in KA14 cannot be met in a laboratory setting. Furthermore, using a small-amplitude nearly inviscid model similar to KA14, Karimi & Akylas (2017) (henceforth referred to as KA17) showed that PSI is possible for beams with general spatial profile if the beam frequency $\omega \approx 2f$ (where f is the inertial frequency) because in this instance subharmonic perturbations with half the beam frequency are near-inertial and thus have nearly vanishing group velocity.

The original scope of the present investigation was to assess the validity of the PSI models of KA14 and KA17 by making a comparison against a formal linear stability analysis based on Floquet theory of small-amplitude wave beams under nearly inviscid flow conditions. The first successful Floquet stability analysis of wave beams was made in a very recent study (Onuki & Tanaka, 2019) by exploiting the fact that the Floquet multipliers, which determine stability, are tied to the eigenvalues of the so-called monodromy matrix which is easily computed by time integration. The emphasis of Onuki & Tanaka (2019), however, is on two- and three-dimensional instabilities of steep beams, far from the PSI regime considered in KA14 and KA17, so our intent was to fill this gap by applying the technique of Onuki & Tanaka (2019) to small-amplitude beams.

In carrying out this programme, we encountered difficulties obtaining quantitative agreement of the instability growth rates predicted by KA17 with those of the Floquet stability analysis for near-inertial PSI. This led us to study afresh the Floquet stability eigenvalue problem in the limit pertinent to the models of KA14 and KA17, namely a small-amplitude beam subject to fine-scale perturbations under nearly inviscid flow conditions. It transpires that the unstable Floquet mode in near-inertial PSI (beam frequency $\omega \approx 2f$) is dominated by two subharmonic wavepackets with carrier frequency $\omega/2$, as assumed in KA17; however, the two relatively small additional components at the frequency $3\omega/2$, which were ignored in KA17, also contribute to the stability eigenvalue problem and hence affect the instability growth rate. Once this contribution is taken into account, the predictions of the revised KA17 model are in excellent agreement with the Floquet stability analysis. A similar omission was also made in the PSI analysis of nearly-monochromatic beams by KA14, but in this instance the components at the frequency $3\omega/2$ do not affect the instability growth rate, and the predictions of KA14 agree well with their Floquet stability counterparts.

Apart from bringing out the significance of the $3\omega/2$ frequency components in the PSI of wave beams, our asymptotic analysis of the Floquet eigenvalue problem also reveals that PSI, which assumes that the frequency components $\omega/2$ are dominant, is limited by how fine-scale the perturbations are for a given beam amplitude (assumed small). Specifically, as the perturbation wavenumber is increased holding the beam amplitude fixed, higher-frequency components eventually come into play so the frequency spectrum of the Floquet mode broadens. Furthermore, this broadband instability, which is beyond the reach of KA14 and KA17, persists in the nearly inviscid limit for small-amplitude beams with general (not necessarily nearly monochromatic) profile even far from near-inertial conditions.

3.2 Floquet stability analysis

3.2.1 General formulation

The present analysis assumes an unbounded, incompressible, uniformly stratified Boussinesq fluid with constant buoyancy frequency N_* and includes the effect of background rotation under the f-plane approximation. Using nondimensional variables with $1/N_*$ as the time scale and L_* as the length scale (to be specified later) the governing equations for the velocity field $\boldsymbol{u}$, the reduced density ρ and pressure p are

$$\boldsymbol{\nabla}\cdot\boldsymbol{u} = 0, \tag{3.1a}$$

$$\rho_t + \boldsymbol{u}\cdot\boldsymbol{\nabla}\rho = \boldsymbol{u}\cdot\boldsymbol{j}, \tag{3.1b}$$

$$\boldsymbol{u}_t + \boldsymbol{u}\cdot\boldsymbol{\nabla}\boldsymbol{u} + \boldsymbol{f}\times\boldsymbol{u} = -\boldsymbol{\nabla}p - \rho\boldsymbol{j} + \nu\nabla^2\boldsymbol{u}. \tag{3.1c}$$

Here, $\boldsymbol{j}$ is a vertical unit vector pointing upwards, $\boldsymbol{f} = f\boldsymbol{j}$, where f is the local Coriolis parameter normalized with N_*, and $\nu = \nu_*/N_*L_*^2$ is the inverse Reynolds number, where ν_* denotes the kinematic viscosity.

In the inviscid limit ($\nu = 0$), (3.1) admits time-harmonic plane wave solutions in the form of beams (Tabaei & Akylas, 2003) that feature general profile in the cross-beam (η-) direction, and are uniform in the along-beam (ξ-) and transverse horizontal (z-) directions (figure 3-1*a*). Specifically, the beam velocity components (u, v, w) in the coordinate system

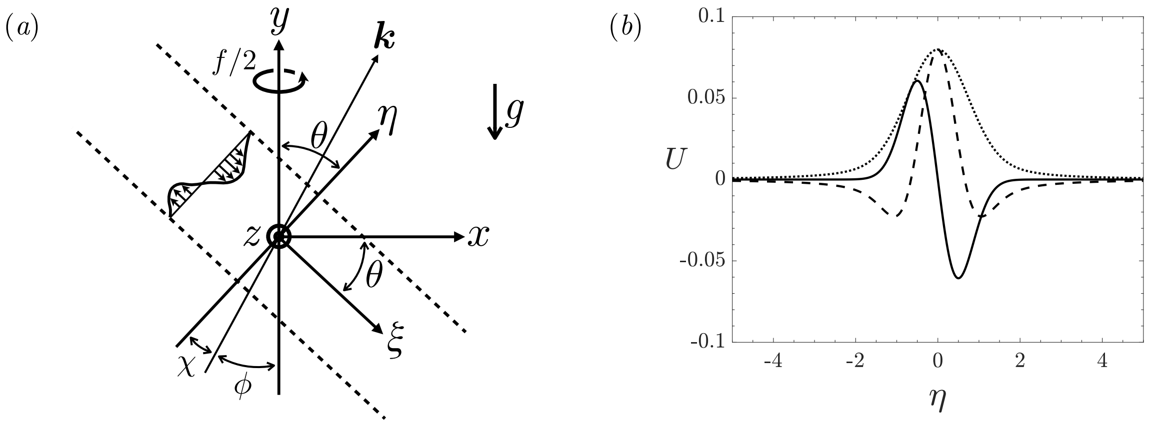

Figure 3-1: (a) Schematic of uniform beam with frequency ω and inclination θ to the horizontal, in keeping with (3.3). The coordinate system (ξ, η, z) is defined by the along-beam, cross-beam and transverse directions, respectively. Dotted lines indicate the finite width of the beam and the arrows within show the along-beam velocity u_0. The perturbation wavevector $\boldsymbol{k}$ is inclined by the angle χ to η and by $\phi = \theta - \chi$ to the vertical y. (b) Beam profile (3.8) for $\epsilon = 0.1$. Solid, dashed and dotted lines correspond to the real part, imaginary part and $|U|$, respectively.

(ξ, η, z), along with ρ and p, are given by

$$(u, v, w) = (u_0, 0, w_0) \equiv \Big(1, 0, \frac{\mathrm{i} f \cos\theta}{\omega}\Big) U(\eta) \mathrm{e}^{-\mathrm{i}\omega t} + \text{c.c.}, \tag{3.2a}$$

$$\rho = \rho_0(\eta, t) \equiv -\frac{\mathrm{i}\sin\theta}{\omega} U(\eta) \mathrm{e}^{-\mathrm{i}\omega t} + \text{c.c.}, \tag{3.2b}$$

$$p = p_0(\eta, t) \equiv \mathrm{i}(1 - f^2) \frac{\sin\theta\cos\theta}{\omega} \int^{\eta} U(\eta')\,\mathrm{d}\eta'\, \mathrm{e}^{-\mathrm{i}\omega t} + \text{c.c.}. \tag{3.2c}$$

Here, the complex amplitude $U(\eta)$ specifies the beam profile and θ is the beam inclination angle to the horizontal, which is tied to the beam frequency ω via the (nondimensional) dispersion relation

$$\omega^2 = f^2 + (1 - f^2)\sin^2\theta. \tag{3.3}$$

Furthermore, (ξ, η) are related to the horizontal and vertical coordinates (x, y) by $\xi = x\cos\theta - y\sin\theta$ and $\eta = x\sin\theta + y\cos\theta$. Generally, finite viscosity ($\nu \neq 0$) will introduce along-beam variations in (3.2) (Mowbray & Rarity, 1967; Thomas & Stevenson, 1972). These viscous effects are ignored here.

The focus of the present analysis is on the stability of the primary wave (3.2) to infinitesimal perturbations. As (3.2) does not depend on ξ or z, we superimpose normal modes in the form

$$u = u_0 + \hat{u}(\eta, t)\mathrm{e}^{\mathrm{i}(\mu\xi + mz)}, \tag{3.4}$$

where the real parameters μ and m specify the along-beam and transverse wavenumbers of the perturbation, with similar expressions for v, w, ρ, and p. After inserting into (3.1) and linearizing with respect to the perturbations, we obtain the following equations (dropping the hats),

$$
\begin{aligned}
0 &= \mathrm{i}\mu u + v_\eta + \mathrm{i}mw, && (3.5\text{a})\\
\rho_t &= -\mathrm{i}(\mu u_0 + m w_0)\rho - \rho_{0\eta} v - u\sin\theta + v\cos\theta, && (3.5\text{b})\\
u_t &= -\mathrm{i}(\mu u_0 + m w_0)u - u_{0\eta} v - \mathrm{i}\mu p + \rho\sin\theta - wf\cos\theta + \nu\mathscr{L}u, && (3.5\text{c})\\
v_t &= -\mathrm{i}(\mu u_0 + m w_0)v - p_\eta - \rho\cos\theta - wf\sin\theta + \nu\mathscr{L}v, && (3.5\text{d})\\
w_t &= -\mathrm{i}(\mu u_0 + m w_0)w - w_{0\eta} v - \mathrm{i}mp + uf\cos\theta + vf\sin\theta + \nu\mathscr{L}w, && (3.5\text{e})
\end{aligned}
$$

where $\mathscr{L} \equiv -\mu^2 + \partial^2_{\eta\eta} - m^2$ takes into account the full effects of viscosity on the perturbations. As the basic state (3.2) is periodic in t (period $T_0 = 2\pi/\omega$), (3.5) is a linear equation system with periodic coefficients, which can be solved by applying Floquet theory to determine stability for a given beam profile $U(\eta)$ and parameters μ and m.

3.2.2 Sinusoidal waves

For a sinusoidal plane wave, the primary wave profile in (3.2) is taken in the form $U = \epsilon\exp(\mathrm{i}\eta)$, where the amplitude parameter $\epsilon = U_*/(N_* L_*)$, U_* being half the along-ξ velocity amplitude, and the wavelength has been normalised to 2π (which fixes the length scale L_*). In this instance, it is straightforward to solve (3.5) via Floquet theory by expanding the perturbations in Fourier series in $\eta - \omega t$, and thus recover the thoroughly studied instability of a sinusoidal plane wave (e.g. Sonmor & Klaassen, 1997). Out of this body of work, of special interest here is the nearly inviscid ($\nu \ll 1$) small-amplitude limit ($\epsilon \ll 1$). In this regime, the most unstable perturbation is two-dimensional (i.e. $m = 0$) and involves only two subharmonic frequency components that are freely propagating sinusoidal internal waves and form a resonant triad with the primary wave. Specifically, these subharmonic waves, with frequencies (ω_1, ω_2) (where $|\omega_{1,2}| < \omega$) and wavevectors $(\boldsymbol{k}_1, \boldsymbol{k}_2)$, each satisfy the dispersion relation (3.3), and together satisfy the triad resonance conditions

$$
\begin{aligned}
\omega_1 + \omega_2 &= \omega, && (3.6\text{a})\\
\boldsymbol{k}_1 + \boldsymbol{k}_2 &= \boldsymbol{k}_0, && (3.6\text{b})
\end{aligned}
$$

where $\boldsymbol{k}_0 = \hat{\boldsymbol{e}}_\eta$ is the primary wavevector. This class of instabilities, which encompasses all such pairs of $(\omega_1, \boldsymbol{k}_1)$ and $(\omega_2, \boldsymbol{k}_2)$, is thus known as TRI.

For inviscid flow conditions, in the event that the beam inclination angle $\theta \gtrsim 43°$ for $f = 0$, or when $\omega \approx 2f$ for any θ, the most unstable pairs of subharmonic waves feature $\omega_1 \approx \omega_2 \approx \omega/2$ and $|\boldsymbol{k}_1| \approx |\boldsymbol{k}_2| \gg 1$ (e.g. Yeh & Liu, 1981; Sonmor & Klaassen, 1997). This particular form of TRI is widely known as PSI. However, it is important to note that other flow conditions may favour other forms of TRI over PSI. For instance, the most unstable triads for $\theta \lesssim 43°$ and $f = 0$ involve subharmonic waves with $|\boldsymbol{k}_1| < 1 < |\boldsymbol{k}_2|$, which is sometimes referred to as the 'branch-C' instability (Sonmor & Klaassen, 1997) or 'elastic scattering' and 'induced diffusion' (McComas & Bretherton, 1977).

3.2.3 Locally confined beams

Moving away from the sinusoidal wave, KA14 and KA17 examined the possibility of PSI for locally confined beams in the small-amplitude nearly inviscid limit. As discussed in §3.1, however, these models of PSI for localised beams are based upon the assumption of triad resonance, a mechanism originally uncovered by solving the full stability problem (3.5) for a sinusoidal primary wave. Here, to assess the validity of KA14 and KA17, we return to (3.5) and perform a formal stability analysis of a locally confined beam profile $U(\eta)$. In general, this task has to be carried out numerically.

The stability problem (3.5) is far more challenging to handle numerically for a general profile $U(\eta)$ than for the sinusoidal wave profile: in addition to Fourier expansion in t, it is necessary to use a separate discretization in η. To tackle this difficulty, we make use of the approach taken by Onuki & Tanaka (2019) in their stability analysis of finite-amplitude beams under oceanic flow conditions. This approach was also used by the current authors in a very recent study of the instability dynamics of large-amplitude thin beams generated by an oscillating cylinder under laboratory flow conditions (Fan & Akylas, 2020*a*).

As our interest centres on the relevance of PSI to small-amplitude locally confined beams, we focus on two-dimensional perturbations ($m = 0$), although the solution procedure outlined below is valid generally. It should be noted that three-dimensional ($m \neq 0$) instabilities are possible and may be important at large amplitudes (Onuki & Tanaka, 2019). Furthermore, other three-dimensional instability mechanisms such as streaming, which involves the generation of a resonant mean flow due to finite transverse variations of a beam (Kataoka & Akylas, 2015; Fan *et al.*, 2018; Jamin *et al.*, 2020) and thus falls beyond the scope of linear stability analysis, may be important in other contexts.

Following Onuki & Tanaka (2019), we solve (3.5) using the 'monodromy' matrix, which can be easily computed using time-integration. First, we eliminate v and p from (3.5) and discretize in η to obtain the matrix equation

$$\frac{\mathrm{d}X}{\mathrm{d}t} = A(t)X, \tag{3.7}$$

where $X = \{u, w, \rho\}$ is the state vector and $A(t) = A(t + T_0)$ is the periodic matrix that results from the right-hand side of (3.5). Based on Floquet theory, a fundamental solution matrix to (3.7) is given by $\mathbb{X}(t) = \mathrm{e}^{Bt}P(t)$, where $\mathbb{X} = \{X_1, X_2, ...\}$ is composed of linearly independent solutions to (3.7), B is a constant matrix whose eigenvalues are the Floquet exponents $\lambda = \lambda_r + \mathrm{i}\lambda_i$, and $P(t) = P(t + T_0) = \{P_1, P_2, ...\}$ is a periodic matrix composed of the Floquet modes. Because P is T_0-periodic, it follows that $\mathbb{X}(T_0) = M\mathbb{X}(0)$, where $M \equiv \mathrm{e}^{BT_0}$ is the so-called monodromy matrix and represents the effect of the operator

A over one period (i.e. the linearized Poincaré map). To find M, we set $\mathbb{X}(0) = I$, the identity matrix, as the initial condition, integrate (3.7) over one period to obtain $\mathbb{X}(T_0)$, and compute $M = \mathbb{X}(0)^{-1}\mathbb{X}(T_0)$. Next, we compute the eigenvalues of M, denoted α, to obtain the Floquet exponents $\lambda = (\log \alpha)/T_0$. By definition of the Floquet exponent, $X \propto \exp(\lambda t)$ so $\mathrm{Re}(\lambda) \equiv \lambda_r > 0$ implies instability. Finally, we repeat this procedure for various μ in order to find the instability modes with the highest growth rate. In implementing this procedure, we typically employed 1024 Fourier modes for discretizing (3.5) in the computational domain $\eta \in [-10, 10]$, and (3.7) was integrated using a pseudo-spectral method with fourth-order Runge–Kutta time stepping and a typical $\Delta t = 0.02$. The ensuing eigenvalue problem was then solved using standard MATLAB algorithms.

3.3 Floquet stability of beams with $\omega = 2f$

3.3.1 Results

We begin by considering finite-width beams in the presence of background rotation and attempt a comparison of the Floquet stability results with the predictions of the near-inertial PSI theory of KA17. This approximate model focuses on the resonant interaction between a small-amplitude wave beam with frequency $\omega \approx 2f$ and two subharmonic perturbations of frequency $\omega/2 \approx f$ and very fine wavelength. According to KA17, the vanishing group velocity of such near-inertial perturbations prolongs their interaction with the primary wave. As a result, when $\omega \approx 2f$, small-amplitude locally confined beams of general profile are susceptible to PSI in the nearly inviscid limit.

We first present Floquet stability results for a small-amplitude beam with the Gaussian profile used in KA17, exactly at the critical frequency $\omega = 2f$ and for inviscid flow conditions ($\nu = 0$). Specifically, we chose $U(\eta)$ in (3.2) to be

$$U(\eta) = \frac{\epsilon}{\sqrt{8\pi}} \int_0^\infty \mathrm{i}l \mathrm{e}^{-l^2/8} \mathrm{e}^{\mathrm{i}l\eta} \, \mathrm{d}l \tag{3.8}$$

and set $\omega = 0.1$. Here, the nondimensional amplitude parameter $\epsilon = U_*/N_*L_*$, where U_* and L_* are a characteristic (dimensional) velocity and width, respectively, of the primary wave beam. Combined with (3.2), the profile (3.8) (figure 3-1*b*) corresponds to a unidirectional (progressive) wave beam that transports energy in the positive ξ-direction (figure 3-1*a*).

Figure 3-2(*a*) plots the computed Floquet growth rates λ_r, scaled by the beam amplitude parameter $\epsilon = 0.01$, as a function of the along-beam (ξ-) wavenumber μ of the perturbations. Instability first arises around $\mu \approx 1$, and growth rates increase monotonically with μ until they eventually saturate to approximately 0.126 at $\mu = 20$. Figure 3-2(*b*) plots the time-frequency spectra of the Floquet modes corresponding to the growth rates shown in figure 3-2(*a*) at representative values of $\mu = 2.4$, 8.6 and 17. At low values of μ (e.g. $\mu = 2.4$), the frequency spectrum is dominated by two frequency components at approximately $\pm f$, matching the description of near-inertial PSI in KA17. However, as μ increases, the frequency spectrum broadens and the components at $\pm f$ are no longer the dominant frequencies. For example, at $\mu = 17$, the dominant frequencies are now approximately $\pm 3f$. As μ is further increased, the frequency spectrum continues to broaden and increasingly large frequencies dominate. It should be noted that the different frequency components are discretized with spacing equal to ω in keeping with Floquet theory: the Floquet mode must be periodic with the same period as the basic state plus a constant offset term due to the imaginary part of the Floquet exponent.

Figure 3-2(e) plots the spatial disturbances that correspond to the top four frequency components, in order of power, of the Floquet mode found at $\mu = 2.4$, which are the components at $\pm f$, followed by $\pm 3f$. All four spatial disturbances take the form of wavepackets with a well-defined carrier and locally-confined envelope. Interestingly, the carrier wavenumbers γ of each of the four spatial disturbances, corresponding to the peak of the spatial Fourier spectrum, are all approximately equal, in this case to roughly -30. Figure 3-2(f) shows similar results for the Floquet mode found at $\mu = 8.6$, in which case $\gamma \approx -100$. In fact, all frequency components of a computed Floquet mode, and not just the top four, have approximately equal γ. Furthermore, figure 3-2(b–d) indicates that the frequency components of a given Floquet mode always appear in plus/minus pairs, while γ is always negative.

According to the above numerical results, the Floquet mode is a superposition of pairs of wavepackets, and each pair consists of waves that have approximately the same frequency and wavenumber but travel in opposite directions. Since the Floquet mode has a fixed along-beam wavenumber μ, the carrier wavevector $\boldsymbol{k} = \mu\hat{\boldsymbol{e}}_\xi + \gamma\hat{\boldsymbol{e}}_\eta$ is approximately constant for all frequency components. Moreover, since $|\gamma| \gg |\mu| = O(1)$, $\boldsymbol{k}$ is nearly aligned with the η-direction (the angle $\chi \ll 1$ in figure 3-1a) and the perturbation wavepackets have very fine scale relative to the primary beam, i.e. $|\boldsymbol{k}| \gg 1$, consistent with KA17 in so far as the subharmonic perturbations are concerned. In view of the dispersion relation (3.3), the beam inclination angle $\theta \approx 5°$ for $\omega = 0.1$ and $f = \omega/2$, so $\boldsymbol{k}$, whose inclination to the vertical is $\phi = \theta - \chi \ll 1$ (figure 3-1a), points nearly vertically. Therefore, only the subharmonic components at $\pm\omega/2$ approximately satisfy the dispersion relation for the wavevector $\boldsymbol{k}$ and correspond essentially to freely propagating internal waves.

3.3.2 Floquet stability vs. near-inertial PSI

The Floquet stability results for a small-amplitude beam ($\epsilon = 0.01$) with $\omega = 2f$ discussed above suggest that the instability dynamics assumed by KA17 for near-inertial PSI is valid only as long as the fine-scale perturbations have moderately large $|\boldsymbol{k}|$ (see figure 3-2b,e): when μ and thereby $|\boldsymbol{k}|$ is increased while keeping ϵ fixed (e.g. figure 3-2c,d,f), the main hypothesis of PSI breaks down because the instability dynamics is no longer dominated by the subharmonic frequencies $\pm\omega/2$. These findings are consistent with the asymptotic scaling $|\boldsymbol{k}| = O(\epsilon^{-1/2})$ of KA17, which is clearly violated as $|\boldsymbol{k}| \to \infty$ for fixed ϵ. As a result

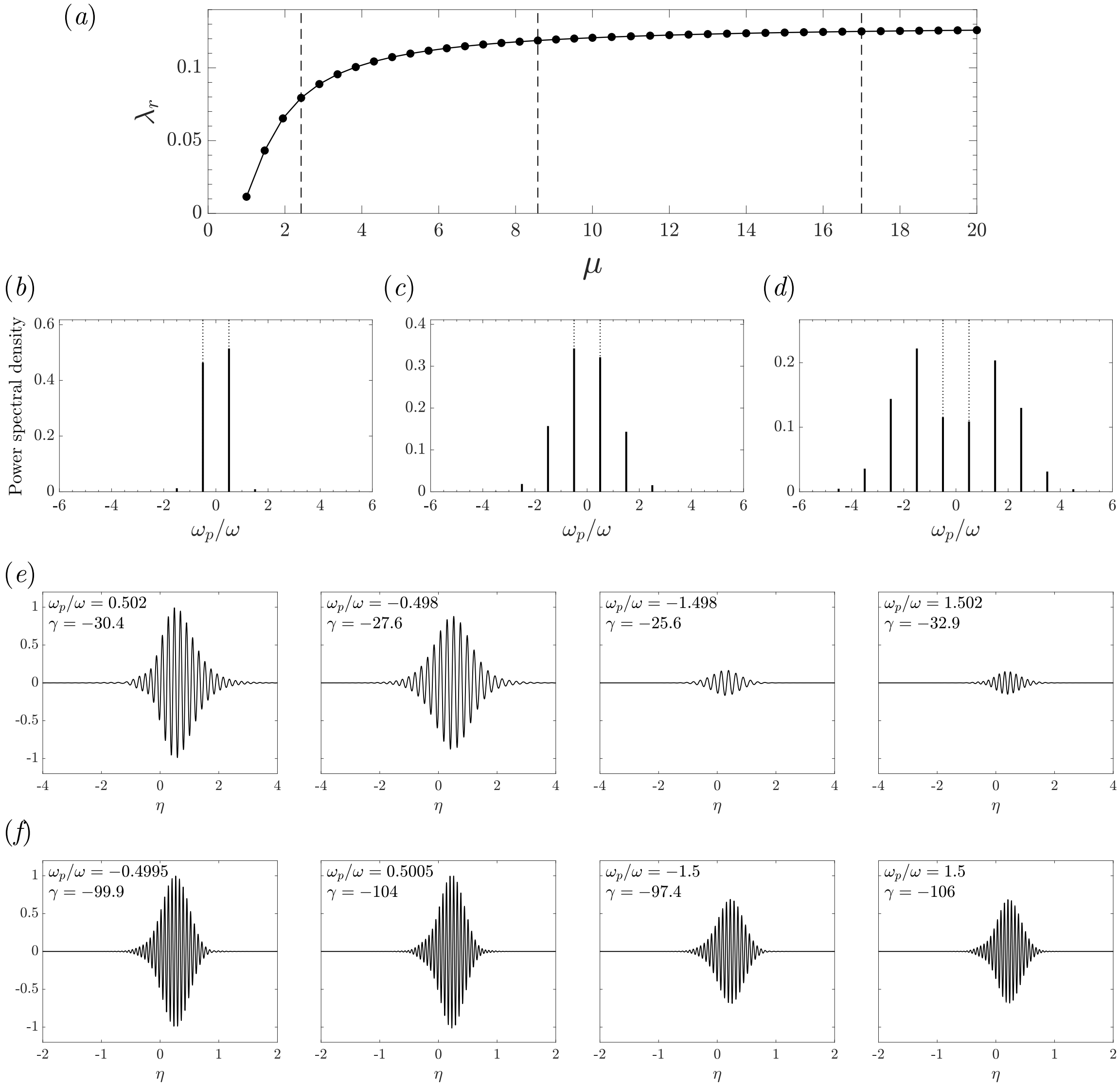

Figure 3-2: (a) Instability growth rates (scaled by the beam amplitude $\epsilon = 0.01$) predicted by the Floquet stability analysis as a function of the along-beam (ξ-) wavenumber μ of the perturbations, for primary beam profile (3.8), beam frequency $\omega = 0.1$, Coriolis parameter $f = 0.05$, and inviscid flow conditions ($\nu = 0$). (b) Time frequency spectrum of the fastest growing Floquet mode for $\mu = 2.4$, indicated in (a) by a vertical dashed line. Vertical dotted lines indicate the frequencies $\pm f/\omega$. (c) and (d) Same as (b) but for $\mu = 8.6$ and 17, respectively. (e) Spatial mode shapes for the top four frequencies, in order of power, of the frequency spectrum plotted in (b) for the Floquet mode at $\mu = 2.4$. From left to right, plots are shown in order of decreasing power. The spatial mode amplitudes have been normalised such that the mode corresponding to the top frequency component has maximum along-beam velocity equal to unity. The peak cross-beam (η-) wavenumber γ of each mode is listed along with the frequency. (f) Same as (e) but for the top four frequencies, in order of power, of the frequency spectrum plotted in (c) for the Floquet mode at $\mu = 8.6$.

of this restriction on $|\boldsymbol{k}|$, PSI does not capture the dominant inviscid instability (largest growth rate) which arises as $|\boldsymbol{k}| \to \infty$ (figure 3-1*a*). More importantly, however, quantitative comparison between the growth rates predicted by KA17 and our Floquet analysis revealed noticeable discrepancies even when PSI is valid (e.g. for $\mu = 2.4$ in figure 3-1*b*,*e*).

To understand and resolve these issues, we now turn to an asymptotic stability analysis of finite-width beams in the joint limit $\epsilon \ll 1$ and $|\boldsymbol{k}| \gg 1$, based on the full stability problem (3.5).

3.4 Small-amplitude limit of Floquet problem

3.4.1 Preliminaries

Since PSI is a two-dimensional instability, the following analysis assumes from the outset perturbations that only vary in the plane of the basic state (i.e. $m = 0$ in (3.4)). In this setting, rather than u and v, it is more convenient to introduce a streamfunction $\psi(\xi, \eta, t)$, in terms of which $u = \psi_\eta$ and $v = -\psi_\xi$. Thus, the incompressibility equation (3.1a) is automatically satisfied, and ψ, w and ρ are governed by the vorticity equation

$$\nabla^2\psi_t - \cos\theta\rho_\xi - \sin\theta\rho_\eta - f\sin\theta w_\xi + f\cos\theta w_\eta + J(\nabla^2\psi, \psi) - \nu\nabla^4\psi = 0, \tag{3.9}$$

along with the transverse momentum and continuity equations

$$w_t + f\sin\theta\psi_\xi - f\cos\theta\psi_\eta + J(w, \psi) - \nu\nabla^2 w = 0, \tag{3.10a}$$

$$\rho_t + \cos\theta\psi_\xi + \sin\theta\psi_\eta + J(\rho, \psi) = 0, \tag{3.10b}$$

where the Jacobian $J(a, b) = a_\xi b_\eta - a_\eta b_\xi$. Furthermore, in terms of the streamfunction, the basic state (3.2) that describes a uniform internal wave beam is replaced by

$$\psi_0 = \epsilon\, Q(\eta)\mathrm{e}^{-\mathrm{i}\omega t} + \text{c.c}, \tag{3.11a}$$

$$w_0 = \epsilon\frac{\mathrm{i}f\cos\theta}{\omega}Q_\eta\mathrm{e}^{-\mathrm{i}\omega t} + \text{c.c}, \tag{3.11b}$$

$$\rho_0 = -\epsilon\frac{\mathrm{i}\sin\theta}{\omega}Q_\eta\mathrm{e}^{-\mathrm{i}\omega t} + \text{c.c}, \tag{3.11c}$$

where $Q(\eta)$ and the beam profile $U(\eta)$ in (3.2) are related by $\epsilon\, Q_\eta = U$, and ϵ is the amplitude parameter used earlier in (3.8).

As in (3.4), we superimpose infinitesimal perturbations to this basic state in the form of normal modes

$$\psi = \psi_0 + \hat{\psi}(\eta, t)\mathrm{e}^{\mathrm{i}\mu\xi}, \tag{3.12}$$

with similar expressions for w and ρ, where μ is a real along-beam wavenumber parameter. Furthermore, in keeping with Floquet theory, $\hat{\psi}$ is expanded as a Fourier series in t with period $2\pi/\omega$, multiplied with an exponential term that contains the Floquet exponent λ:

$$\hat{\psi} = \mathrm{e}^{\lambda t} \sum_{n=-\infty}^{\infty} \hat{\psi}^{(n)}(\eta)\mathrm{e}^{\mathrm{i}n\omega t}, \tag{3.13}$$

with analogous expressions for $\hat{w}$ and $\hat{\rho}$. Inserting then (3.12) and (3.13) into (3.9) and (3.10) and linearizing leads to a set of infinite homogeneous equations for the perturbation amplitudes $\hat{\psi}^{(n)}, \hat{w}^{(n)}$ and $\hat{\rho}^{(n)}$, where $n = 0, \pm 1, \pm 2, \ldots$. This eigenvalue problem for λ, which determines stability, is of course equivalent to the one obtained earlier from (3.5) and can be solved numerically by a similar procedure as in §3.2.3.

Rather than proceeding numerically, however, here we seek an asymptotic approximation to this Floquet eigenvalue problem in the limit of a small-amplitude beam ($\epsilon \ll 1$) subject to fine-scale perturbations ($|\boldsymbol{k}| \gg 1$) in a nearly inviscid fluid ($\nu \ll 1$), the conditions under which PSI comes into play according to the numerical results in §3.3.1. Specifically, as seen in figure 3-2(e), the spatial mode shapes $\hat{\psi}^{(n)}(\eta)$ in (3.13) take the form of wavepackets with a common carrier wavenumber γ in the cross-beam (η-) direction. Therefore, we write

$$\left(\hat{\psi}^{(n)}, \hat{w}^{(n)}, \hat{\rho}^{(n)}\right) = \left(A^{(n)}(\eta), W^{(n)}(\eta), R^{(n)}(\eta)\right)\mathrm{e}^{\mathrm{i}\gamma\eta}. \tag{3.14}$$

Furthermore, we express the along- and cross-beam wavenumbers as

$$\mu = -k\sin\chi, \qquad \gamma = k\cos\chi, \tag{3.15}$$

where

$$k = \sqrt{\mu^2+\gamma^2}, \qquad \chi = \tan^{-1}(-\mu/\gamma) \tag{3.16}$$

are the magnitude and inclination angle to the η-direction, respectively, of the carrier wavevector $\boldsymbol{k} = \mu\hat{\boldsymbol{e}}_\xi + \gamma\hat{\boldsymbol{e}}_\eta$ (see figure 3-1a). Finally, to bring out the perturbation components with frequency $\omega/2$, without loss of generality, we take

$$\lambda \to \lambda - \mathrm{i}\frac{\omega}{2}. \tag{3.17}$$

As a result of the substitutions (3.14)–(3.17), the Floquet mode in (3.12) takes the form

$$\hat{\psi}(\eta, t)\mathrm{e}^{\mathrm{i}\mu\xi} = \mathrm{e}^{\lambda t}\mathrm{e}^{-\mathrm{i}\omega t/2}\mathrm{e}^{\mathrm{i}k(\eta\cos\chi - \xi\sin\chi)} \sum_{n=-\infty}^{\infty} A^{(n)}(\eta)\mathrm{e}^{\mathrm{i}n\omega t}, \tag{3.18}$$

with similar expressions for $\hat{w}$ and $\hat{\rho}$. Furthermore, upon substituting (3.12) and (3.18) into (3.9) and (3.10), linearizing and collecting equal harmonics, it follows that the perturbation amplitudes $\tilde{A}^{(n)} = kA^{(n)}, W^{(n)}$ and $R^{(n)}$ ($n = 0, \pm 1, \pm 2, \ldots$) satisfy the infinite equation system

$$\begin{aligned}&\Big[\lambda+\mathrm{i}\Big(n-\frac{1}{2}\Big)\omega\Big]\mathbb{L}\tilde{A}^{(n)}+\mathrm{i}\Big(\sin\phi\,R^{(n)}-f\cos\phi\,W^{(n)}\Big)+\frac{1}{k}\Big(\sin\theta\,R^{(n)}_{\eta}-f\cos\theta\,W^{(n)}_{\eta}\Big)\\&\quad-\epsilon k\,\mathrm{i}\sin\chi\Big\{\Big(Q_{\eta}\mathbb{L}A^{(n+1)}+Q^{*}_{\eta}\mathbb{L}\tilde{A}^{(n-1)}\Big)+\frac{1}{k^{2}}\Big(Q_{\eta\eta\eta}\tilde{A}^{(n+1)}+Q^{*}_{\eta\eta\eta}\tilde{A}^{(n-1)}\Big)\Big\}\\&\quad+\nu k^{2}\mathbb{L}^{2}\tilde{A}^{(n)}=0,\end{aligned}\tag{3.19a}$$

$$\begin{aligned}&\Big[\lambda+\mathrm{i}\Big(n-\frac{1}{2}\Big)\omega\Big]W^{(n)}-\mathrm{i}f\cos\phi\,\tilde{A}^{(n)}-\frac{f\cos\theta}{k}\,\tilde{A}^{(n)}_{\eta}+\nu k^{2}\mathbb{L}W^{(n)}\\&\quad-\epsilon k\,\mathrm{i}\sin\chi\Big\{\Big(Q_{\eta}W^{(n+1)}+Q^{*}_{\eta}W^{(n-1)}\Big)-\frac{\mathrm{i}f\cos\theta}{k\omega}\Big(Q_{\eta\eta}\tilde{A}^{(n+1)}-Q^{*}_{\eta\eta}\tilde{A}^{(n-1)}\Big)\Big\}=0,\end{aligned}\tag{3.19b}$$

$$\begin{aligned}&\Big[\lambda+\mathrm{i}\Big(n-\frac{1}{2}\Big)\omega\Big]R^{(n)}+\mathrm{i}\sin\phi\,\tilde{A}^{(n)}+\frac{\sin\theta}{k}\,\tilde{A}^{(n)}_{\eta}\\&\quad-\epsilon k\,\mathrm{i}\sin\chi\Big\{\Big(Q_{\eta}R^{(n+1)}+Q^{*}_{\eta}R^{(n-1)}\Big)+\frac{\mathrm{i}\sin\theta}{k\omega}\Big(Q_{\eta\eta}\tilde{A}^{(n+1)}-Q^{*}_{\eta\eta}\tilde{A}^{(n-1)}\Big)\Big\}=0,\end{aligned}\tag{3.19c}$$

where

$$\mathbb{L}=1-\frac{2\mathrm{i}\cos\chi}{k}\frac{\mathrm{d}}{\mathrm{d}\eta}-\frac{1}{k^{2}}\frac{\mathrm{d}^{2}}{\mathrm{d}\eta^{2}},\tag{3.20}$$

and $\phi=\theta-\chi$ is the inclination of $\boldsymbol{k}$ to the vertical (see figure 3-1*a*).

3.4.2 PSI regime

The eigenvalue problem (3.19), while equivalent to the one discussed in §3.2.3, is a convenient starting point for examining the limit $\epsilon\ll 1$ and $k\gg 1$ appropriate for PSI. Specifically, for $k\gg 1$, the amplitudes $(\tilde{A}^{(n)},W^{(n)},R^{(n)})$ of the various frequency components that comprise the Floquet mode (3.18) correspond to the envelopes of the wavepackets found numerically in figure 3-2(*e*,*f*). According to (3.19), these amplitudes are coupled via the terms proportional to ϵk. Therefore, when $\epsilon k=O(1)$, all frequency components may participate equally in the instability dynamics of a small-amplitude ($\epsilon\ll 1$) beam. This accounts for the results of figure 3-2(*c*,*d*), in which the frequency spectrum of the instability at fixed ϵ becomes increasingly broadband as μ (and therefore k) is increased.

By constrast, when

$$\epsilon k\ll 1\tag{3.21}$$

in (3.19), the amplitudes of the frequency components of the Floquet mode are weakly coupled. In this instance, it is possible to asymptotically truncate the Fourier series in (3.18) so that a finite number of frequency components dominate the instability dynamics, as is the case in PSI. Thus, we now turn our attention to the joint limit

$$\epsilon\ll 1,\qquad k\gg 1,\tag{3.22}$$

under the condition (3.21) and, as seen in figure 3-2(*b*), we assume that the frequencies $-\omega/2$ and $\omega/2$, which correspond to $n = 0$ and $n = 1$ in (3.18), dominate the instability. Then, from (3.19), the rest of the harmonics are less important

$$\left(\tilde{A}^{(n)}, W^{(n)}, R^{(n)}\right) = \begin{cases} O\big((\epsilon k)^{n-1}\big)\tilde{A}^{(1)} & (n \geq 2), \\ O\big((\epsilon k)^{|n|}\big)\tilde{A}^{(0)} & (n \leq -1). \end{cases} \tag{3.23}$$

Furthermore, after eliminating $W^{(0,1)}$ and $R^{(0,1)}$ and making use of (3.21)–(3.23), the equations for the dominant $n = 0$ and $n = 1$ components of (3.19) can be approximated as

$$\begin{aligned} &\Omega\tilde{A}^{(0)} - \omega\big(\lambda + \nu k^2\beta\big)\tilde{A}^{(0)} - \frac{\omega c}{k}\tilde{A}^{(0)}_{\eta} + \mathrm{i}\frac{3\omega^2}{4k^2}\tilde{A}^{(0)}_{\eta\eta} \\ &\quad + \epsilon k\,\mathrm{i}\sin\chi\left\{\Omega\frac{2}{\omega}Q_{\eta}\tilde{A}^{(1)} + Q^*_{\eta}\Big(\sin\phi\, R^{(-1)} - f\cos\phi\, W^{(-1)} + \frac{\omega}{2}\tilde{A}^{(-1)}\Big)\right\} \\ &\quad + \epsilon^2k^2\mathrm{i}\sin^2\chi\,|Q_{\eta}|^2\tilde{A}^{(0)} - \epsilon\frac{\sin\chi}{\omega}\Big\{3\delta Q_{\eta\eta}\tilde{A}^{(1)} + (4\delta - \omega^2\cos\chi)Q_{\eta}\tilde{A}^{(1)}_{\eta}\Big\} = O\Big(\frac{\epsilon}{k}, \epsilon^2 k\Big), \end{aligned} \tag{3.24a}$$

$$\begin{aligned} &\Omega\tilde{A}^{(1)} + \omega\big(\lambda + \nu k^2\beta\big)\tilde{A}^{(1)} - \frac{\omega c}{k}\tilde{A}^{(1)}_{\eta} + \mathrm{i}\frac{3\omega^2}{4k^2}\tilde{A}^{(1)}_{\eta\eta} \\ &\quad - \epsilon k\,\mathrm{i}\sin\chi\left\{\Omega\frac{2}{\omega}Q^*_{\eta}\tilde{A}^{(0)} - Q_{\eta}\Big(\sin\phi\, R^{(2)} - f\cos\phi\, W^{(2)} - \frac{\omega}{2}\tilde{A}^{(2)}\Big)\right\} \\ &\quad + \epsilon^2k^2\mathrm{i}\sin^2\chi\,|Q_{\eta}|^2\tilde{A}^{(1)} + \epsilon\frac{\sin\chi}{\omega}\Big\{3\delta Q^*_{\eta\eta}\tilde{A}^{(0)} + (4\delta - \omega^2\cos\chi)Q^*_{\eta}\tilde{A}^{(0)}_{\eta}\Big\} = O\Big(\frac{\epsilon}{k}, \epsilon^2 k\Big), \end{aligned} \tag{3.24b}$$

where

$$\Omega = \sin^2\phi + f^2\cos^2\phi - \frac{\omega^2}{4} \tag{3.25a}$$

$$\beta = \frac{1}{2}\left(1 + \frac{4f^2\cos^2\phi}{\omega^2}\right), \qquad \delta = \sin\phi\sin\theta + f^2\cos\phi\cos\theta, \tag{3.25b}$$

$$c = \frac{2}{\omega}\left(\delta - \frac{\omega^2}{4}\cos\chi\right). \tag{3.25c}$$

Here, in deriving (3.24), it is assumed that

$$\lambda \sim \nu k^2 \ll 1, \tag{3.26}$$

anticipating that in the weak-coupling limit (3.21) instability is weak, and including only the leading-order effects of viscosity.

The $O(1)$ terms in (3.24) drop out as the carrier wavevector $\boldsymbol{k}$ has to adhere to the dispersion relation (3.3) for the dominant frequencies $\pm\omega/2$, so $\Omega = 0$ in (3.25a). Furthermore, from (3.19), the amplitudes of the frequency components $\pm 3\omega/2$, to leading order, are given as

$$\tilde{A}^{(-1)} = -\epsilon k \frac{\sin\chi}{\omega} Q_\eta \tilde{A}^{(0)}, \qquad \tilde{A}^{(2)} = \epsilon k \frac{\sin\chi}{\omega} Q_\eta^* \tilde{A}^{(1)}, \tag{3.27}$$

with $R^{(-1,2)} = \pm 2\sin\phi\, \tilde{A}^{(-1,2)}/\omega$ and $W^{(-1,2)} = \mp 2f\cos\phi\, \tilde{A}^{(-1,2)}/\omega$. As a result, inserting (3.27) into (3.24), we find that all interaction terms at $O(\epsilon k)$ and $O(\epsilon^2 k^2)$ vanish, leaving the following closed system for $\tilde{A}^{(0)}$ and $\tilde{A}^{(1)}$:

$$\begin{aligned}\big(\lambda + \nu k^2 \beta\big)\tilde{A}^{(0)} + \frac{c}{k}\tilde{A}^{(0)}_\eta - \mathrm{i}\frac{3\omega}{4k^2}\tilde{A}^{(0)}_{\eta\eta} + \epsilon\frac{\sin\chi}{\omega^2}\Big\{3\delta Q_{\eta\eta}\tilde{A}^{(1)} + (4\delta - \omega^2\cos\chi)Q_\eta \tilde{A}^{(1)}_\eta\Big\} \\ = O\Big(\frac{\epsilon}{k}, \epsilon^2 k\Big),\end{aligned} \tag{3.28a}$$

$$\begin{aligned}\big(\lambda + \nu k^2 \beta\big)\tilde{A}^{(1)} - \frac{c}{k}\tilde{A}^{(1)}_\eta + \mathrm{i}\frac{3\omega}{4k^2}\tilde{A}^{(1)}_{\eta\eta} + \epsilon\frac{\sin\chi}{\omega^2}\Big\{3\delta Q^*_{\eta\eta}\tilde{A}^{(0)} + (4\delta - \omega^2\cos\chi)Q^*_\eta \tilde{A}^{(0)}_\eta\Big\} \\ = O\Big(\frac{\epsilon}{k}, \epsilon^2 k\Big).\end{aligned} \tag{3.28b}$$

These two coupled equations define an eigenvalue problem for λ that governs the stability of small-amplitude finite-width beams under the conditions (3.21), (3.22), and (3.26) appropriate to PSI. This reduced system captures the effects of the group velocity and dispersion of the subharmonic perturbation wavepackets, as well as the leading-order effects of the interaction of these wavepackets with the underlying beam, and weak viscosity. In view of (3.21) and (3.22), the $O(1/k)$ group velocity effect in (3.28) always dominates the $O(\epsilon)$ interaction of the perturbation with the beam, the only culprit in a potential instability. On these grounds it was argued in KA14 that a small-amplitude finite-width beam cannot suffer PSI in general.

There are two notable special cases, though: (i) near-inertial PSI (considered in KA17 and re-visited in §3.5 below), where the group velocity c in (3.25c) happens to be small; and (ii) PSI of a beam with nearly-monochromatic profile (considered in KA14 and re-visited in §3.6 below), where the triad interaction of the subharmonic perturbations with the beam is more finely tuned and can lead to instability. Conceivably, of course, a small-amplitude ($\epsilon \ll 1$) beam with general locally confined profile could be unstable to fine-scale ($k \gg 1$) perturbations with $\epsilon k = O(1)$, in which case the full eigenvalue problem (3.19) is appropriate. This possibility, which involves a broadband frequency spectrum and no longer qualifies as PSI, will be explored in §3.7.

3.5 Near-inertial PSI

3.5.1 Reduced eigenvalue problem

We now revisit near-inertial PSI in the light of the small-amplitude theory derived in the previous section and the numerical Floquet analysis of §3.3. To allow for slight deviations from the critical frequency $\omega = 2f$, we write

$$\omega = 2f + \sigma, \tag{3.29}$$

where $|\sigma| \ll 1$ is a detuning parameter.

Here, it is important to note that when $\omega < 2f$ (i.e. $\sigma < 0$), perturbations at half this frequency are sub-inertial ($\omega/2 < f$) so the dispersion relation $\Omega = 0$ in (3.24) cannot be satisfied by a real wavevector $\boldsymbol{k}$. However, it is still possible to allow for slightly sub-inertial subharmonic perturbations in our asymptotic approach by inserting (3.29) into (3.19) from the onset. This results in two additional terms, $\omega\sigma\tilde{A}^{(0)}/2$ in (3.24a) and $\omega\sigma\tilde{A}^{(1)}/2$ in (3.24b), which incorporate the effect of weak detuning. Since $\omega/2 = f$ to leading order, it is sufficient now to take $\phi = 0$ (i.e. $\boldsymbol{k}$ points vertically) so that $\Omega = 0$ and the $O(1)$ terms in (3.24) again drop out. Furthermore, for this choice of ϕ, the group velocity c of the perturbation wavepackets in (3.28) vanishes in view of (3.25). The remaining terms of (3.28) – which represent the effects of wavepacket dispersion, coupling to the underlying beam, viscous dissipation and departure from the critical frequency – may then be formally balanced by the scalings

$$\lambda \to \epsilon\lambda, \qquad \nu = \alpha\epsilon^2, \qquad k = \frac{\kappa}{\epsilon^{1/2}}, \qquad \sigma = \epsilon f \hat{\sigma}, \tag{3.30}$$

consistent with (3.22) and (3.26). In this 'distinguished limit', making also use of (3.25), the eigenvalue problem (3.28) reduces to

$$\left(\frac{\hat{\lambda}}{\omega/2} - \mathrm{i}\frac{\hat{\sigma}}{2}\right)\tilde{A}^{(0)} - \mathrm{i}\frac{3}{2\kappa^2}\tilde{A}^{(0)}_{\eta\eta} + \frac{3\sin 2\theta}{4\omega}\, Q_{\eta\eta}\tilde{A}^{(1)} = 0, \tag{3.31a}$$

$$\left(\frac{\hat{\lambda}}{\omega/2} + \mathrm{i}\frac{\hat{\sigma}}{2}\right)\tilde{A}^{(1)} + \mathrm{i}\frac{3}{2\kappa^2}\tilde{A}^{(1)}_{\eta\eta} + \frac{3\sin 2\theta}{4\omega}\, Q^{*}_{\eta\eta}\tilde{A}^{(0)} = 0. \tag{3.31b}$$

where

$$\hat{\lambda} = \lambda + \alpha\kappa^2. \tag{3.32}$$

For a given profile Q, the eigenvalues $\hat{\lambda}$ depend on the parameters $\omega, \hat{\sigma}$ and κ, and instability arises when $\hat{\lambda} > \alpha\kappa^2$. Accordingly, $\hat{\lambda}$ can be interpreted as the inviscid growth rate.

The stability problem (3.31) is similar, but not entirely equivalent, to the one obtained in KA17 for near-inertial PSI. Specifically, the present asymptotic analysis, which is based on the full Floquet stability problem (3.19), reveals the importance of the $\pm 3\omega/2$ frequency components (3.27) in the PSI dynamics: including these waves cancels out the terms proportional to $|Q_\eta|^2$ in (3.24), which thus do not appear in the final stability equations (3.31). In contrast, KA17 focuses solely on the $\pm\omega/2$ frequency components so these 'nonlinear refraction' terms erroneously are present in the stability eigenvalue problem of KA17 (*cf.* their equation 28). This resolves the discrepancy noted in §3.3.2 between KA17 and the numerical Floquet analysis: the predictions of the eigenvalue problem (3.31) are in excellent agreement with Floquet numerical results for near-inertial PSI, as discussed below. Furthermore, it should be noted that KA17 assumes $\omega \geq 2f$, whereas our analysis permits the detuning parameter to be of either sign, encompassing both super- and sub-inertial perturbations. The present, more general, treatment reduces to that of KA17 by setting $\hat{\sigma} = \sigma_{\mathrm{KA}}^2(1-f^2)/f^2$ and $(A^{(0)}, A^{(1)}) \rightarrow (A^{(0)}, A^{(1)}) \exp(\mathrm{i}\kappa\sigma_{\mathrm{KA}}\eta/\sin\theta)$, where σ_{KA} is the detuning parameter used in KA17.

3.5.2 Instability growth rates

We now proceed to compare the predictions of (3.31) against the results of the numerical Floquet analysis of §§3.2.3 and 3.3. To this end, Q in (3.31) is chosen as

$$Q(\eta) = \frac{1}{\sqrt{8\pi}} \int_0^\infty \mathrm{e}^{-l^2/8} \mathrm{e}^{\mathrm{i}l\eta}\, \mathrm{d}l\,, \tag{3.33}$$

which corresponds to the same beam profile (3.8) used earlier (and also matches the profile used in KA17). Furthermore, as in §3.3, $\omega = 0.1$ and all reported real growth rates λ_r will be in the scaled time $T = \epsilon t$ consistent with (3.30). Numerically, the eigenvalue problem (3.31) was discretized in η using 8th-order centred differences and the resulting matrix eigenvalue problem was solved using standard numerical eigenvalue algorithms in MATLAB for the eigenvalue $\hat{\lambda}$. The computational domain was varied between $\eta \in [-5, 5]$ and $[-100, 100]$, depending on the choices of κ and $\hat{\sigma}$, with a typical grid size of 2000 points.

Figure 3-3 compares the instability growth rates λ_r predicted by the numerical Floquet analysis and the near-inertial PSI theory (3.31) under various flow conditions. Specifically, the PSI growth rates are plotted as a function of the perturbation wavenumber $\kappa > 0$ for viscosity parameter $\alpha = 0$ and 10^{-3}, and detuning parameter $\hat{\sigma} = -4, -2, 0, 4, 10$, and 20. The corresponding Floquet growth rates are shown for beam amplitude $\epsilon = 0.002$, with κ computed using (3.16) and (3.30), where γ is taken to be the average of the carrier wavenumbers (in η) of the two subharmonic frequency components.

Overall, we observe excellent quantitative agreement between the fully numerical and the asymptotic instability growth rates. In the inviscid case ($\alpha = 0$) shown in figure 3-3(*a*,*c*), $\lambda_r = \hat{\lambda}_r$ saturates to an approximatively constant value for large κ that depends on the detuning $\hat{\sigma}$. As $|\hat{\sigma}|$ increases, i.e. as $\omega/2$ moves away from f, this limiting growth rate is diminished, a stabilizing effect that is stronger for $\hat{\sigma} < 0$ (i.e. $\omega/2 < f$). In this instance, the computed PSI growth rates have zero imaginary part ($\lambda_i = 0$) so in view of (3.18), sub-inertial subharmonic perturbations have frequency exactly equal to $\omega/2$, also in agreement with the numerical Floquet analysis. Under viscous flow conditions ($\alpha = 10^{-3}$), shown in figure 3-3(*b*,*d*), instability is confined to a finite range of κ. This is to be expected based on the near-inertial PSI theory: as κ is increased, the quadratic $\alpha\kappa^2$ will eventually exceed $\hat{\lambda}_r$, the inviscid growth rate, which is approximately constant at large κ.

Figure 3-4 plots the maximum instability growth rate, taken over κ, as a function of

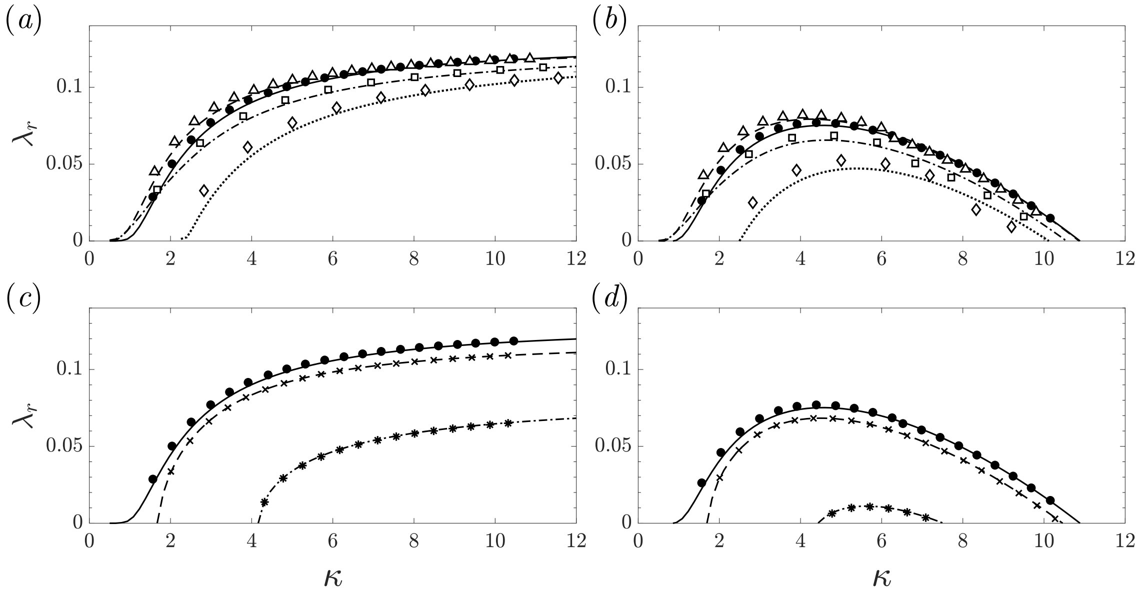

Figure 3-3: Comparison of predicted instability growth rates (in terms of the scaled time $T = \epsilon t$) as a function of the scaled perturbation wavenumber κ between the near-inertial PSI theory (using beam profile (3.33)) and the Floquet analysis (using beam profile (3.8) with beam amplitude $\epsilon = 0.002$) for primary beam frequency $\omega = 0.1$. Results are shown for viscous parameter (*a*,*c*) $\alpha = 0$ corresponding to inviscid flow, and (*b*,*d*) $\alpha = 10^{-3}$. (*a*,*b*) show results for detuning parameter $\hat{\sigma} = 0$ (●, solid line), $\hat{\sigma} = 4$ (△, dashed line), $\hat{\sigma} = 10$ (□, dashed-dotted line), and $\hat{\sigma} = 20$ (◇, dotted line). (*c*,*d*) show results for $\hat{\sigma} = 0$ (●, solid line), $\hat{\sigma} = -2$ (×, dashed line), $\hat{\sigma} = -4$ ($*$, dashed-dotted line). In all plots, shapes correspond to the Floquet growth rate while lines correspond to the near-inertial PSI growth rate.

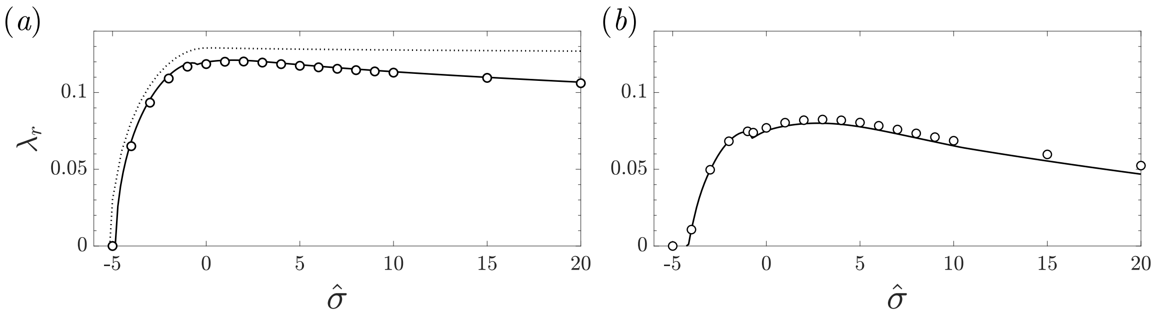

Figure 3-4: Maximum instability growth rate as function of detuning $-6 \leq \hat{\sigma} \leq 20$ for the same primary beam as in figure 3-3. (*a*) Inviscid flow conditions ($\alpha = 0$). In this case, since the maximum growth rate for a given $\hat{\sigma}$ occurs as $\kappa \to \infty$ (see figure 3-3*a*,*c*), results are presented for the near-inertial PSI growth rate at $\kappa = 12$ (solid line) and $\kappa = 100$ (dotted line). Floquet results ($\circ$) are shown at $\kappa \approx 12$. (*b*) Viscous flow conditions ($\alpha = 10^{-3}$). In this case, since the maximum growth rate is achieved at finite κ (see §3.5.2), plotted growth rates correspond to the maximum over all κ. Solid line is the near-inertial PSI growth rate, while ($\circ$) is the Floquet growth rate.

the detuning $-6 \leq \hat{\sigma} \leq 20$. Again, there is excellent agreement between the near-inertial PSI theory and the Floquet analysis. As illustrated in figure 3-4, instability is completely suppressed regardless of viscous dissipation when $\omega/2$ is sufficiently sub-inertial ($\hat{\sigma} \lesssim -5$). For inviscid flow conditions (figure 3-4*a*), the maximum instability growth rate, which is found as $\kappa \to \infty$ for a given detuning $\hat{\sigma}$, shows very weak dependence on $\hat{\sigma}$ for $\hat{\sigma} \geq 0$. Under viscous flow conditions ($\alpha = 10^{-3}$), shown in figure 3-4(*b*), the maximum growth rate decreases for large $\hat{\sigma}$, indicating that instability is weakened far enough from near-inertial conditions. Interestingly, though, for finite viscosity, instability is strongest at small but finite $\hat{\sigma} > 0$, rather than exactly at the critical $\omega = 2f$. This is due to the behaviour of the growth rates near the onset of instability: as illustrated in figure 3-3(*a*,*b*), the growth rates for $\hat{\sigma} = 4$ arise at slightly lower κ and have larger values in the range $1 \lesssim \kappa \lesssim 5$ than the growth rates for $\hat{\sigma} = 0$.

Finally, figure 3-5 compares the Floquet and PSI growth rates under inviscid flow conditions ($\alpha = 0$) at three different values of the detuning $\hat{\sigma} = -4, 0$, and 20 for the beam amplitudes $\epsilon = 0.002, 0.01, 0.05$, and 0.1. For $\hat{\sigma} = 0$, the Floquet growth rates for the larger $\epsilon = 0.2$ are also shown. As expected, the best agreement between the PSI theory and the Floquet analysis is found when the assumptions $\epsilon \ll 1$, $\epsilon k \ll 1$ ($\kappa \lesssim \epsilon^{-1/2}$) and $|\hat{\sigma}| = O(1)$ made in the PSI theory are well satisfied.

3.5.3 Instability dynamics

The results presented thus far indicate that the instability growth rates predicted by the numerical Floquet analysis agree well with the near-inertial PSI theory. However, as illustrated in figure 3-2 and discussed in §3.4.2, the main assumption of PSI theory, namely that

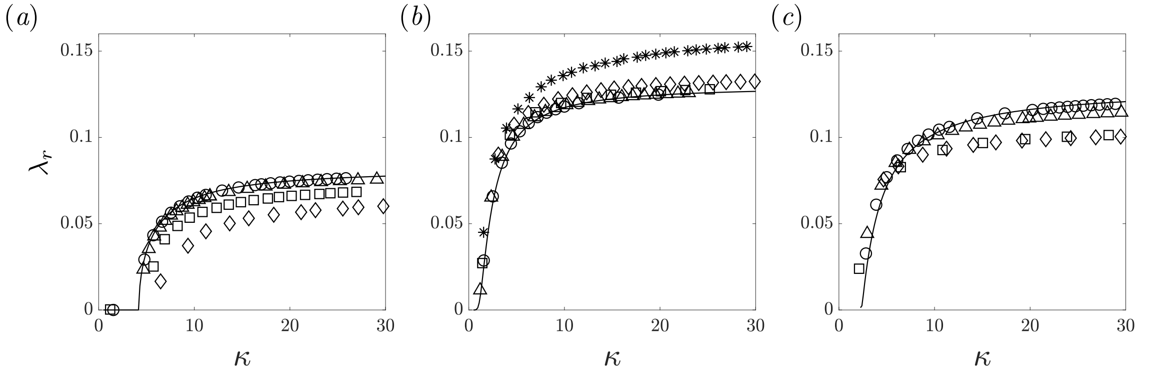

Figure 3-5: Inviscid instability growth rate as a function of the scaled perturbation wavenumber κ predicted by the Floquet analysis for beam amplitude $\epsilon = 0.002$ ($\circ$), 0.01 ($\triangle$), 0.05 ($\square$), 0.1 ($\diamond$). The same primary beam profile and frequency as in figure 3-3 and 3-4 are used here. Plots correspond to detuning parameter $\hat{\sigma} = -4$ (a), $\hat{\sigma} = 0$ (b), and $\hat{\sigma} = 20$ (c). The results for $\hat{\sigma} = 0$ in (b) include Floquet growth rates for $\epsilon = 0.2$ ($*$). Solid lines correspond to the near-inertial PSI growth rate.

the frequency components at $\pm\omega/2$ dominate, eventually breaks down as κ is increased with ϵ fixed. More precisely, the PSI theory fails when $\kappa = O(\epsilon^{-1/2})$, in keeping with (3.21) and (3.30), and unstable Floquet modes contain broadband frequency spectra.

To confirm these theoretical predictions, we return to the instability growth rate curve in figure 3-2(a). When plotted in terms of the scaled wavenumber magnitude κ rather than the along-beam wavenumber μ, this curve corresponds to the growth rate curve in figure 3-5(b) for $\hat{\sigma} = 0$ and $\epsilon = 0.01$ and is nearly indistinguishable from the predictions of the PSI theory. However, despite this agreement, the time-frequency spectra in figure 3-2(b–d), which correspond to $\kappa \approx 3, 10$ and 20, respectively, indicate that the instability dynamics for $\kappa \gtrsim 10$ does not resemble PSI at all, consistent with the estimate $\kappa \approx \epsilon^{-1/2} = 10$ for the breakdown of the PSI assumption. Furthermore, figure 3-6 compares the time-frequency spectra of the most unstable inviscid Floquet modes at $\kappa = 10$ for beam amplitudes $\epsilon = 0.002$ and 0.05 and detuning $\hat{\sigma} = -4, 0$, and 20. Since these Floquet modes exactly correspond to the growth rates shown in figure 3-5 at $\kappa = 10$, the Floquet growth rate is in excellent agreement with the PSI theory for both beam amplitudes. However, for the larger amplitude $\epsilon = 0.05$ (top row of figure 3-6), the frequency spectra indicate that the instability dynamics does not correspond to PSI, consistent with $\epsilon k \approx 2$ not being small.

In summary, when $\epsilon k \ll 1$ the near-inertial PSI theory is in excellent agreement with the numerical Floquet analysis. When ϵk is not small, instability is not dominated by the subharmonic frequencies at $\pm\omega/2$, consistent with the conclusion reached in §3.4.2. Remarkably however, PSI theory, even though it is not formally valid in this regime, still provides reliable predictions for the instability growth rate. We note that a similar observation was made by Sonmor & Klaassen (1997) for the instability of a sinusoidal wave (see their §4a).

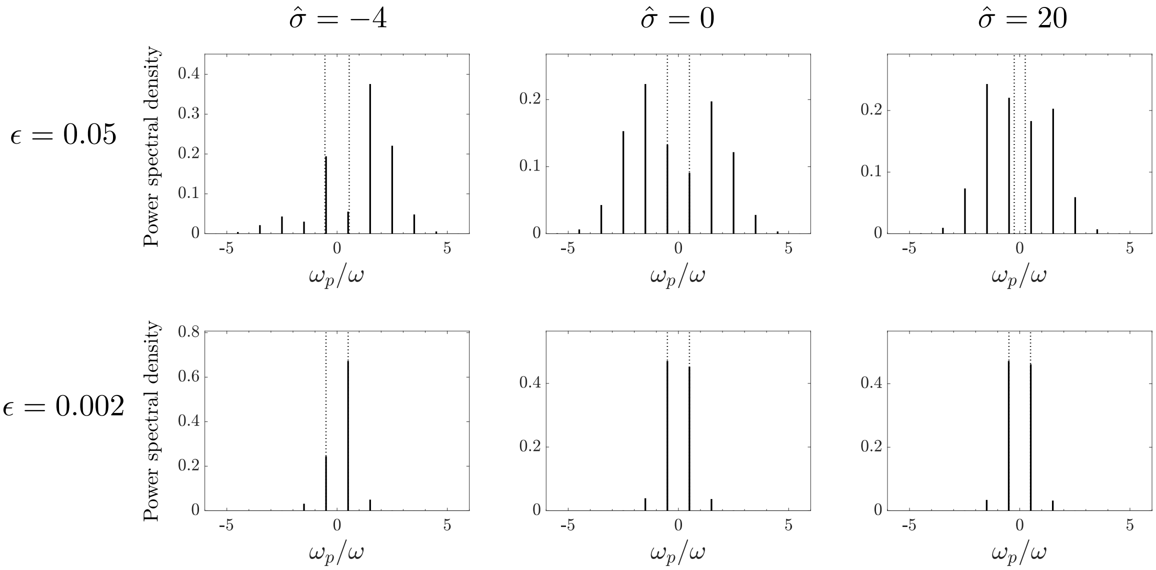

Figure 3-6: Time-frequency spectra of the fastest-growing Floquet mode found at scaled perturbation wavenumber $\kappa = 10$ for the same primary beam profile and frequency used throughout §3.5. Top row show modes for beam amplitude $\epsilon = 0.05$ while bottom row shows modes for $\epsilon = 0.002$. Left, middle and right columns correspond to detuning parameter $\hat{\sigma} = -4, 0$ and 20, respectively. The vertical dotted lines indicate the frequencies $\pm f/\omega$.

3.6 PSI of nearly monochromatic beams

3.6.1 Reduced eigenvalue problem

Aside from near-inertial conditions, PSI is also possible for small-amplitude locally confined beams with nearly monochromatic profile, as pointed out in KA14 for a beam with general frequency ω in the absence of background rotation ($f = 0$). This study omitted the contribution of the $\pm 3\omega/2$ frequency components to PSI dynamics. However, unlike near-inertial PSI, these frequencies do not affect the stability eigenvalue problem derived in KA14.

We wish to compare the predictions of PSI theory with those of Floquet stability analysis for a nearly-monochromatic beam under the conditions assumed in KA14. To this end, rather than quoting KA14, it is more economical to proceed directly from the small-amplitude limit of the Floquet stability problem discussed in §3.4. Specifically, we return to the eigenvalue problem (3.28) and consider a beam with frequency $\omega = \sin\theta$ ($f = 0$) and profile

$$Q(\eta) = q(H)\mathrm{e}^{\mathrm{i}\eta}, \qquad H = \hat{\epsilon}\eta. \tag{3.34}$$

Here, H is a stretched envelope coordinate and $\hat{\epsilon} \ll 1$ is a small parameter (made precise below) that controls the width of the slowly varying envelope $q(H)$ relative to the characteristic length scale $L_* = \Lambda_*/2\pi$, where Λ_* is the carrier wavelength of the primary wave beam. It should be noted that under the present conditions, the dispersion relation $\Omega = 0$

in (3.24) is exactly satisfied by choosing $\sin\phi = \omega/2$.

In view of (3.34), the perturbation amplitudes $\tilde{A}^{(0,1)}$ take the form

$$\tilde{A}^{(0)}(\eta) \to \tilde{A}^{(0)}(H)\mathrm{e}^{\mathrm{i}\frac{\eta}{2}}, \qquad \tilde{A}^{(1)}(\eta) \to \tilde{A}^{(1)}(H)\mathrm{e}^{-\mathrm{i}\frac{\eta}{2}}, \tag{3.35}$$

and inserting (3.34) and (3.35) into the stability equations (3.28), we find at leading order

$$\left(\lambda + \frac{1}{2}\nu k^2 + \mathrm{i}\frac{c}{2k} + \mathrm{i}\frac{3\omega}{8k^2}\right)\tilde{A}^{(0)} + \hat{\epsilon}\frac{c}{k}\tilde{A}^{(0)}_H - \epsilon\sin\chi\cos^2\left(\frac{\chi}{2}\right)q\tilde{A}^{(1)} = 0, \tag{3.36a}$$

$$\left(\lambda + \frac{1}{2}\nu k^2 + \mathrm{i}\frac{c}{2k} - \mathrm{i}\frac{3\omega}{8k^2}\right)\tilde{A}^{(1)} - \hat{\epsilon}\frac{c}{k}\tilde{A}^{(1)}_H - \epsilon\sin\chi\cos^2\left(\frac{\chi}{2}\right)q^*\tilde{A}^{(0)} = 0. \tag{3.36b}$$

The various terms in (3.36) may then be formally balanced in a similar fashion to the near-inertial PSI analysis (*c.f.* (3.30)), by the scalings

$$\lambda \to \epsilon\lambda, \quad \nu = 2\alpha\epsilon^2, \quad k = \frac{\kappa}{\epsilon^{1/2}}, \qquad \hat{\epsilon} = \frac{\epsilon^{1/2}}{D}. \tag{3.37}$$

Here,

$$D = 2\pi N\epsilon^{1/2} = O(1) \tag{3.38}$$

is a scaled width of the beam envelope in terms of N, the number of carrier wavelengths contained within the beam. Inserting (3.37) into (3.36) and making the substitutions $\tilde{A}^{(0,1)} \to \tilde{A}^{(0,1)}\exp[-3\mathrm{i}\omega H/(8c\kappa)]$ and $\lambda \to \lambda + \mathrm{i}c/(2k)$, which do not affect stability, we find that the PSI of nearly monochromatic beams is governed by

$$\hat{\lambda}\tilde{A}^{(0)} + \frac{c}{D\kappa}\tilde{A}^{(0)}_H - \sin\chi\cos^2\left(\frac{\chi}{2}\right)q\tilde{A}^{(1)} = 0, \tag{3.39a}$$

$$\hat{\lambda}\tilde{A}^{(1)} - \frac{c}{D\kappa}\tilde{A}^{(1)}_H - \sin\chi\cos^2\left(\frac{\chi}{2}\right)q^*\tilde{A}^{(0)} = 0, \tag{3.39b}$$

where

$$\hat{\lambda} = \lambda + \alpha\kappa^2. \tag{3.40}$$

As noted earlier, the final stability eigenvalue problem (3.39) is identical to that found by KA14 (see their equation 4.10), as the frequency components at ±3ω/2, omitted in KA14, ultimately do not play a role in the PSI stability analysis of nearly monochromatic beams.

3.6.2 Comparison with Floquet analysis

We now compare the results of the numerical Floquet analysis outlined in §3.2 against the predictions of the PSI theory (3.39). Specifically, we chose the Gaussian envelope profile

$$q(H) = \frac{1}{2}\exp\left(-8H^2\right), \tag{3.41}$$

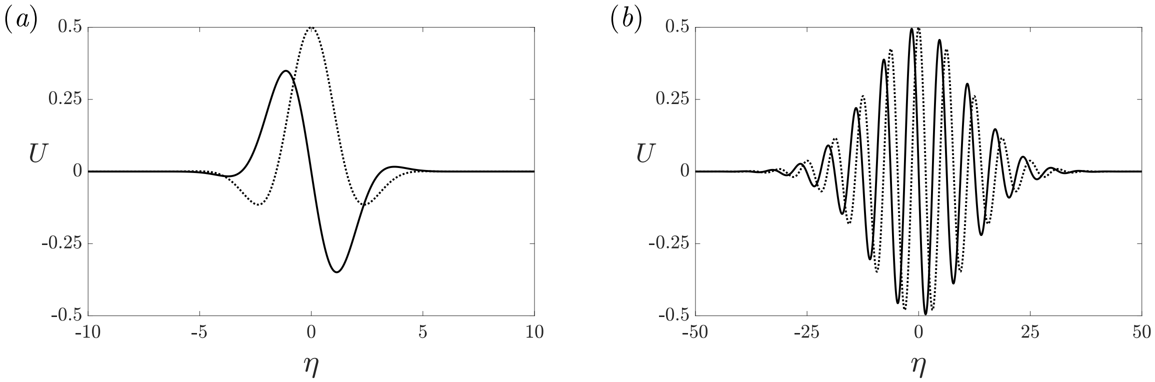

Figure 3-7: Beam profile (3.42) for nondimensional amplitude $\epsilon = 1$ and (*a*) $N = 1$ and (*b*) $N = 7$, where N corresponds to the number of carrier wavelengths contained within the beam width. Solid lines indicate the real part, while dotted lines indicate the imaginary part.

whose width is approximately 4 standard deviations. Combined with (3.34) and (3.37), (3.41) corresponds to the overall beam profile

$$U(\eta) = \mathrm{i}\frac{\epsilon}{2} \exp\left[-\frac{1}{2}\left(\frac{4}{2\pi N}\right)^2 \eta^2\right] \exp(\mathrm{i}\eta) \tag{3.42}$$

to be used in the numerical Floquet analysis (see (3.2)). Figure 3-7 plots the beam profile (3.42) for $\epsilon = 1$ and $N = 1$ and 7. We recall that, according to (3.38), $N = O(\epsilon^{-1/2})$ in the PSI theory. Numerically, the eigenvalue problem (3.39) was discretized in the domain $H \in [-5, 5]$ using 8th-order centred differences with a grid size of 500 points, and the resulting matrix eigenvalue problem was solved using standard numerical eigenvalue algorithms in MATLAB for the eigenvalue $\hat{\lambda}$. The discussion below will focus on the beam inclination angle $\theta = 45°$ (which is tied to the beam frequency via the dispersion relation $\omega = \sin\theta$) and viscosity $\nu = 10^{-5}$. The effect of varying θ is discussed in §3.6.3.

Figure 3-8(*a*) plots the maximum instability growth rates (taken over κ and given in terms of the slow time $T = \epsilon t$) predicted by the PSI theory and the numerical Floquet analysis as a function of N, the number of carrier wavelengths of the beam profile, for various values of $0.025 \leq \epsilon \leq 0.4$. As expected, in the limit of $N \to \infty$, the PSI growth rates converge onto the sinusoidal wave growth rate. Furthermore, the Floquet growth rates show excellent agreement with the PSI theory for all $\epsilon \leq 0.4$ and $N \geq 2$, even though in these parameter ranges neither the assumption of small amplitude (i.e. $\epsilon \ll 1$) nor the assumption of scale separation between the carrier and the envelope (i.e. $N \gg 1$) are necessarily well satisfied.

Furthermore, based on PSI theory, KA14 proposed a lower bound on N, the number of carrier wavelengths contained in the beam envelope, needed for PSI (see their equation (5.14)). By re-arranging their expression for this lower bound, which depends on various parameters including the viscosity ν and beam amplitude ϵ, we find that a minimum amplitude threshold needed for instability at fixed N is

$$\epsilon_c = \left(\frac{1}{2\mathbb{C}_c}\right)^{1/3} \frac{c^{2/3}}{\Gamma} \frac{\nu^{1/3}}{(2\pi N)^{2/3}}. \tag{3.43}$$

Here, $\mathbb{C}_c \approx 3.35 \times 10^{-3}$ is a coefficient set by the choice of envelope profile (3.41), c is defined in (3.25c), and $\Gamma = \sin\chi\cos^2(\chi/2)$. Figure 3-8($b$) compares (3.43) against the minimum amplitude threshold found numerically using the Floquet analysis for various $2 \leq N \leq 10$ and for three different viscosities $\nu = 5 \times 10^{-4}, 10^{-3}$, and 2×10^{-3}. We observe excellent agreement between (3.43) and the numerical results.

Figure 3-9 plots the time-frequency spectra of the Floquet modes corresponding to the growth rates shown in figure 3-8(a) for $\epsilon = 0.05$ and 0.2, and for $N = 2$, 10, and 20. Similar to the results found in §3.5.3 for near-inertial conditions, the frequency spectra widen as the beam amplitude ϵ is increased, corresponding to the emergence of multiple instability frequencies other than $\pm\omega/2$. Again, we find that PSI theory, although it is no longer strictly valid, still provides accurate predictions of the instability growth rates.

Finally, it is worth noting that (3.43) predicts that $\epsilon_c \to 0$ in the inviscid limit ($\nu = 0$) regardless of N. This is in qualitative agreement with the discussion of §3.4.2, which suggests that small-amplitude ($\epsilon \ll 1$) locally confined beams with general (not necessarily nearly monochromatic) profile are possibly susceptible to instability. However, this instability may arise when $\epsilon k = O(1)$ and is distinct from PSI. We shall return to this point in §3.7.

3.6.3 Instability for inclination angle $\theta \lesssim 43°$

Thus far, the results of §3.6 have focused on the beam inclination angle $\theta = 45°$. However, as noted in §3.2.2, for a plane sinusoidal wave in the absence of rotation ($f = 0$) and under inviscid flow conditions, PSI is the most unstable of all triadic resonant instabilities only for wave inclination angle $\theta \gtrsim 43°$. For $\theta \lesssim 43°$, the 'branch-C' or finite-scale TRI, where one member of the triad has larger wavelength than the primary wave, has higher growth rate than PSI. To check whether this interesting result also holds for a locally confined beam, we now consider the stability of a nearly monochromatic beam with frequency $\omega = 0.4$, corresponding to $\theta \approx 23.6°$. Here, we will use the term PSI to refer to any TRI where both members of the resonant triad have smaller wavelength than the primary wave.

Figure 3-10 compares the dominant instability growth rates, computed using the Floquet stability analysis and scaled by the beam amplitude $\epsilon = 0.1$, between a nearly monochromatic beam with the profile (3.42) for $N = 20$ and a purely sinusoidal wave (i.e. $N \to \infty$) under inviscid flow conditions. Here, growth rates are plotted as a function of the along-beam perturbation wavenumber μ. In the case of the sinusoidal wave, the growth rate curve features a distinct kink at $\mu \approx 0.62$, where the instability with the highest growth rate transitions from a branch-C-like instability at low μ to a PSI-like instability at high μ. It

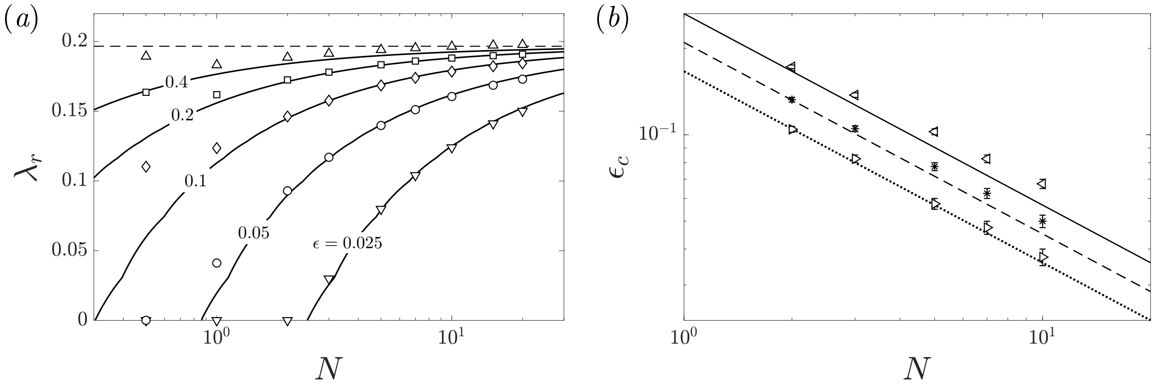

Figure 3-8: (a) Computed instability growth rates (in terms of the scaled time $T = \epsilon t$) according to the Floquet stability analysis as a function of N, the number of carrier wavelengths contained in the beam width, for the profile (3.42) with viscosity $\nu = 10^{-5}$, beam frequency $\omega = \sin 45°$, and beam amplitudes $\epsilon = 0.025$ ($\triangledown$), 0.05 ($\circ$), 0.1 ($\Diamond$), 0.2 ($\Box$), and 0.4 ($\triangle$). The corresponding asymptotic PSI growth rates, as predicted by (3.39), are overlaid and labelled. The PSI growth rate for a sinusoidal wave (i.e. $N \to \infty$) is indicated by the horizontal dashed line. (b) Minimum amplitude ϵ_c for instability as a function of N for $\nu = 5 \times 10^{-4}$ ($\triangleright$, solid line), 10^{-3} ($*$, dashed line), and 2×10^{-3} ($\triangleleft$, dotted line). Shapes correspond to Floquet analysis results while lines correspond to the amplitude threshold (3.43) predicted by the PSI theory.

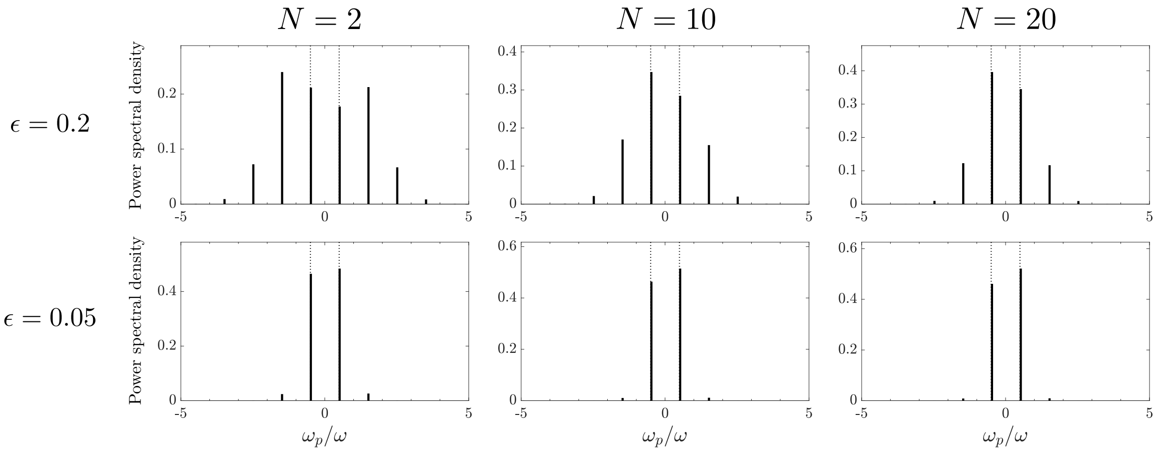

Figure 3-9: Time-frequency spectra of the fastest-growing Floquet mode for various configurations shown in figure 3-8(a). Top and bottom rows correspond to beam amplitude $\epsilon = 0.2$ and 0.05, respectively. Left, middle and right columns correspond to $N = 2$, 10 and 20. Vertical dotted lines in each plot correspond to the frequencies $\pm\omega/2$.

should be noted that at the inclination angle $\theta \approx 23.6°$, the maximum branch-C growth rate is larger than that of PSI by nearly 40%. By contrast, for the nearly monochromatic beam with $N = 20$ wavelengths at the same θ, the Floquet analysis growth rates simply increase monotonically and converge to the PSI growth rate as $\mu \to \infty$, with no sign of the 'branch-C' instability. This reveals that the finite width of the beam stabilizes the branch-C instability to a far greater extent than PSI (which involves smaller-scale perturbations), likely due to the fact that perturbations with $O(1)$ wavenumber have $O(1)$ group velocity and therefore propagate quickly across the primary beam.

Furthermore, this stabilizing effect suggests an explanation for why Bourget *et al.* (2013), in their experimental study of TRI in a finite-width beam with approximately three carrier wavelengths, did not observe the branch-C instability and instead observed PSI. In these experiments, although the inclination angle $\theta \approx 47.7° > 43°$, due to the effect of viscosity and the proximity to the critical angle of 43°, the branch-C instability of a sinusoidal wave has higher growth rate than PSI (see their figure 7). However, based on our findings here, it is likely that the finite width of the experimentally-generated beam suppressed the branch-C instability, allowing PSI to manifest.

3.7 Broadband instability of small-amplitude beams

In §3.4.2 it was argued that PSI is not an effective instability mechanism of small-amplitude ($\epsilon \ll 1$) beams with general locally confined profile away from near-inertial conditions because the group velocity effect overwhelms the coupling of the perturbations with the primary beam (see (3.28)). However, the full stability eigenvalue problem (3.19) suggests that such beams may still be unstable to fine-scale ($k \gg 1$) perturbations when $\epsilon k = O(1)$, but unlike PSI this potential instability involves broadband frequency spectrum. To explore this possibility, we consider again the beam with profile (3.8) and frequency $\omega = 0.1$, used in the discussion of near-inertial PSI of §3.5 (see figure 3-1*b*), except here, we assume no background rotation ($f = 0$).

Figure 3-11(*a*) plots the instability growth rates (scaled with the beam amplitude ϵ) found by the numerical Floquet analysis as a function of the perturbation wavenumber k, for $\epsilon = 0.01$ under inviscid flow conditions ($\nu = 0$). For comparison, the same figure also plots the growth rates for $f = 0.05$, corresponding to near-inertial conditions exactly at the critical frequency $\omega = 2f$. Figure 3-11(*a*) confirms that for $f = 0$, the beam is unstable when $\epsilon k \gtrsim O(1)$. The onset of instability occurs at $k \approx 45$ ($\epsilon k \approx 0.45$) and the growth rate keeps increasing monotonically, reaching a plateau for $k \gtrsim 300$ ($\epsilon k \gtrsim 3$). This is in sharp contrast to the instability for $f = 0.05$ (i.e. near-inertial conditions), which arises at a significantly lower value of $k \approx 10$ ($\epsilon k = 0.1$), consistent with the scaling $\kappa = \epsilon^{1/2} k = 1 = O(1)$ of near-inertial PSI, and has reached its plateau when $k \gtrsim 100$ ($\epsilon k \gtrsim 1$).

Figure 3-11(*b*–*d*) plots the frequency spectrum of the Floquet mode for $f = 0$ at $k =$

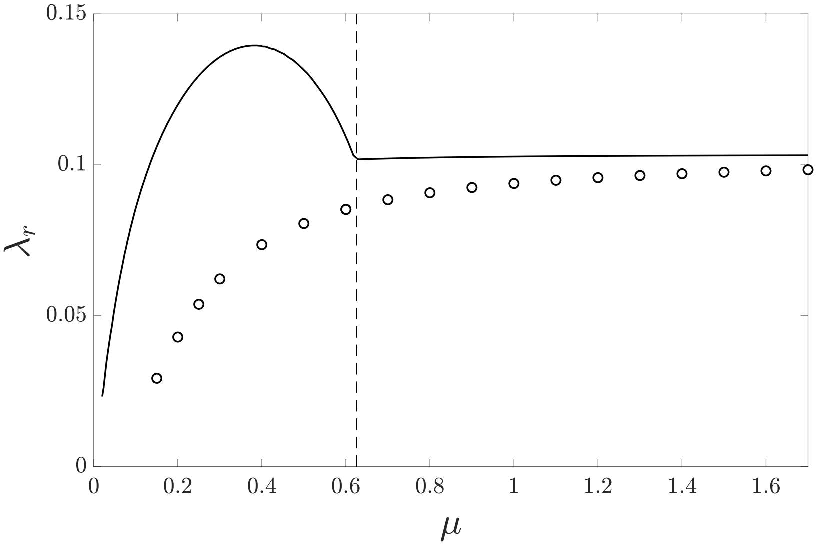

Figure 3-10: Instability growth rate predicted by the Floquet stability analysis ($\circ$) as a function of the along-beam (ξ-) wavenumber μ of the perturbation, for the beam profile (3.42) with beam frequency $\omega = 0.4$ (i.e. beam inclination angle $\theta \approx 23.6°$), amplitude $\epsilon = 0.1$, viscosity $\nu = 0$, and $N = 20$ wavelengths of the carrier contained in the beam width. The corresponding growth rates for a sinusoidal wave as predicted by Floquet analysis under the same conditions are plotted as the solid line. The vertical dashed line at $\mu \approx 0.62$ indicates the point at which the most unstable perturbations to the sinusoidal wave transitions between the 'branch-C'-like instability (for $\mu \lesssim 0.62$), where one subharmonic frequency component of the perturbation has larger wavelength than the primary wave, and the PSI-like instability (for $\mu \gtrsim 0.62$), where both subharmonic frequency components have smaller wavelength than the primary wave.

$80, 200$ and 400. Perhaps surprisingly, at $k = 80$ ($\epsilon k = 0.8$) the frequency components $\pm\omega/2$ are dominant so the spectrum is of the PSI type (figure 3-11*b*). However, as shown in figure 3-11(*a*), the instability growth rate at this value of k is significantly lower than its near-inertial counterpart, consistent with the destabilising effect of the vanishing group velocity at the critical frequency $\omega = 2f$. Furthermore, the Floquet modes associated with the highest growth rates for $f = 0$ (which are roughly 75% of the highest near-inertial growth rates) are certainly broadband, as illustrated in figure 3-11(*c*,*d*) at $k = 200$ and 400, corresponding to $\epsilon k = 2$ and 4. Thus, the scaling argument made in §3.4.2 (and KA14) for ruling out PSI of small-amplitude locally confined beams away from near-inertial conditions is not entirely binding: the dominant instability for $f = 0$ indeed is broadband, but PSI is still relevant near the onset of instability.

The computed instability for $f = 0$ is expected to be more vulnerable to the effects of viscous dissipation, owing to the larger wavenumber perturbations required, $k = O(\epsilon^{-1})$, than near-inertial PSI, which arises when $k = O(\epsilon^{-1/2})$. This is illustrated in figure 3-12, which shows the effect of finite viscosity ($\alpha = 10^{-3}$) on the Floquet growth rates for the same beam as in figure 3-11(*a*). In this case, for both $f = 0$ and $f = 0.05$ (i.e. near-inertial conditions), instability is entirely stabilized when $k \gtrsim 110$ ($\epsilon k \gtrsim 1.1$), thereby eliminating the broadband-type instability and leaving only the PSI-type instability. As a result, instability is far weaker for $f = 0$ than for $f = 0.05$. Based on figure 3-12, for $\alpha = 10^{-3}$, the maximum growth rate for $f = 0$ decreases by roughly 80% relative to inviscid conditions, whereas the maximum growth rate for $f = 0.05$ decreases only by roughly 30%.

3.8 Concluding remarks

We made an analytical and numerical study of instability mechanisms of finite-width internal gravity wave beams using a formal stability analysis based on Floquet theory. Our original motivation was to assess the validity of the approximate theories proposed in KA14 and KA17 for the PSI of small-amplitude beams. These models assume that PSI involves a resonant triad interaction between a beam of frequency ω and two fine-scale subharmonic perturbation wavepackets with carrier frequency $\omega/2$. This hypothesis is supported by our asymptotic analysis of the Floquet stability eigenvalue problem in the PSI regime, namely a small-amplitude beam subject to fine-scale perturbations in the nearly inviscid limit. However, the Floquet instability mode also comprises components with frequency $3\omega/2$, ignored in KA14 and KA17, which are smaller than the subharmonic wavepackets but still play an important part, particularly in near-inertial PSI where they affect the instability growth rate. The participation of these additional frequency components in PSI dynamics is a higher-order interaction (resonant quartet) effect that here comes into play at the same level as the main resonant triad owing to the fine scale (large wavenumber) of the perturbations.

After accounting for the $3\omega/2$ frequency components, the predictions of KA17 for near-

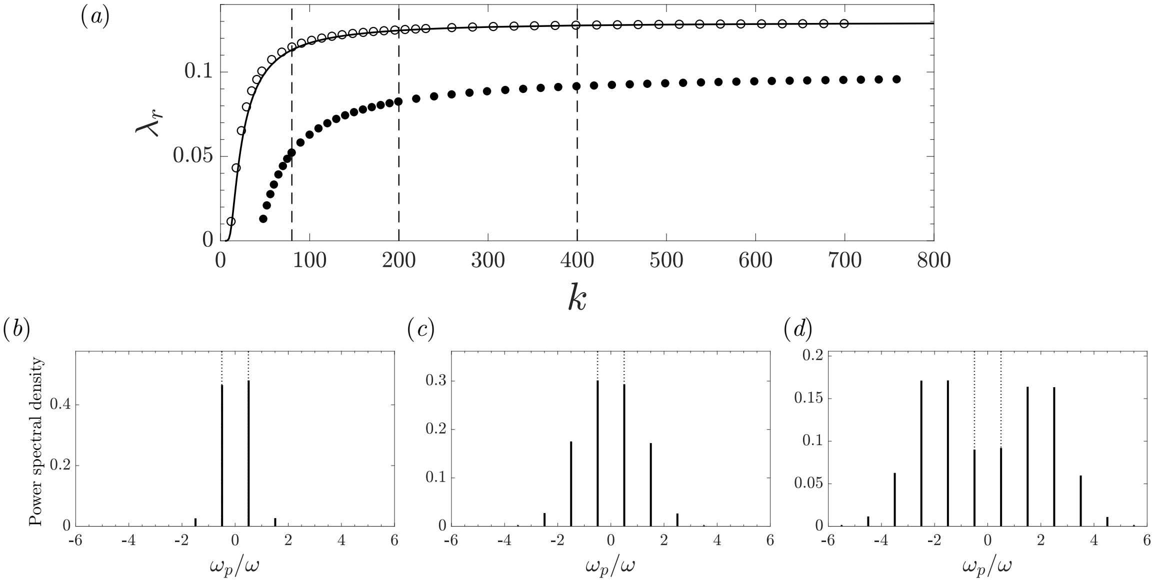

Figure 3-11: (*a*) Floquet growth rate (●) as a function of the perturbation wavenumber magnitude k using beam profile (3.8) for beam amplitude $\epsilon = 0.01$, primary beam frequency $\omega = 0.1$ and no background rotation ($f = 0$) under inviscid flow conditions ($\nu = 0$). The Floquet growth rate for $f = 0.05$ (○) and the asymptotic near-inertial PSI growth rate (solid line) are plotted for comparison. Vertical dashed lines indicate the values $k = 80, 200$ and 400. (*b*) Time-frequency spectra of the most unstable Floquet mode for $f = 0$ shown in (*a*) at $k = 80$. Vertical dashed lines indicate the frequencies $\omega_p = \pm\omega/2$. (*c*) Same as (*b*) but at $k = 200$. (*d*) Same as (*b*) but at $k = 400$.

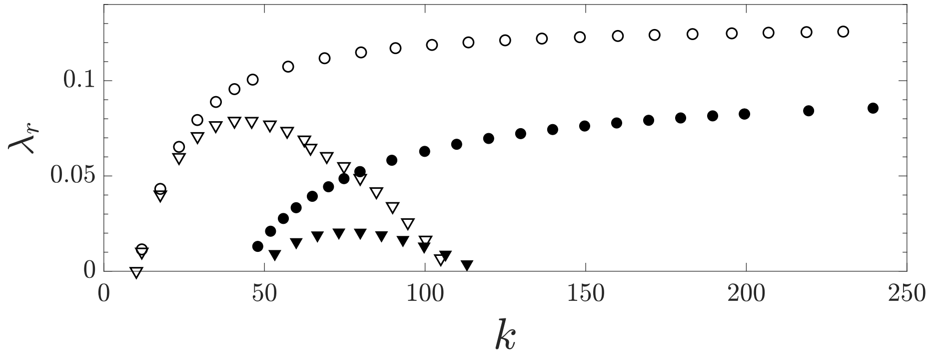

Figure 3-12: Effect of viscosity on the Floquet growth rates shown in figure 3-11(*a*) using the same beam profile (3.8), beam amplitude $\epsilon = 0.01$ and primary beam frequency $\omega = 0.1$, for $\alpha = 10^{-3}$ (▲, △) and $\alpha = 0$ (●, ○). Filled shapes (●, ▲) correspond to growth rates for $f = 0$, while open shapes (○, △) correspond to results for $f = 0.05$ (i.e. near-inertial conditions).

inertial PSI of a locally confined beam are in excellent quantitative agreement with those of the Floquet stability analysis, even outside the formal range of validity of the approximate model. Close agreement is also found between the model of KA14 and the exact linear stability analysis away from near-inertial conditions. In this instance, the $3\omega/2$ frequency components of the Floquet instability mode omitted in KA14 do not affect the instability growth rate. The asymptotic PSI theory of KA14 also assumes nearly monochromatic beam profile – the resonant interaction of the subharmonic perturbations, which travel with their group velocity, with the underlying beam must be finely tuned to cause instability. Nevertheless, we find satisfactory agreement of the asymptotic PSI growth rate with that computed from the Floquet stability analysis, even for a beam profile with as few as two carrier wavelengths. Furthermore, the validity of the asymptotic beam-amplitude threshold for PSI found in KA14 is confirmed.

An interesting insight revealed by our analysis of the small-amplitude limit of the Floquet stability problem is that the coupling of the perturbation with the underlying beam is controlled by ϵk, where $\epsilon \ll 1$ measures the beam amplitude and $k \gg 1$ is the perturbation wavenumber. As a result, PSI arises only when $\epsilon k \ll 1$ so the coupling is weak and the two subharmonic perturbation components with frequency $\omega/2$ dominate. This also explains why the frequency spectrum of the Floquet instability mode eventually becomes broadband as ϵ is increased (in agreement with the results of Onuki & Tanaka, 2019) and/or k is increased. Furthermore, this broadband instability can persist in the nearly inviscid limit for small-amplitude beams with general (not nearly monochromatic) locally confined profile, which according to the scaling argument presented in §3.4.2 (and KA14) are not susceptible to PSI.

THIS PAGE INTENTIONALLY LEFT BLANK

Chapter 4

Effect of background mean flow on the PSI of nearly monochromatic internal wave beams

Much of this text previously appeared in Fan, B. & Akylas, T. R. 2019 Effect of background mean flow on PSI of internal wave beams. *J. Fluid Mech.* **869**, R1. However, it has been corrected and updated to reflect new findings based on the results of Chapter 3.

4.1 Introduction

Among the various types of instabilities that are known to befall internal gravity waves in continuously stratified fluids (Sonmor & Klaassen, 1997; Dauxois *et al.*, 2018, and references therein), parametric subharmonic instability (PSI) has been widely studied in the past decades. In its most idealized form, PSI involves transfer of energy from a primary sinusoidal wavetrain to two subharmonic perturbations via a weakly nonlinear resonant triad interaction (Staquet & Sommeria, 2002). Furthermore, for nearly inviscid flows, the most unstable perturbations have short wavelength relative to the primary wave, and frequency equal to half that of the primary wave. In view of this transfer of energy into smaller scales, PSI emerges as a possibly significant factor in the dissipation of oceanic internal waves and could provide a pathway for their contribution to mixing (e.g. Hibiya *et al.*, 2002; MacKinnon & Winters, 2005; Young *et al.*, 2008).

Oceanic observations of PSI (Alford *et al.*, 2007; MacKinnon *et al.*, 2013) and detailed numerical simulations (Hazewinkel & Winters, 2011) though have found only modest energy transfer rates compared with the idealized theory. To account for this discrepancy, it is possible that the presence of mesoscale flow features, such as background mean flows, may alter the dynamics of PSI. For instance, recent numerical experiments (Richet *et al.*, 2017) indicate that near-inertial PSI around the critical latitude is weakened by a background mean flow. To support these findings, Richet *et al.* (2017) argue that, due to the Doppler shift of the frequency of a sinusoidal plane wave by the background mean flow, the primary wave frequency can fall below $2f$ (where f is the inertial frequency); in such a case, the subharmonic perturbations with half the primary frequency would be sub-inertial and hence forbidden by the dispersion relation, preventing PSI.

Recent work on PSI has also shifted attention from sinusoidal plane waves to plane waves with locally confined spatial profile (Clark & Sutherland, 2010; Bourget *et al.*, 2013, 2014; Karimi & Akylas, 2014, 2017). Such wave beams provide a more realistic setting for PSI (Sutherland, 2013), as they arise from the interaction of the barotropic tide with bottom topography in oceans (e.g. Lamb, 2004; Peacock *et al.*, 2008; Johnston *et al.*, 2011) and can also be generated by thunderstorms in the atmosphere (e.g. Fovell *et al.*, 1992). The finite width of an internal wave beam imposes additional constraints on PSI because subharmonic perturbations, which propagate across the beam with their group velocity, will eventually leave the beam (Bourget *et al.*, 2014; Karimi & Akylas, 2014, 2017). As a result, PSI is only possible if a beam: (*i*) has nearly monochromatic profile so as to allow fine-tuned triad interactions similar to a sinusoidal plane wave; and (*ii*) is sufficiently wide so that subharmonic perturbations can stay in contact with the beam for long enough time (Karimi & Akylas, 2014). These conditions also hold in the presence of background rotation, unless the primary beam frequency happens to be close to $2f$, in which case it is possible for beams of general profile to be subject to PSI. In this instance, subharmonic perturbations with half the primary frequency are near-inertial and have nearly vanishing group velocity, which prolongs their contact with the primary beam and thus enhances PSI (Karimi & Akylas, 2017).

The present paper seeks to further advance our understanding of PSI in more realistic scenarios. Specifically, we explore the effect of a constant uniform background mean flow on PSI of finite-width internal wave beams in the absence of background rotation. These flow conditions preclude near-inertial PSI and, in view of the findings of Karimi & Akylas (2014), attention is focused on nearly monochromatic beams. We first discuss how the mean flow affects the beam profile itself and then derive evolution equations for fine-scale subharmonic perturbations. The analysis considers a 'distinguished limit' where coupling with the underlying beam, dispersion, viscous dissipation and the background mean flow partake in the perturbation dynamics on an equal footing; to this end, it will be necessary to assume that the mean flow is small. The main effect of the background mean flow is to advect the subharmonic perturbations, which modifies their group velocity and generally hinders their capacity to extract energy from a finite-width beam. Specifically, for PSI to arise in the presence of the mean flow, unstable perturbations must propagate in opposite directions across the beam. This constraint stabilizes very short-scale perturbations and can in fact weaken PSI dramatically, as demonstrated by calculating the growth rates and range of unstable wavenumbers for a nearly monochromatic beam profile with a 'top-hat' envelope. These findings for a finite-width beam are in stark contrast with the case of a purely sinusoidal plane wave, where the presence of a uniform background mean flow has no effect on PSI once the Doppler shift of the wave frequencies has been taken into account.

4.2 Formulation

4.2.1 Preliminaries

Our analysis assumes two-dimensional disturbances in an unbounded, incompressible, uniformly stratified Boussinesq fluid with constant buoyancy frequency N_*, and will use nondimensional variables with $1/N_*$ as the time scale and L_* as the length scale, to be specified later. We take x to be the horizontal coordinate, y the vertical coordinate pointing antiparallel to gravity, and $\overline{\boldsymbol{u}} = \overline{u}\,\hat{\boldsymbol{e}}_x$ the horizontal uniform background mean flow with respect to a fixed reference frame. In this frame, the streamfunction ψ for the velocity field $(\psi_y, -\psi_x)$, and the reduced density ρ are governed by

$$(\partial_t + \overline{u}\,\partial_x)\rho + \psi_x + J(\rho, \psi) = 0, \tag{4.1a}$$

$$(\partial_t + \overline{u}\,\partial_x)\nabla^2\psi - \rho_x + J(\nabla^2\psi, \psi) - \nu\nabla^4\psi = 0. \tag{4.1b}$$

Here, $J(a, b) = a_x b_y - a_y b_x$ stands for the Jacobian and $\nu = \nu_*/N_* L_*^2$ is an inverse Reynolds number where ν_* is the fluid kinematic viscosity.

In the linear, inviscid limit ($\nu = 0$), equations (4.1) admit sinusoidal plane wave solutions that obey the dispersion relation

$$(\omega - \overline{u}\,|\boldsymbol{k}|\sin\theta)^2 = \sin^2\theta, \tag{4.2}$$

where ω is the wave frequency, $|\boldsymbol{k}|$ is the magnitude of the wavevector $\boldsymbol{k}$ and θ is the inclination of $\boldsymbol{k}$ to the vertical (figure 4-1*a*). It is useful to note that in (4.2), the quantity in parentheses is the (Doppler shifted) frequency of the wave in the reference frame moving with the background mean flow. In the case of $\overline{u} = 0$, (4.2) reduces to the well-known internal wave dispersion relation, where the inclination of the wavevector to the vertical alone determines the frequency. For a locally confined time-harmonic source, it is then possible to construct infinitely long uniform wave beam solutions by superposing sinusoidal plane waves with the same frequency as the source but general $|\boldsymbol{k}|$ spectrum, and these solutions are also exact nonlinear states (Tabaei & Akylas, 2003). In contrast, for $\overline{u} \neq 0$, the wave frequency is no longer independent of $|\boldsymbol{k}|$ and exact uniform beam solutions are not possible. In this case, each wavevector $\boldsymbol{k}$ generated by a general, locally confined source with fixed frequency will be affected by the mean flow to a varying degree, resulting in a two-dimensional wake-like wave pattern far away from the forcing (Lighthill, 1978, §4.12).

4.2.2 Primary wave beam

Our interest here is on flow conditions that permit the generation of beams for $\overline{u} \neq 0$, that will be used later in the PSI analysis. To this end, keeping also in mind that beams with nearly monochromatic spatial profiles are the only ones that can suffer from PSI in the absence of background rotation (Karimi & Akylas, 2014), we shall focus on waves generated by a time-harmonic source whose spatial profile consists of a sinusoidal carrier modulated by a locally confined envelope. The steady-state response to such a source is expected to also be time-harmonic and have nearly monochromatic spatial dependence. Accordingly, without getting into the detailed generation process, we take as characteristic length scale $L_* = \Lambda_*/2\pi$, where Λ_* is the dimensional carrier wavelength of the generated wave disturbance. The carrier wavevector $\boldsymbol{k}_0$ is then simply given by

$$\boldsymbol{k}_0 = \hat{\boldsymbol{e}}_\eta, \tag{4.3}$$

where $\hat{\boldsymbol{e}}_\eta$ is a unit vector pointing along $\eta = x \sin\theta + y\cos\theta$, and in view of (4.2), θ is related to the source frequency ω_0 by

$$\omega_0 = (1 + \overline{u})\sin\theta. \tag{4.4}$$

Furthermore, owing to the modulations of the source profile, the wave response involves sidebands, $\boldsymbol{k} = \boldsymbol{k}_0 + \mu\boldsymbol{q}$ $(0 < \mu \ll 1)$ that modulate the sinusoidal carrier $\boldsymbol{k}_0$ with a slowly varying envelope. For $\overline{u} \neq 0$, it is clear from (4.2) that each of these sidebands will point in a slightly different direction than $\boldsymbol{k}_0$. Expanding (4.2) about $\boldsymbol{k}_0$ gives $\omega_0 - \overline{u}(\boldsymbol{k}_0 + \mu\boldsymbol{q}) \cdot \hat{\boldsymbol{e}}_x = \sin\theta + \mu\boldsymbol{c}_g \cdot \boldsymbol{q}$ to leading order in μ, and taking into account (4.4), we find that $\boldsymbol{c}_g \cdot \boldsymbol{q} + \overline{u}\,\boldsymbol{q} \cdot \hat{\boldsymbol{e}}_x = 0$, where the group velocity $\boldsymbol{c}_g$ of $\boldsymbol{k}_0$ is taken in the fluid frame. Thus, the slowly varying envelope of the wave response can be described by the stretched coordinate H which is inclined to the vertical by the angle Θ such that

$$H = \mu(x\sin\Theta + y\cos\Theta), \quad \tan\Theta = \frac{-c_{g,y}}{c_{g,x} + \overline{u}} = \frac{\sin\theta}{\cos\theta + \overline{u}/\cos\theta}, \tag{4.5}$$

where μ^{-1} sets the envelope length scale, and $c_{g,x}$ and $c_{g,y}$ are the horizontal and vertical components of $\boldsymbol{c}_g$. It should be noted that the mean flow rotates the modulation direction $\hat{\mathbf{e}}_H$ relative to the carrier direction $\hat{\boldsymbol{e}}_\eta$ (figure 4-1*a*), an effect that depends on the sign of $\overline{u}$ and the orientation of $\boldsymbol{k}_0$.

From the above kinematic analysis, it is concluded that the response to the assumed wave source in a background mean flow is a nearly monochromatic beam in the form

$$\psi_0 = \rho_0 = \epsilon\Big\{Q(H)\mathrm{e}^{\mathrm{i}(\eta - \omega_0 t)} + \text{c.c.}\Big\} + \ldots, \tag{4.6}$$

where the envelope $Q(H)$ is related to the source spatial profile, and the amplitude parameter $\epsilon = U_*/(N_* L_*) \ll 1$, U_* being the dimensional peak beam velocity. It should be noted that

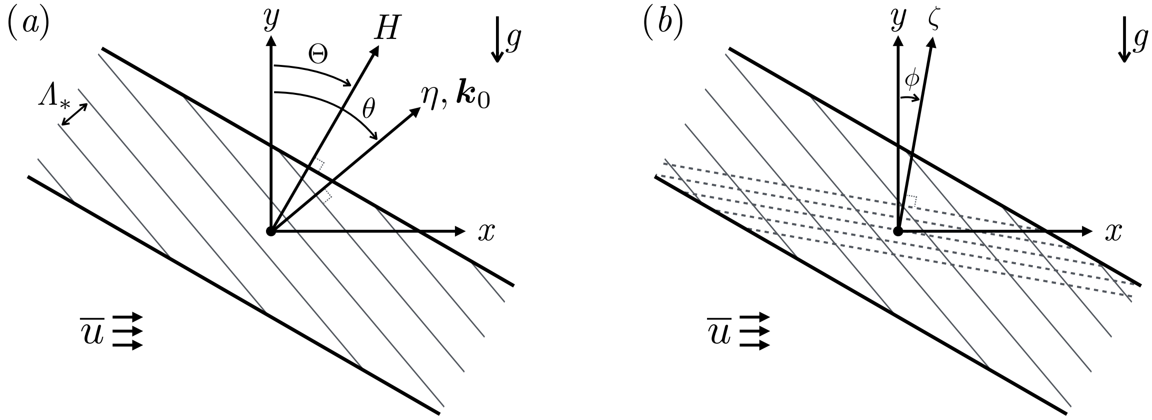

Figure 4-1: Schematic of the PSI geometry. (a) Nearly monochromatic primary wave beam of frequency ω_0 in the presence of a background mean flow $\overline{u}$. The carrier wavevector $\boldsymbol{k}_0 = \hat{\boldsymbol{e}}_\eta$ is inclined to the vertical by θ, determined by the Doppler shifted dispersion relation (4.4). Thin solid lines indicate lines of constant phase (e.g. crests) of the carrier with Λ_* as the dimensional carrier wavelength, while thick solid lines indicate the finite extent of the envelope. According to (4.5), due to the mean flow, the modulation coordinate H is inclined to the vertical by an angle Θ different from θ. (b) Subharmonic perturbations are short-scale wavepackets with lines of constant phase (dashed lines) inclined to the horizontal by the angle ϕ given by (4.12).

unlike uniform beams in the absence of mean flows, which are exact inviscid nonlinear states, (4.6) is only an approximate weakly nonlinear solution of equations (4.1). Specifically, due to the dispersive effects of the mean flow, the beam envelope will also feature variations in the direction orthogonal to $\hat{\boldsymbol{e}}_H$. Such 'along-beam' modulations, however, have an $O(\mu^{-2})$ length scale as can be verified from expanding (4.2) about $\boldsymbol{k}_0$ correct to $O(\mu^2)$, and will be neglected in the PSI stability analysis in comparison with the 'cross-beam' $O(\mu^{-1})$ modulations in H. Furthermore, weakly nonlinear effects on the beam solution (4.6) itself, owing to self-interactions with its mean and higher harmonics, will not be considered either because they act over an $O(\mu^{-1}\epsilon^{-2})$ time scale at best (see §A.2) and thus are less important than nonlinear interactions with perturbations as discussed in the following sections. Finally, viscous dissipation affects predominately these perturbations since they are of fine scale relative to the underlying beam (see §4.2.3).

4.2.3 Subharmonic perturbations

To examine the linear stability of (4.6) to PSI, we now specify the form of the subharmonic perturbations. According to the standard PSI analysis for sinusoidal wavetrains in the case of no mean flow, the most unstable perturbations $(\boldsymbol{k}_+, \omega_+)$ and $(\boldsymbol{k}_-, \omega_-)$ correspond to short-scale disturbances relative to the primary wave ($|\boldsymbol{k}_\pm| \gg |\boldsymbol{k}_0|$) and satisfy the triad resonance conditions

$$\boldsymbol{k}_+ + \boldsymbol{k}_- = \boldsymbol{k}_0, \tag{4.7a}$$

$$\omega_+ + \omega_- = \omega_0 \tag{4.7b}$$

(e.g. Staquet & Sommeria, 2002; Bourget *et al.*, 2013). Making use of Galilean invariance, it is expected that these results will hold in the presence of a constant uniform mean flow, provided that we are in the reference frame moving with the mean flow. However, by virtue of the form of the frequency Doppler shift $\overline{\boldsymbol{u}} \cdot \boldsymbol{k}$ due to the mean flow, the triad resonance conditions in the fluid frame are equivalent to (4.7) in the stationary frame.

With these considerations in mind, we now turn to the beam (4.6) as the primary wave. Here, the subharmonic perturbations are taken in the form of fine-scale wavepackets that are modulated by the underlying beam (figure 4-1*b*). Furthermore, we consider the 'distinguished limit' where triad nonlinear interactions, dispersion, viscous dissipation and the background mean flow are equally important in the evolution of such perturbations. From prior experience (Karimi & Akylas, 2014), a balance of nonlinear and dispersive effects, acting on an $O(\epsilon^{-1})$ time scale, is achieved when

$$\mu = \epsilon^{1/2} \tag{4.8}$$

and the perturbations have carrier wavevectors $\boldsymbol{k}_\pm = O(\epsilon^{-1/2})$. Thus, to satisfy the wavevector resonance condition $\boldsymbol{k}_+ + \boldsymbol{k}_- = \boldsymbol{k}_0$, we write

$$\boldsymbol{k}_\pm = \pm \frac{\kappa}{\epsilon^{1/2}} \hat{\boldsymbol{e}}_\zeta + \frac{1}{2}\boldsymbol{k}_0, \tag{4.9}$$

where $\hat{\boldsymbol{e}}_\zeta$ is a unit vector along $\zeta = x \sin\phi + y\cos\phi$, with the inclination angle ϕ to be determined. Here, the parameter $\kappa = O(1)$, taken to be positive without loss of generality, controls the carrier wavenumber of the perturbation wavepackets and will play a central role in the determination of the maximum PSI growth rate. Additionally, in order for dispersion, which causes such perturbations to propagate with their $O(\epsilon^{1/2})$ group velocity across the envelope, to be as important as the advection due to the mean flow $\overline{u}$, it is necessary to take the mean flow to be $O(\epsilon^{1/2})$:

$$\overline{u} \to \epsilon^{1/2}\overline{u}. \tag{4.10}$$

As a result, the effects of the mean flow on the primary beam, discussed in §4.2.2, will be small.

Substituting (4.3), (4.9) and (4.10) into the dispersion relation (4.2), we find the following expressions for the subharmonic frequencies

$$\omega_\pm = \sin\phi(1 \pm \overline{u}\kappa) \pm \epsilon^{1/2}\left\{\frac{1}{2\kappa}(\sin\theta - \sin\phi\cos\chi) \pm \frac{\overline{u}\sin\theta}{2}\right\}, \tag{4.11}$$

where $\chi = \theta - \phi$. As argued earlier, these wave frequencies have to form a resonant triad with the beam frequency in the reference frame moving with the mean flow, which happens to be equivalent to forming a resonant triad in the stationary frame (viz. equation 4.7b). Making use of (4.3), (4.4), (4.9) and (4.11), the triad resonance condition (4.7b) determines ϕ:

$$\sin\phi = \frac{\sin\theta}{2}. \tag{4.12}$$

4.2.4 Additional frequency components

Recently, in their study of PSI using a formal stability analysis based on Floquet theory in the absence of background mean flow, Fan & Akylas (2020*b*) (see Chapter 3) noted the presence of additional frequency components with frequency $3\omega_0/2$, where ω_0 is the primary wave frequency. Importantly, their results show that these $3\omega_0/2$ frequency components, which are generated via the interaction of the subharmonic perturbations with the primary wave, play a crucial role in PSI dynamics and were erroneously neglected by earlier analyses (e.g. Karimi & Akylas, 2014, 2017).

In view of these findings, in the present analysis of PSI with background mean flow, it is necessary to include in the perturbation frequency components with frequency $\omega_\pm + \omega_0$, which are analogous to the $3\omega_0/2$ frequency components for PSI in the absence of mean flow. Since they arise via the interaction of the subharmonic perturbations with the primary wave, these $\omega_\pm + \omega_0$ frequency components have the same fine-scale structure as the subharmonic perturbations. It should be noted that these additional frequency components were erroneously ignored in the published version of this thesis chapter (Fan & Akylas, 2019); however, they play no role in the instability growth rates of a nearly-monochromatic primary wave and therefore do not affect the results presented in Fan & Akylas (2019).

4.2.5 Evolution equations

At this point, we introduce infinitesimal perturbations in the form discussed above to the primary wave beam (4.6),

$$\begin{aligned}\psi = \psi_0 &+ \frac{\epsilon^{1/2}}{\kappa}\Big\{A(H,T)\mathrm{e}^{\mathrm{i}(\boldsymbol{k}_+\cdot\boldsymbol{x}-\omega_+ t)} + B(H,T)\mathrm{e}^{\mathrm{i}(\boldsymbol{k}_-\cdot\boldsymbol{x}-\omega_- t)} + \text{c.c.}\Big\}\\ &+ \frac{\epsilon}{\kappa}\Big\{\Big[A_3(H,T)\mathrm{e}^{\mathrm{i}(\boldsymbol{k}_+\cdot\boldsymbol{x}-\omega_+ t)} + B_3(H,T)\mathrm{e}^{\mathrm{i}(\boldsymbol{k}_-\cdot\boldsymbol{x}-\omega_- t)}\Big]\mathrm{e}^{\mathrm{i}(\eta-\omega_0 t)} + \text{c.c.}\Big\},\end{aligned} \tag{4.13a}$$

$$\begin{aligned}\rho = \rho_0 &+ \Big\{F(H,T)\mathrm{e}^{\mathrm{i}(\boldsymbol{k}_+\cdot\boldsymbol{x}-\omega_+ t)} + G(H,T)\mathrm{e}^{\mathrm{i}(\boldsymbol{k}_-\cdot\boldsymbol{x}-\omega_- t)} + \text{c.c.}\Big\}\\ &+ \epsilon^{1/2}\Big\{\Big[F_3(H,T)\mathrm{e}^{\mathrm{i}(\boldsymbol{k}_+\cdot\boldsymbol{x}-\omega_+ t)} + G_3(H,T)\mathrm{e}^{\mathrm{i}(\boldsymbol{k}_-\cdot\boldsymbol{x}-\omega_- t)}\Big]\mathrm{e}^{\mathrm{i}(\eta-\omega_0 t)} + \text{c.c.}\Big\},\end{aligned} \tag{4.13b}$$

Here, the perturbation envelope amplitudes $A, B, F, G, A_3, B_3, F_3$ and G_3 are modulated in H owing to their interaction with the primary beam, and $T = \epsilon t$ is the slow time on which dispersion, nonlinear interactions and the mean flow affect the perturbations. Furthermore, as in Karimi & Akylas (2014), we scale the inverse Reynolds number, $\nu = 2\alpha\epsilon^2$, where α is an $O(1)$ viscous parameter, to bring dissipation to the same level as these effects. Note that in view of (4.5) and (4.10), $H = \epsilon^{1/2}\eta + O(\epsilon)$, which simplifies the ensuing calculations significantly.

Inserting (4.13) into (4.1), linearizing with respect to the perturbations, and grouping terms according to each frequency component, we find that the amplitudes of the $\omega_\pm + \omega_0$ frequency components are given to leading order as

$$A_3 = F_3 = -\mathrm{i}\frac{\kappa \sin\chi}{2\sin\phi}AQ, \qquad B_3 = -G_3 = \mathrm{i}\frac{\kappa\sin\chi}{2\sin\phi}BQ. \tag{4.14}$$

Turning now to the subharmonic perturbations with frequency $\omega_\pm$, making use of (4.14) and eliminating F and G, we obtain the following coupled evolution equations for A and B,

$$A_T + \frac{1}{D}\Big(\frac{c}{\kappa} + \overline{u}\sin\theta\Big)A_H + \mathrm{i}\frac{c'}{8\kappa^2}A + \alpha\kappa^2 A - \gamma Q B^* = 0, \tag{4.15a}$$

$$B_T - \frac{1}{D}\Big(\frac{c}{\kappa} - \overline{u}\sin\theta\Big)B_H + \mathrm{i}\frac{c'}{8\kappa^2}B + \alpha\kappa^2 B - \gamma Q A^* = 0, \tag{4.15b}$$

where

$$\begin{gathered} c = \sin\theta - \sin\phi\cos\chi, \quad c' = 3\sin\phi\cos^2\chi - 2\sin\theta\cos\chi - \sin\phi, \\ \gamma = \sin\chi\cos^2\left(\frac{\chi}{2}\right). \end{gathered} \tag{4.16}$$

Here, in order to bring out the effect of the finite width of the primary beam, we have taken $Q(H)$ to have fixed $O(1)$ width by rescaling $H \to H/D$, where $D = 2\pi N\epsilon^{1/2}$ is the nondimensional width of the beam envelope and $N = O(\epsilon^{-1/2})$ is the number of carrier wavelengths contained in the beam. In (4.15), the first two terms represent the propagation of the subharmonic wavepackets across the beam with the projection of their group velocity on the modulation direction. The third term corresponds to envelope dispersion, fourth to viscous dissipation, and fifth to nonlinear energy transfer from the primary wave. Thus, the leading-order effect of the small mean flow is to advect each subharmonic wavepacket and modify its group velocity. In the limit $\overline{u} \to 0$, we recover the results of Karimi & Akylas (2014). Furthermore, if Q is not locally confined, i.e. in the limit of $D \to \infty$, the group velocity and the effect of $\overline{u}$ vanish, and we recover the PSI of a sinusoidal wavetrain.

It is worth noting that the coupled evolution equations (4.15) differ from those found by Fan & Akylas (2019) (the published version of this thesis chaper) in that the terms proportional to $|Q_\eta|^2$ have now vanished as a result of the inclusion of the $\omega_\pm + \omega_0$ frequency components. However, since these terms do not affect the instability growth rates (Fan & Akylas, 2019), the ensuing results are largely unchanged.

4.3 Stability eigenvalue problem

We now proceed to solve (4.15) for a locally confined beam envelope ($Q \to 0$ as $H \to \pm\infty$) in order to examine the effect of the background mean flow on PSI. To this end, we first make the substitution

$$(A, B^*) \to (A, B^*) \exp\left[\mathrm{i}\frac{D\kappa}{c}\left(\frac{c'\overline{u}\sin\theta}{8\kappa^2 D}T - \frac{c'}{8\kappa^2}H\right)\right], \tag{4.17}$$

which eliminates in (4.15) the dispersive terms proportional to c'. Next, we search for normal mode solutions

$$(A, B^*) = (a, b^*)\mathrm{e}^{\lambda T}, \tag{4.18}$$

where $\lambda = \lambda_r + \mathrm{i}\lambda_i$ and $\lambda_r > 0$ implies instability. Thus, we obtain the eigenvalue problem

$$(1+\hat{u})a_H + \hat{\lambda}a - \hat{\kappa}Qb^* = 0, \tag{4.19a}$$

$$(1-\hat{u})b^*_H - \hat{\lambda}b^* + \hat{\kappa}Q^*a = 0, \tag{4.19b}$$

$$(a, b^*) \to 0 \quad (H \to \pm\infty), \tag{4.19c}$$

with

$$\hat{u} = \frac{\kappa\sin\theta}{c}\overline{u}, \quad \hat{\lambda} = \frac{D\kappa}{c}(\lambda + \alpha\kappa^2), \quad \hat{\kappa} = \frac{D\gamma}{c}\kappa. \tag{4.20}$$

For given beam envelope profile $Q(H)$, background mean flow $\overline{u}$ and perturbation wavenumber κ, solving (4.19) determines the eigenvalue spectrum $\hat{\lambda}$, and instability arises ($\lambda_r > 0$) only if $\hat{\lambda}_r(\kappa) > \alpha D\kappa^3/c$. Thus, $\hat{\lambda}_r$ is proportional to the inviscid growth rate ($\hat{\lambda}_r \propto \lambda_r$ if $\alpha = 0$), whereas the actual growth rate λ_r takes into account the effect of viscous dissipation.

As a simple example to illustrate the effect of the background mean flow on PSI, we solve the eigenvalue problem (4.19) for the 'top-hat' envelope profile

$$Q(H) = \begin{cases} 1/2 & (|H| \le 1/2) \\ 0 & (|H| > 1/2), \end{cases} \tag{4.21}$$

corresponding to a beam that comprises a uniform sinusoidal wave with peak amplitude ϵ and finite width. Because Q is piecewise constant, it is possible to solve (4.19) analytically in $|H| > 1/2$ and $|H| \le 1/2$. Then, matching these solutions to ensure that a and b^* are continuous at $H = \pm 1/2$ leads to the characteristic equation for $\hat{\lambda}$.

First, consider the case where $|\hat{u}| < 1$. The solution to (4.19) can be expressed, up to a normalization constant, as

$$(a,b^*) = (1,0)\mathrm{e}^{-\hat{\lambda}H/(1+\hat{u})} \quad (H > 1/2), \tag{4.22a}$$

$$(a,b^*) = \mathbb{D}(0,1)\mathrm{e}^{\hat{\lambda}H/(1-\hat{u})} \quad (H < -1/2), \tag{4.22b}$$

$$(a,b^*) = \big\{\mathbb{D}_+(1,\mathbb{B}_+)\mathrm{e}^{\mathrm{i}\sigma H} + \mathbb{D}_-(1,\mathbb{B}_-)\mathrm{e}^{-\mathrm{i}\sigma H}\big\}\mathrm{e}^{\hat{\lambda}\hat{u}H/(1-\hat{u}^2)} \quad (|H| < 1/2), \tag{4.22c}$$

where

$$\sigma = \sqrt{\frac{1}{1-\hat{u}^2}\left(\frac{\hat{\kappa}^2}{4} - \frac{\hat{\lambda}^2}{1-\hat{u}^2}\right)}, \quad \mathbb{B}_\pm = \frac{2}{\hat{\kappa}(1-\hat{u})}\Big(\hat{\lambda} \pm \mathrm{i}(1-\hat{u}^2)\sigma\Big). \tag{4.23}$$

Here, $\mathbb{D}, \mathbb{D}_+, \mathbb{D}_-$ are constants determined by enforcing continuity of a and b^* at $H = \pm 1/2$. For a nontrivial solution to exist, we obtain the characteristic equation

$$\frac{\hat{\lambda}}{1-\hat{u}^2}\sin\sigma + \sigma\cos\sigma = 0 \tag{4.24}$$

that determines $\hat{\lambda}$; then λ follows directly via (4.20). It is easy to verify that (4.24) does not depend on the sign of $\overline{u}$. Thus, for a given envelope profile $Q(H)$, the growth rates are symmetric in $\overline{u}$. On the other hand, in view of (4.5), for a given wave source, the envelope profile $Q(H)$ will differ depending on the sign of $\overline{u}$, but these effects will be small given the small mean flow (viz. (4.10)).

Turning next to the case $|\hat{u}| > 1$, the solution to (4.19) in each region where Q is constant can again be readily obtained and has similar form as (4.22). However, upon matching these piecewise solutions, it is concluded that no nontrivial solutions exist with $\hat{\lambda}_r > 0$. Therefore, all disturbances are stable, regardless of viscosity. For $|\hat{u}| = 1$, it is also readily shown by returning to (4.19) that no unstable solutions exist either. Therefore, PSI only exists when $|\hat{u}| < 1$, or equivalently,

$$\kappa < \left|\frac{c}{\overline{u}\sin\theta}\right|. \tag{4.25}$$

Importantly, this condition arises only for finite beam width D and, in view of the group velocity terms in (4.15), can be physically interpreted as a requirement that the two subharmonic wavepackets propagate in opposite directions. Furthermore, (4.25) suggests that the range of possible unstable wavenumbers shrinks to zero as $\overline{u} \to \infty$, consistent with the arguments made later (see §4.5) that no instability is possible for a dimensionless mean flow of $O(1)$ magnitude.

4.4 Results

We now present stability results based on the characteristic equation (4.24) for the specific parameter values $\theta = \pi/4$, $\epsilon = 0.3$, $\nu = 0.004$, $D = 5$, and various $\overline{u} \geq 0$ (e.g. for $\nu_* = 10^{-6}$ m^2/s, corresponding to water, and $N_* = 1$ rad/s, taking $\nu = 0.004$ implies $\Lambda_* \approx 10$ cm).

These values are representative of laboratory flow conditions (e.g. Bourget *et al.*, 2014). Earlier analyses of finite-width PSI with no mean flow (Bourget *et al.*, 2014; Karimi & Akylas, 2014) focused on the importance of the width D, and in particular, the existence of a critical value $D = D_c$ below which no PSI is possible (Karimi & Akylas, 2014). As the emphasis here is on the effects of the background mean flow $\overline{u}$ on PSI growth, we take $D = 5$ such that $D > D_c \approx 2$ for the chosen parameters. Furthermore, as $\overline{u}$ is varied, the beam inclination angle θ is kept fixed and the forcing frequency ω_0 is allowed to adjust accordingly via (4.4), as opposed to the other way around. This makes it possible to compare the effect of the mean flow for a fixed primary wave beam, although given the small mean flow, both choices produce qualitatively similar results. Figure 4-2(*a,b*) shows the eigenvalue branches $\hat{\lambda}_r$ as functions of κ for $\overline{u} = 0$ and $\overline{u} = 0.2$, as well as the cubic $\alpha D\kappa^3/c$. It is clear that as a whole, the addition of the background mean flow has decreased the eigenvalues and therefore reduced the growth rates for PSI.

For $\overline{u} = 0$ (figure 4-2*a*), (4.24) admits a countably infinite number of eigenvalue branches that bifurcate at discrete non-zero values along the κ-axis. As shown by Karimi & Akylas (2014), when κ is much greater than the first bifurcation point, the first eigenvalue branch (lowest mode) has the highest growth rate and behaves as $\hat{\lambda}_r \sim D\gamma\kappa/(2c)$. Therefore, for nonzero viscosity, the cubic $\alpha D\kappa^3/c$ will always exceed $\hat{\lambda}_r$ for large enough κ, restricting unstable wavenumbers to a finite range of κ. In the inviscid limit ($\alpha = 0$), there is then no upper bound to the range of unstable wavenumbers. On the other hand, for $\overline{u} = 0.2$ (figure 4-2*b*), there exists an upper bound on the range of eigenvalues with positive $\hat{\lambda}_r$, suggesting that very short wavelength perturbations are stabilized by the mean flow even in the absence of viscosity. This can be understood in view of the necessary condition for instability (4.25) noted earlier. Moreover, for the top-hat profile (4.21), the first bifurcation point can be found analytically

$$\kappa = \frac{\pi c}{\sqrt{D^2\gamma^2 + \pi^2\overline{u}^2\sin^2\theta}}, \tag{4.26}$$

and provides a lower bound to the unstable range of wavenumbers.

Figure 4-2(*c*,*d*) plots the range of unstable wavenumbers as well as the maximum PSI growth rates for various values of $\overline{u}$, indicating that the presence of mean flow significantly shrinks the range of unstable wavenumbers and decreases the PSI growth rates. For instance, according to figure 4-2(*d*) the maximum instability growth rate is cut in about half by taking $\overline{u} = 1$, which corresponds to a dimensional mean flow of about 9 mm/s. However, in spite of this dramatic weakening of PSI, the mean flow never completely eliminates the instability, as there always exists a small but finite range of unstable wavenumbers for any $\overline{u}$ (figure 4-2*c*). We suspect that this is a limitation of our asymptotic theory as the unstable wavenumber range shifts towards $\kappa \ll 1$ when $\overline{u}$ is increased, in keeping with (4.25), invalidating the scaling assumptions made earlier.

While the mean flow weakens PSI for beams with $D > D_c$, as shown by the above example, it is also possible with the addition of sufficient mean flow to induce PSI for

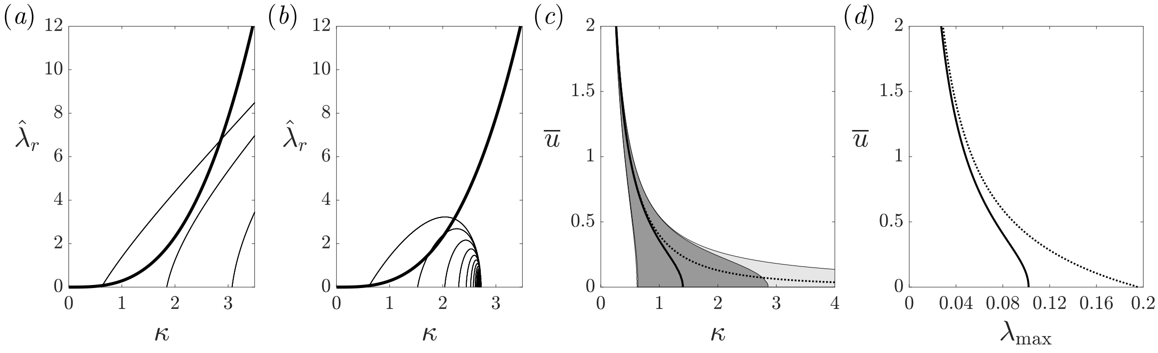

Figure 4-2: Eigenvalues and growth rates for the top-hat profile with $\theta = \pi/4$, $\epsilon = 0.3$, $\nu = 0.004$, and $D = 5$. When varying $\overline{u}$, the beam inclination angle θ was fixed. (a) Plot of the real eigenvalue branches $\hat{\lambda}_r(\kappa)$ for $\overline{u} = 0$ (thin lines), as well as the cubic $\alpha D\kappa^3/c$ (thick line) that controls viscous dissipation. Instability arises if $\hat{\lambda}_r > \alpha D\kappa^3/c$. ($b$) Same as ($a$), but for $\overline{u} = 0.2$. (c) Range of unstable wavenumbers (shaded in dark gray) as $\overline{u}$ is varied. The wavenumber with the maximum growth rate is indicated by the thick black line. The corresponding range for $\nu = 0$ is shown in light gray (which completely contains the dark gray region), with maximum growth rate locus indicated by the dotted line. (d) Plot of the maximum PSI growth rate $\lambda_{\max}$ as function of $\overline{u}$. The corresponding growth rates for $\nu = 0$ are plotted with the dotted line.

beams with $D < D_c$ that would be entirely stable in the absence of mean flow. To explain this apparent anomaly, we note that increasing $\overline{u}$ decreases the lower bound for instability, namely (4.26), and shifts the range of unstable wavenumbers to smaller κ (as seen in figure 4-2c). Because the effects of viscous dissipation are weaker for smaller κ, it is now possible for these low wavenumber modes to overcome viscous damping and lead to PSI. However, this mean-flow-induced PSI is extremely weak. For instance, using the same parameters as in figure 4-2 ($\theta = \pi/4$, $\epsilon = 0.3$, $\nu = 0.004$) but with $D = 1.5 < D_c \approx 2$, the maximum PSI growth rate attained as $\overline{u}$ is varied is $\lambda_{\max} \approx 0.01$, while the range of unstable wavenumbers (difference in κ) is quite narrow (about 0.1).

4.5 Concluding remarks

We have studied the effect of a background constant horizontal mean flow on the PSI of finite-width nearly monochromatic internal wave beams. As in Karimi & Akylas (2014), the subharmonic perturbations are in the form of short-scale wavepackets that are modulated by the underlying beam and can also extract energy via resonant triad interactions. In order for the advection by the mean flow to be as important as the propagation of such disturbances with their group velocity across the beam, and to also achieve a balance with the effects of triad nonlinearity and viscous dissipation, it is necessary to take the mean flow to be small. This distinguished limit is governed by the similar evolution equations as those derived in Karimi & Akylas (2014) after taking into account the $\omega_\pm + \omega_0$ frequency components revealed by Fan & Akylas (2020*b*), with the exception of a mean flow term that affects the group velocity of the subharmonic perturbations. For a nearly monochromatic beam with a top-hat envelope profile, this new term stabilizes very short-scale perturbations in keeping with the necessary condition for instability (4.25), and thus shifts the most unstable disturbance to longer wavelengths even for inviscid or nearly inviscid flow conditions. Physically, this necessary condition implies that unstable perturbations must propagate in opposite directions across the beam in order for PSI to arise in the presence of the mean flow. As a result, it is possible for a small amount of mean flow to weaken PSI dramatically. Although these findings were derived analytically for the top-hat envelope profile, similar results are expected for other types of locally-confined envelope profiles. Finally, these results are unique to finite-width beams (D finite in (4.15)), as the background mean flow has no effect on the PSI of a purely sinusoidal plane wave once the Doppler shift of the wave frequency has been taken into account (viz. (4.4)).

It is worth mentioning that for $O(1)$ mean flow (i.e. $\overline{u} = O(1)$ instead of $\overline{u} = O(\epsilon^{1/2})$ in (4.10)), it is still possible to balance the mean flow advection of subharmonic perturbations and nonlinear energy transfer over the same $O(\epsilon^{-1})$ time scale by assuming a larger beam envelope scale, namely $1/\mu = 1/\epsilon$ instead of $1/\mu = 1/\epsilon^{1/2}$ in (4.8). The evolution equations obtained under these alternative scalings are nearly identical to (4.15) with the exception that the effect of the group velocity is rendered negligible relative to the advection by the mean flow. As a result, the perturbations are advected in the same direction across the beam and according to the necessary condition for PSI noted above for the top-hat envelope profile, no instability is possible in this instance.

The present theory assumes waves with nearly monochromatic spatial profile and ignores the effects of background rotation. These flow conditions preclude direct comparisons with oceanic internal waves, although a rough estimate for the dimensional mean flow strength needed to impact PSI can still be obtained. Using $\theta = \pi/4, \epsilon = 0.3$, and $D = 5$ as in §4, but with the choice $\nu \approx 0$ relevant to the oceanic case, the maximum instability growth rate is cut in about half by taking $\overline{u} = 0.5$, which corresponds to a rather small dimensional mean flow of about 2 cm/s (using $N_* = 10^{-3}$ s^{-1} and $\Lambda_* = 500$ m as representative oceanic values). A separate theory that accounts for background mean flow in the presence of rotation and focuses on near-inertial PSI, which is most relevant to oceanic internal waves, will be presented elsewhere.

THIS PAGE INTENTIONALLY LEFT BLANK

Chapter 5

Near-inertial PSI of internal wave beams in a background mean flow

5.1 Introduction

In its simplest form, the parametric subharmonic instability (PSI) of internal gravity waves in continuously stratified fluids involves transfer of energy from a sinusoidal primary wavetrain to two subharmonic perturbations via a weakly nonlinear resonant triad interaction (Staquet & Sommeria, 2002). Importantly, for nearly inviscid flows, the most unstable perturbations have frequency equal to half that of the primary wave and short wavelength relative to the primary wave. PSI has therefore been proposed as a potential pathway by which internal waves transfer their energy into smaller scales and eventually dissipate (e.g. Hibiya *et al.*, 2002; MacKinnon & Winters, 2005; Young *et al.*, 2008).

However, oceanic internal waves are not necessary sinusoidal and may not be well approximated by theories of sinusoidal plane wave PSI (Alford *et al.*, 2007; Hazewinkel & Winters, 2011; MacKinnon *et al.*, 2013). Rather, oceanic internal waves commonly manifest as wave beams – time-harmonic plane waves with locally confined spatial profile (Tabaei & Akylas, 2003; Sutherland, 2013) – that arise from the interaction of the barotropic tide with bottom topography in oceans (e.g. Lamb, 2004; Peacock *et al.*, 2008; Johnston *et al.*, 2011). Recent work on the PSI of internal wave beams have shown that the finite width of the beam imposes additional constraints on PSI because subharmonic perturbations, which propagate across the beam with their group velocity, will eventually leave the beam (Bourget *et al.*, 2014; Karimi & Akylas, 2014, 2017). As a result, PSI is only possible if either (i) the beam has nearly monochromatic profile and is sufficiently wide to allow subharmonic perturbations to stay in contact with the beam for a long enough time (Karimi & Akylas, 2014), or (ii) the beam has arbitrary general profile but has frequency close to $2f$, where f is the Coriolis frequency, in which case subharmonic perturbations with half the primary frequency are near-inertial with nearly vanishing group velocity, prolonging their contact with the primary beam (Karimi & Akylas, 2017).

Recently, Fan & Akylas (2019) revisited the PSI of internal wave beams and considered the additional effect of a background mean flow in an effort to study PSI in more realistic settings. We found that mean flow weakens PSI dramatically by hindering the ability of the subharmonic perturbations to extract energy from the primary wave. This stabilizing effect of the mean flow is unique to finite-width beams as mean flow has no effect on the PSI of a purely sinusoidal plane wave once the Doppler shift of the wave frequency has been taken into account. However, in Fan & Akylas (2019), we focused on beams with nearly monochromatic profile and did not include the effects of background rotation. While recent numerical experiments (Richet *et al.*, 2017) indicate that near-inertial PSI is also weakened by a background mean flow, our earlier study could not make direct comparisons to oceanic internal waves as we ignored the effect of background rotation.

The present analysis explores the effect of a background mean flow on the near-inertial PSI of internal wave beams with general profile. Similar to the approach of Fan & Akylas (2019), we first discuss the effects of the mean flow on the primary beam profile itself. Here, waves are generated by a source with general locally confined profile and thus contain broadband wavenumber spectrum. As a result, it is necessary to assume that the mean flow is small in order to ensure that the mean flow does not destroy the beam entirely of its own accord. We then derive evolution equations for near-inertial fine-scale perturbations under a 'distinguished limit', where coupling with the primary wave, dispersion, viscous dissipation, and the background mean flow partake in the perturbation dynamics on an equal footing. By calculating the growth rates and eigenvalue spectra for a locally confined beam profile, we find that background mean flow can either hinder or facilitate the ability of perturbations to extract energy from a finite-width beam, depending on both the sign of the mean flow and the frequency of the primary wave. However, sufficiently large background mean flow of either sign stabilizes perturbations and weakens PSI dramatically.

5.2 Formulation

5.2.1 Preliminaries

Our analysis assumes two-dimensional disturbances in an unbounded, incompressible, uniformly stratified Boussinesq fluid with constant buoyancy frequency N_*, and will use nondimensional variables with $1/N_*$ as the time scale and L_* as the length scale, to be specified later. We take x to be the horizontal coordinate, y the vertical coordinate pointing antiparallel to gravity, and $\overline{\boldsymbol{u}} = \overline{u}\,\hat{\boldsymbol{e}}_x$ as the uniform horizontal background mean flow with respect to a fixed reference frame. In this fixed frame, the streamfunction $\psi(x, y, t)$ for the in-plane velocity field $(\psi_y, -\psi_x)$, the transverse velocity $w(x, y, t)$, and the reduced density $\rho(x, y, t)$

are governed by

$$(\partial_t + \overline{u}\,\partial_x)\nabla^2\psi - \rho_x + f w_y + J(\nabla^2\psi, \psi) - \nu\nabla^4\psi = 0, \tag{5.1a}$$

$$(\partial_t + \overline{u}\,\partial_x)w - f\psi_y + J(w, \psi) - \nu\nabla^2 w = 0, \tag{5.1b}$$

$$(\partial_t + \overline{u}\,\partial_x)\rho + \psi_x + J(\rho, \psi) = 0. \tag{5.1c}$$

Here, $J(a, b) = a_x b_y - a_y b_x$ stands for the Jacobian, f is the local Coriolis parameter under the f-plane approximation, and $\nu = \nu_*/N_* L_*^2$ is the inverse Reynolds number where ν_* is the fluid kinematic viscosity. In the linear, inviscid limit ($\nu = 0$), equations (5.1) admit sinusoidal plane wave solutions that obey the dispersion relation

$$(\omega_0 - \overline{u}\,|\boldsymbol{k}|\sin\theta)^2 = f^2 + (1 - f^2)\sin^2\theta, \tag{5.2}$$

where ω_0 is the wave frequency, $|\boldsymbol{k}|$ is the magnitude of the wavevector $\boldsymbol{k}$ and θ is the inclination of $\boldsymbol{k}$ to the vertical. In (5.2), it is useful to note that the quantity in parentheses is the (Doppler shifted) frequency of the wave in the reference frame moving with the background mean flow.

5.2.2 Primary wave beam

When $\overline{u} = 0$, (5.2) reduces to the well-known internal wave dispersion relation, where the inclination of the wavevector to the vertical alone determines the frequency. In such a setting, by superposing sinusoidal plane waves with the same frequency ω_0 but varying $|\boldsymbol{k}|$, it is then possible to construct infinitely long uniform wave beam solutions

$$\psi_0 = Q(\eta)\mathrm{e}^{-\mathrm{i}\omega_0 t} + \text{c.c.}, \quad w_0 = \mathrm{i}\frac{f\cos\theta}{\omega_0}Q_\eta \mathrm{e}^{-\mathrm{i}\omega_0 t} + \text{c.c.}, \quad \rho_0 = -\mathrm{i}\frac{\sin\theta}{\omega_0}Q_\eta \mathrm{e}^{-\mathrm{i}\omega_0 t} + \text{c.c.}, \tag{5.3}$$

where $Q(\eta)$ is a general profile (related to the wave source) that varies in the cross-beam direction $\eta = x\sin\theta + y\cos\theta$, L_* is taken to be a characteristic length scale of the beam profile, and θ is related to beam frequency ω_0 via (5.2). Such uniform beams happen to be exact nonlinear states (Tabaei & Akylas, 2003) and form the basis of the analyses of Karimi & Akylas (2017) and Fan & Akylas (2020*b*) of PSI in near-inertial locally-confined beams.

On the other hand, for $\overline{u} \neq 0$, the wave frequency is no longer independent of $|\boldsymbol{k}|$ and each wavevector $\boldsymbol{k}$ generated by a locally-confined source (with fixed frequency) will be affected by the mean flow to varying extents. As a result, the profile Q in (5.3) will also feature variations in the along beam (ξ-) direction, orthogonal to η and defined by $\xi = x\cos\theta - y\sin\theta$ (figure 5-1*a*). To prevent this dispersive effect of the mean flow from destroying the beam of its own accord, and to permit the possibility of PSI, we therefore focus on the case of weak mean flow and introduce the scaling

$$\overline{u} \to \mu\overline{u}, \tag{5.4}$$

where $0 < \mu \ll 1$ is a small scaling parameter to be specified later. Inserting (5.4) into (5.1) and allowing for ξ-variations in Q, we find at leading order

$$\mu \overline{u} \sin\theta \, Q_{\eta\eta} + \mathrm{i} \frac{(1 - f^2) \sin\theta \cos\theta}{\omega_0} Q_\xi = 0. \tag{5.5}$$

Here, the two terms represent a balance between the effects of the mean flow and along-beam variations, which suggests that the latter have $O(\mu^{-1})$ length scale. As we are ultimately interested in the stability to fine-scale perturbations (relative to L_*), these slow ξ-variations may therefore be neglected in the PSI analysis: at a given $\xi = \xi_0$, the beam locally appears uniform (see figure 5-1*b*), which allows (5.3) to be taken as the basic state in the ensuing stability analysis provided L_* and Q are taken at ξ_0.

As our analysis centres on PSI for small-amplitude beams, we assume

$$Q \to \epsilon Q, \tag{5.6}$$

where $\epsilon = U_*/N_* L_* \ll 1$ is a nondimensional amplitude parameter and U_* is a (dimensional) characteristic along-beam velocity. In addition, for beams of general locally-confined profile to suffer PSI, it is necessary for their frequency ω_0 to be close to $2f$ (Karimi & Akylas, 2017; Fan & Akylas, 2020*b*) so that perturbations at half this frequency will be near-inertial and thus have vanishing group velocity, prolonging their interaction with the primary wave. Therefore, we specify

$$\omega_0 = 2f + \delta\sigma, \tag{5.7}$$

where $0 < \delta \ll 1$ is a small scaling parameter, to be made precise later, and $\sigma = O(1)$ is a detuning parameter. Here, σ may be either positive or negative, implying that the perturbations at half this frequency may be either super-inertial or sub-inertial.

5.2.3 Fine-scale perturbations

With the basic state (5.3) specified, it remains now to specify the form of the perturbations used in the ensuing linear stability analysis. According to PSI theory in the absence of mean flow, the primary wave is unstable to two fine-scale subharmonic wavepackets with frequency approximately $\omega_0/2$. From prior experience (Karimi & Akylas, 2017; Fan & Akylas, 2020*b*), PSI requires such perturbations have $O(\epsilon^{-1/2})$ carrier wavenumber to ensure that the group velocity effect balances with the coupling of the perturbations with the primary wave. These effects are then balanced with the effects of detuning and viscosity via the scalings

$$\delta = \epsilon, \qquad \nu = \alpha\epsilon^2, \tag{5.8}$$

where α is an $O(1)$ viscous parameter, and

$$T = \epsilon t \tag{5.9}$$

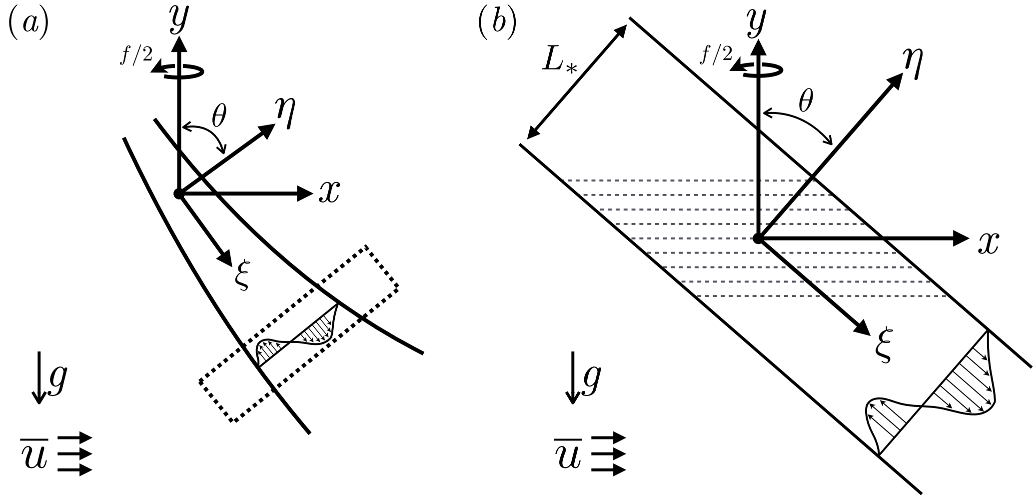

Figure 5-1: Schematic of the PSI geometry. (*a*) Locally confined primary wave beam of general profile with frequency ω_0 and $O(1)$ width in the presence of a small background mean flow $\overline{u}$. According to (5.5), the beam profile will feature slow variations in ξ. (*b*) Close-up view of the beam slice shown in the dotted box in (*a*). The beam geometry at any given ξ-location can be assumed to be uniform along ξ since ξ-variations have a much longer length scale than η-variations. Subharmonic perturbations with frequency $\omega_0/2$ are taken to have short vertical scale and have nearly horizontal lines of constant phase (dotted lines) since they are near-inertial.

is the slow time scale over which this 'distinguished limit' occurs. As a result of (5.8), subharmonic perturbations with half the primary wave frequency (5.7) thus have frequency close to

$$\frac{\omega_0}{2} = f + \frac{\sigma}{2}\epsilon, \tag{5.10}$$

and in view of (5.2), have nearly vertical wavevectors. In the present analysis, owing to the assumption of weak mean flow (5.4), it is possible to formally incorporate the leading order effects of the mean flow into the rest of the PSI dynamics by setting

$$\mu = \epsilon. \tag{5.11}$$

Recently, Fan & Akylas (2020*b*), noted the presence of frequency components with frequency $3\omega_0/2$ when studying PSI using a formal stability analysis based on Floquet theory. Importantly, their results show that these $3\omega_0/2$ frequency components, which are generated via the interaction of the subharmonic perturbations with the primary wave, play a crucial role in PSI dynamics and were erroneously neglected by earlier analyses (e.g. Karimi & Akylas, 2017). Therefore, based on these considerations, we introduce infinitesimal perturbations to the primary wave beam (5.3) as follows:

$$\begin{aligned}\psi = \psi_0 + \frac{\epsilon^{1/2}}{\kappa}\Big\{\Big[A\mathrm{e}^{\mathrm{i}\kappa y/\epsilon^{1/2}} + B\mathrm{e}^{-\mathrm{i}\kappa y/\epsilon^{1/2}}\Big]\mathrm{e}^{-\mathrm{i}\omega_0 t/2} + \text{c.c.}\Big\}& \\ + \frac{\epsilon}{\kappa}\Big\{\Big[A_3\mathrm{e}^{\mathrm{i}\kappa y/\epsilon^{1/2}} + B_3\mathrm{e}^{-\mathrm{i}\kappa y/\epsilon^{1/2}}\Big]\mathrm{e}^{-\mathrm{i}3\omega_0 t/2} + \text{c.c.}\Big\},&\end{aligned} \tag{5.12a}$$

$$\begin{aligned}w = w_0 + \Big\{\Big[M\mathrm{e}^{\mathrm{i}\kappa y/\epsilon^{1/2}} + N\mathrm{e}^{-\mathrm{i}\kappa y/\epsilon^{1/2}}\Big]\mathrm{e}^{-\mathrm{i}\omega_0 t/2} + \text{c.c.}\Big\}& \\ + \epsilon^{1/2}\Big\{\Big[M_3\mathrm{e}^{\mathrm{i}\kappa y/\epsilon^{1/2}} + N_3\mathrm{e}^{-\mathrm{i}\kappa y/\epsilon^{1/2}}\Big]\mathrm{e}^{-\mathrm{i}3\omega_0 t/2} + \text{c.c.}\Big\},&\end{aligned} \tag{5.12b}$$

$$\rho = \rho_0 + \epsilon^{1/2}\Big\{\Big[F\mathrm{e}^{\mathrm{i}\kappa y/\epsilon^{1/2}} + G\mathrm{e}^{-\mathrm{i}\kappa y/\epsilon^{1/2}}\Big]\mathrm{e}^{-\mathrm{i}\omega_0 t/2} + \text{c.c.}\Big\}, \tag{5.12c}$$

where the perturbation envelopes $A, B, A_3, B_3, M, N, M_3, N_3, F$ and G are taken to be functions of $(\boldsymbol{x}, T)$. Here, the near-inertial perturbations consist of two fine-scale wavepackets with vertical carrier wavevectors, in view of (5.7) and (5.8), of equal magnitude but opposite sign, and thus resonantly interact with the primary wave. The $3\omega_0/2$ frequency components are taken to have the same fine-scale structure as the subharmonic waves but with smaller amplitude, as shown by Fan & Akylas (2020*b*). Finally, the parameter $\kappa = O(1)$, taken to be positive without loss of generality, controls the vertical wavenumber of the perturbation wavepackets and will play a central role in the determination of the maximum PSI growth rate.

5.2.4 Evolution equations

Inserting (5.12) into (5.1), linearizing with respect to the perturbations, and collecting the various harmonics, we first find that

$$A_3 = -M_3 = -\frac{\kappa\sin\theta}{2f}AQ_\eta, \qquad B_3 = N_3 = \frac{\kappa\sin\theta}{2f}BQ_\eta. \tag{5.13}$$

As discussed, these $3\omega_0/2$ waves are generated via the nonlinear interaction between the subharmonic perturbations and the primary wave. Next, eliminating F, G, M, and N, and making use of (5.13), we obtain the following coupled evolution equations for A and B,

$$A_T - \mathrm{i}\frac{\sigma}{2}A + \overline{u}\sin\theta\, A_\eta - \mathrm{i}\frac{c'}{2\kappa^2}A_{\eta\eta} + \alpha\kappa^2 A + \gamma Q_{\eta\eta}B^* = 0, \tag{5.14a}$$

$$B_T - \mathrm{i}\frac{\sigma}{2}B + \overline{u}\sin\theta\, B_\eta - \mathrm{i}\frac{c'}{2\kappa^2}B_{\eta\eta} + \alpha\kappa^2 B + \gamma Q_{\eta\eta}A^* = 0, \tag{5.14b}$$

where

$$c' = 3f, \qquad \gamma = \frac{3}{4}\sin\theta\cos\theta. \tag{5.15}$$

Here, the second term of (5.14) corresponds to the effect of detuning, the third to the effect of the mean flow, the fourth to dispersion, the fifth to viscous dissipation, and the sixth to the coupling with the underlying wave. Based on (5.14), the leading order effect of the mean flow is to advect the subharmonic wavepackets, similar to the case in the PSI of nearly-monochromatic beams in a weak background mean flow (Fan & Akylas, 2019). Finally, it should be noted that even though we have allowed for general $O(1)$ variations in the perturbation envelopes, (5.14) can be written as a function of η only, indicating that ξ-variations have no effect on the stability to leading order.

5.2.5 Eigenvalue problem for $f \ll 1$

The linear equations (5.14) that describe the evolution of near-inertial perturbations depend on the primary beam profile $Q(\eta)$, as well as the independent parameters $(f, \sigma, \overline{u}, \alpha, \kappa)$. Although (5.14) can be readily solved (e.g. numerically), a comprehensive study across all values of these parameters is formidable. Therefore, we now shift focus for the rest of the study to the case where

$$f \ll 1, \tag{5.16}$$

an approximation that is well justified for oceanic internal waves where typically $f \lesssim 0.1$. In this limit, to achieve the same distinguished limit as found in (5.14), it is necessary to rescale

$$T \to fT, \quad \sigma \to f\sigma, \quad \alpha \to f\alpha \tag{5.17}$$

and note that to leading order, $\sin\theta = \sqrt{3}f$ and $\gamma = 3\sqrt{3}f/4$. In addition, to examine the linear stability of the primary beam, we look for solutions in the form of normal modes

$$(A, B^*) = (a, b^*)\mathrm{e}^{\lambda T}, \tag{5.18}$$

where $\lambda = \lambda_r + \mathrm{i}\lambda_i$ and $\lambda_r > 0$ implies instability. Thus, making use of (5.16)–(5.18), (5.14) reduces to

$$\Big(\hat{\lambda} - \mathrm{i}\frac{\sigma}{2}\Big)a + \overline{u}\sqrt{3}\,a_\eta - \mathrm{i}\frac{3}{2\kappa^2}a_{\eta\eta} + \frac{3\sqrt{3}}{4}Q_{\eta\eta}b^* = 0, \tag{5.19a}$$

$$\Big(\hat{\lambda} + \mathrm{i}\frac{\sigma}{2}\Big)b^* + \overline{u}\sqrt{3}\,b^*_\eta + \mathrm{i}\frac{3}{2\kappa^2}b^*_{\eta\eta} + \frac{3\sqrt{3}}{4}Q^*_{\eta\eta}a = 0, \tag{5.19b}$$

where

$$\hat{\lambda} = \lambda + \alpha\kappa^2. \tag{5.20}$$

For a given primary wave profile $Q(\eta)$, detuning σ, and mean flow $\overline{u}$, (5.19) defines eigenvalues $\hat{\lambda} = \hat{\lambda}(\kappa)$, and via (5.20), instability arises if $\hat{\lambda}_r(\kappa) > \alpha\kappa^2$. Thus, eigenvalues $\hat{\lambda}_r$ correspond to the inviscid growth rates, whereas the actual growth rate λ_r takes into account the effect of viscous dissipation. We now discuss the predictions of (5.19) for the PSI growth rates.

5.3 Sinusoidal plane wave

First, we examine the PSI of a uniform sinusoidal plane wave

$$Q = \frac{1}{2}\mathrm{e}^{\mathrm{i}\eta}, \tag{5.21}$$

corresponding to a primary wave with nondimensional peak amplitude ϵ and dimensional wavelength $2\pi L_*$. For this primary wave profile, normal mode solutions of (5.19) are found in the form

$$(a, b^*) = \left(a_0\mathrm{e}^{\mathrm{i}\eta/2}, b_0^*\mathrm{e}^{-\mathrm{i}\eta/2}\right)\mathrm{e}^{\mathrm{i}\rho\eta}, \tag{5.22}$$

where ρ is a real mode parameter. Upon substituting (5.21) and (5.22) into (5.19), we obtain a characteristic equation for λ that can be readily solved to find that

$$\lambda = \frac{3}{8}\sqrt{3-\mathbb{C}^2} - \alpha\kappa^2 - \mathrm{i}\left(\frac{3}{2\kappa^2} + \overline{u}\sqrt{3}\right)\rho \tag{5.23}$$

with

$$\mathbb{C} = \left(\frac{4}{3}\sigma' - \frac{1}{\kappa^2}\right) - \frac{4\rho^2}{\kappa^2}, \qquad \sigma' = \sigma - \overline{u}\sqrt{3}. \tag{5.24}$$

Here, the effect of the mean flow appears together with the detuning in the form of the parameter σ', which can be interpreted as the detuning in the reference frame of the fluid moving with the background mean flow. Indeed, according to (5.2), (5.7), (5.8) and (5.17), the primary wave in the reference frame of the fluid has frequency $\omega_f = \omega_0 - \epsilon\overline{u}\sin\theta = 2f(1+\epsilon\sigma'/2)$. This agrees with the fact that a constant, uniform, background mean flow has no affect on the PSI of a sinusoidal plane wave once the Doppler shift of the primary wave frequency is taken into account.

Based on (5.23) and (5.24), a necessary condition for PSI is that $\mathbb{C} > -\sqrt{3}$, or equivalently, $\kappa > \kappa_{\min} = \sqrt{3/(4\sigma' + 3\sqrt{3})}$. This implies that PSI is only possible for $\sigma' > -3\sqrt{3}/4$, which indicates that slightly sub-inertial perturbations (in the reference frame of the fluid) are indeed unstable, in agreement with the results of Young *et al.* (2008).

In the inviscid limit ($\alpha = 0$), the maximum growth rate $\lambda_r = 3\sqrt{3}/8$ is obtained when $\mathbb{C} = 0$, which is always possible for a suitable choice of ρ if the quantity in the parentheses in (5.24) is positive, or equivalently, $\kappa \geq \kappa_c = \sqrt{3/(4\sigma')}$. Therefore, for $\sigma' > 0$, PSI is universal for any $\kappa \geq \kappa_c$ with no scale selection. On the other hand, for $\sigma' \leq 0$, the maximum growth rate requires $\kappa \to \infty$, also in agreement with Young *et al.* (2008).

Under viscous flow conditions ($\alpha \neq 0$), high wavenumber modes are stabilized because the quadratic $\alpha\kappa^2$ in (5.23) will always exceed the inviscid growth rate. As a result, no instability is possible for $\kappa > \sqrt{3\sqrt{3}/(8\alpha)}$. In addition, for $\sigma' < 0$, the PSI growth rate monotonically decreases for $\kappa \geq \kappa_c$ owing to the increased effect of viscous dissipation and implies that the maximum PSI growth rate can always be found in the range $\kappa_{\min} < \kappa \leq \kappa_c$.

5.4 Locally confined beam

We now consider the case of a locally confined beam profile ($Q \to 0$ as $\eta \to \pm\infty$) and accordingly, we look for solutions of (5.19) that decay far from the beam:

$$(a, b^*) \to 0 \quad (\eta \to \pm\infty). \tag{5.25}$$

Interestingly, by integrating (5.19) over the η-domain and making use of the boundary condition (5.25), we find that all modes with $\hat{\lambda}_r \neq 0$, including all unstable modes, satisfy

$$\int_{-\infty}^{\infty} |a|^2 \, \mathrm{d}\eta = \int_{-\infty}^{\infty} |b|^2 \, \mathrm{d}\eta \,, \tag{5.26}$$

which suggests that energy is equipartitioned between the two subharmonic wavepackets regardless of mean flow.

To examine the effect of the mean flow on PSI, we use the beam profile

$$Q = \frac{1}{\sqrt{8\pi}} \int_0^{\infty} \mathrm{e}^{-l^2/8} \mathrm{e}^{\mathrm{i}l\eta} \, \mathrm{d}l \,, \tag{5.27}$$

comprised of a superposition of plane waves with positive wavenumber ($l > 0$) and therefore represents a unidirectional, progressive wave beam (Tabaei & Akylas, 2003) that transports energy in the positive ξ-direction (see figure 5-1). Inserting (5.27) into (5.19) and discretizing (5.19) using eighth-order centered finite differences, the resulting matrix eigenvalue problem is then solved for various σ and $\overline{u}$ using standard numerical eigenvalue packages in MATLAB to obtain eigenvalues $\hat{\lambda}(\kappa)$, with boundary conditions (5.25) taken at the edges of the computational domain. We used a typical grid spacing of $\Delta\eta = 0.05$ and domain of $\eta \in [-50, 50]$, although these values varied depending on the parameters σ and $\overline{u}$.

Figure 5-2 plots the eigenvalues $\hat{\lambda}$ as a function of κ for $\sigma = 0$ and $\overline{u} = 0, 0.5$ and -1, as well as the quadratic $\alpha\kappa^2$. Here, it is clear that positive background mean flow ($\overline{u} = 0.5$), in which the mean flow is parallel with the projections of the group and phase velocities onto the horizontal, has a strong stabilizing effect on instability, while negative mean flow ($\overline{u} = -1$) has a much weaker stabilizing effect. It should be noted that if Q is taken to have only negative wavenumbers via the substitution $Q(\eta) \to Q(-\eta)$, representing a wave beam that transports energy in the negative ξ-direction, then via (5.19), the same results hold if the mean flow is accordingly reversed via the substitution $\overline{u} \to -\overline{u}$.

Figure 5-3(a) plots the maximum inviscid PSI growth rates, taken over κ, as a function of the mean flow $-4 \leq \overline{u} \leq 2$ for detuning parameter $\sigma = -4, 0$ and 10. Overall, PSI is almost entirely stabilized for $\overline{u} \gtrsim 1$ and for $\overline{u} \lesssim -4$. Importantly however, for $\sigma = -4$, corresponding to the case when $\omega/2 < f$ and subharmonic perturbations are sub-inertial, negative but small mean flow actually enhances PSI, with the maximum growth rate occurring for $\overline{u} \approx -1$. Furthermore, under viscous flow conditions, shown in figure 5-3(b,c), instability for the

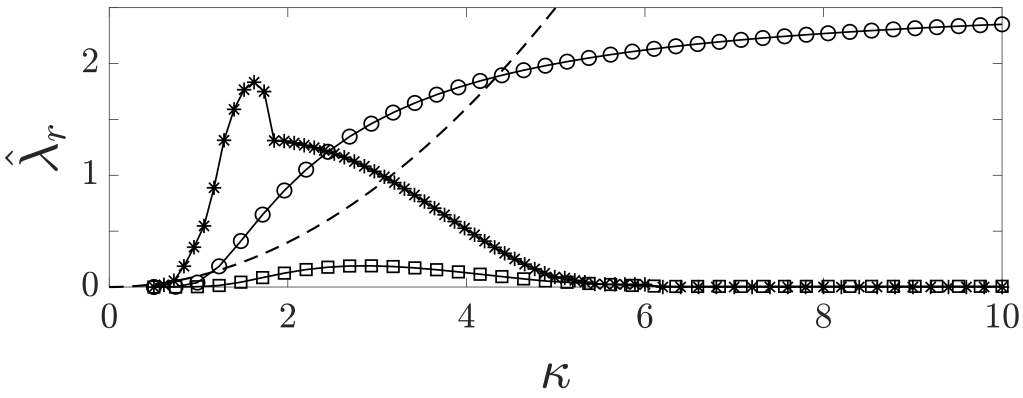

Figure 5-2: Real part of the stability eigenvalues $\hat{\lambda}_r$, corresponding to the inviscid PSI growth rate, for the locally confined beam profile (5.27) as a function of the scaled perturbation wavenumber κ for $\overline{u} = 0$ ($\circ$), 0.5 ($\Box$), and -1 ($*$). The dashed line plots the quadratic $\alpha\kappa^2$ for $\alpha = 0.1$.

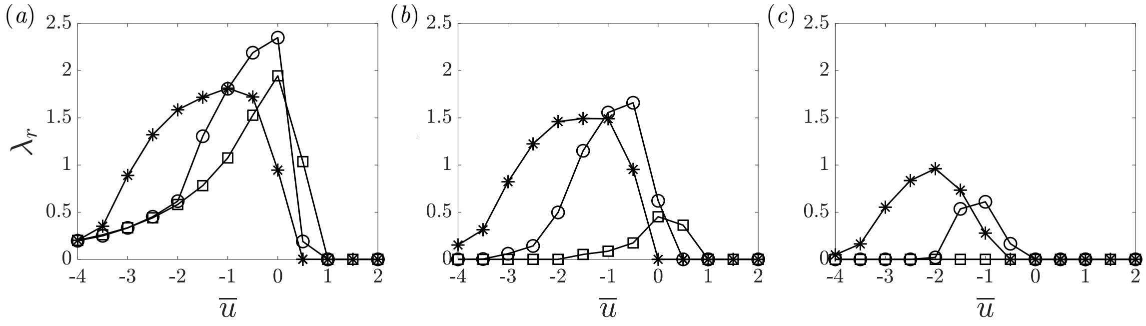

Figure 5-3: (a) Maximum inviscid ($\alpha = 0$) PSI growth rate λ_r for the locally confined beam profile (5.27) as a function of $\overline{u}$ for $\sigma = -4$ ($*$), 0 ($\circ$), and 10 ($\Box$). (b) Same as (a) but for $\alpha = 0.1$. (c) Same as (a) but for $\alpha = 0.5$.

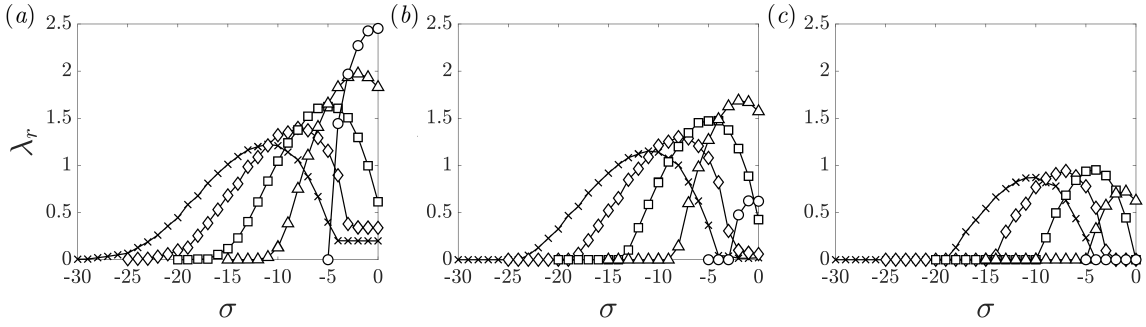

Figure 5-4: (a) Maximum inviscid ($\alpha = 0$) PSI growth rate λ_r for the locally confined beam profile (5.27) as a function of σ for $\overline{u} = 0$ ($\circ$), -1 ($\triangle$), -2 ($\Box$), -3 ($\Diamond$), and -4 ($\times$). (b) Same as (a) but for $\alpha = 0.1$. (c) Same as (a) but for $\alpha = 0.5$.

case of negative detuning and negative mean flow appears to be less susceptible to the stabilizing effects of viscous dissipation. This is because negative mean flow generally shifts the maximum instability growth rate to lower wavenumbers κ, as seen in figure 5-2.

To shed light on the case of negative detuning and negative mean flow, in which instability appears to be strengthened by the addition of mean flow, figure 5-4(a) plots the maximum inviscid PSI growth rate, taken over κ, as a function of $-30 \leq \sigma \leq 0$ for $-4 \leq \overline{u} \leq 0$. Overall, negative mean flow permits PSI far below the critical frequency $\omega = 2f$. This effect is similar to the PSI of a plane wave, where instability depends only on the combined parameter $\sigma' = \sigma - \overline{u}\sqrt{3}$, although for the locally confined beam, growth rates are highest under no mean flow. Under viscous flow conditions (figure 5-4b,c), PSI is stronger for $\overline{u} < 0$ than no mean flow, owing to the complex dependence of the instability eigenvalues on κ (e.g. see figure 5-2). However, it should be noted that although these results suggest that PSI is possible even for $\sigma \lesssim -10$ under the presence of mean flow, the present asymptotic theory is only strictly valid for $|\sigma| = O(1)$.

5.5 Concluding remarks

We have studied the effect of a small background constant horizontal mean flow on the near-inertial PSI of locally confined beams of general profile. To do so, we derived evolution equations for near-inertial perturbations that describe their ability to extract energy from the primary beam under the combined effects of mean flow, detuning, dispersion, and viscosity. Importantly, we find that sufficiently large mean flow in either direction (relative to the primary beam) stabilities PSI. From the results presented in §5.4, our theory suggests that mean flow entire stabilizes PSI when $\overline{u} \approx 1$. Assuming a modest amplitude of $\epsilon = 0.1$ and using $N_* = 10^{-3}$ s^{-1} and $L_* = 500$ m as representative oceanic values, this corresponds to a dimensional mean flow of about 5 cm/s. However, in the special case where the mean flow points antiparallel to the horizontal projection of the group velocity and the primary wave frequency $\omega < 2f$, a small amount of mean flow can strengthen PSI and extend the region of instability to lower frequencies. As a result, PSI may be found away from the critical frequency $\omega = 2f$ depending on the mean flow.

THIS PAGE INTENTIONALLY LEFT BLANK

Chapter 6

Future directions

In this thesis, we have shown that the instability of finite-width internal wave beams, while sharing much fundamental physics with that of idealized sinusoidal waves, manifest in the natural environment in very different ways. We find that in some cases, classical instability mechanisms may not be as important as we think, such as PSI in three-dimensional beams or at the critical latitude in the presence of background mean flows, while they appear in new, unexpected places, such as away from the critical latitude and even without background rotation. At the same time, we find that asymptotic analysis is an extremely powerful tool in studying these nonlinear phenomena, by taking full advantage of the vast arrays of time and length scales that nature has provided us, which continue to astound us with their complexity while surprising us with their simplicity.

However, there is still much work to be done. In Chapter 2, we found that three-dimensional variations, while weakening PSI, may result in other types of instability related to the generation of induced mean flows. These three-dimensional instabilities, which include streaming and a three-dimensional modulational instability, have only recently gained notice and their relevance in the natural environment is still unknown. In Chapter 3, we found that a broadband-type instability dominates over PSI for extremely fine-scale perturbations. Whether this broadband instability can be observed is unclear. In Chapter 4 and 5, we showed that background mean flows generally weaken PSI, but small amounts can actually extend the range of PSI, suggesting that instability could be spread over a range of latitudes around the critical latitude. Since these are theoretical results derived using an asymptotic theory, a comparison with fully numerical simulations, laboratory experiments, or observation is desired. Furthermore, our results assume small mean flow, and so the effect of larger mean flows are unknown, such as in the lee wave regime. It is possible that other types of instabilities befall internal waves in these scenarios.

THIS PAGE INTENTIONALLY LEFT BLANK

Appendix A

Miscellaneous results

A.1 Eigenvalue problem symmetry for locally-confined beam

By eliminating p in (2.6), we obtain

$$v_\eta = -\mathrm{i}(\mu u + mw), \tag{A.1a}$$

$$\rho_t + \mathrm{i}\mu u_0 \rho + v\rho_{0\eta} + u\sin\theta - v\cos\theta = 0, \tag{A.1b}$$

$$\big(u_{\eta\eta} - \mu^2 u - \mu m w\big)_t + (\mathrm{i}\mu u_0 u + v u_{0\eta} - \rho\sin\theta - \nu\mathscr{L}u)_{\eta\eta} - \mathrm{i}\mu\mathbb{F}_\eta = 0, \tag{A.1c}$$

$$\big(w_{\eta\eta} - m^2 w - \mu m u\big)_t + (\mathrm{i}\mu u_0 w - \nu\mathscr{L}w)_{\eta\eta} - \mathrm{i}m\mathbb{F}_\eta = 0, \tag{A.1d}$$

where

$$\mathbb{F} = \mathrm{i}\mu u_0 v + \rho\cos\theta - \nu\mathscr{L}v, \tag{A.2}$$

and $\mathscr{L} = -\mu^2 + \partial^2_{\eta\eta} - m^2$. Because u_0 and ρ_0 are purely real, if $(u, v, w, \rho; \mu, m)$ is a solution to (A.1), then so are $(u, v, -w, \rho; \mu, -m)$, $(u^*, v^*, w^*, \rho^*; -\mu, -m)$, and $(u^*, v^*, -w^*, \rho^*; -\mu, m)$. Therefore, it is sufficient to consider $\mu \geq 0$ and $m \geq 0$ only.

A.2 Nonlinear self-interaction terms with weak mean flow

An internal wave beam with general profile in η and variations in ξ, the along-beam direction orthogonal to η, will generate a mean and higher harmonics owing to nonlinear self-interactions (Tabaei & Akylas, 2003). For a beam with amplitude ϵ and $O(\mu)$ modulations in ξ, nonlinear self-interaction terms due to the Jacobians in (4.1) will be $O(\mu\epsilon^2)$. Therefore, at best, the mean and higher harmonics that arise via these self-interaction terms will have amplitude $O(\mu\epsilon^2)$ and their feedback onto the primary wave beam can only occur over a $O(\mu^{-1}\epsilon^{-2})$ time scale.

The wave beam (4.6) is a specific case of a locally confined beam with general profile in η and $O(\mu)$ modulations in ξ according to (4.5). Therefore, as argued above, nonlinear self-interaction terms can only occur over a $O(\mu^{-1}\epsilon^{-2})$ time scale at best.

Bibliography

Alford, M. H., MacKinnon, J. A., Zhao, Z., Pinkel, R., Klymak, J. & Peacock, T. 2007 Internal waves across the pacific. *Geophys. Res. Lett.* **34** (24).

Bordes, G., Venaille, A., Joubaud, S., Odier, P. & Dauxois, T. 2012 Experimental observation of a strong mean flow induced by internal gravity waves. *Phys. Fluids* **24** (8).

Bourget, B., Dauxois, T., Joubaud, S. & Odier, P. 2013 Experimental study of parametric subharmonic instability for internal plane waves. *J. Fluid Mech.* **723**, 1–20.

Bourget, B., Scolan, H., Dauxois, T., Le Bars, M., Odier, P. & Joubaud, S. 2014 Finite-size effects in parametric subharmonic instability. *J. Fluid Mech.* **759**, 739–750.

Brouzet, C., Sibgatullin, I. N., Scolan, H., Ermanyuk, E. V. & Dauxois, T. 2016 Internal wave attractors examined using laboratory experiments and 3D numerical simulations. *J. Fluid Mech.* **793**, 109–131.

Clark, H.A. & Sutherland, B.R. 2010 Generation, propagation, and breaking of an internal wave beam. *Phys. Fluids* **22** (7), 076601.

Dauxois, T., Joubaud, S., Odier, P. & Venaille, A. 2018 Instabilities of internal gravity wave beams. *Annu. Rev. Fluid Mech.* **50** (1), 131–156.

Ermanyuk, E. V. & Gavrilov, N. V. 2008 On internal waves generated by large-amplitude circular and rectilinear oscillations of a circular cylinder in a uniformly stratified fluid. *J. Fluid Mech.* **613**, 329–356.

Fan, B. & Akylas, T. R. 2019 Effect of background mean flow on PSI of internal wave beams. *J. Fluid Mech.* **869**, R1.

Fan, B. & Akylas, T. R. 2020*a* Finite-amplitude instabilities of thin internal wave beams: experiments and theory. *J. Fluid Mech.* (*sub judice*).

Fan, B. & Akylas, T. R. 2020*b* Instabilities of finite-width internal wave beams: from Floquet analysis to PSI. *J. Fluid Mech.* (*sub judice*).

Fan, B., Kataoka, T. & Akylas, T. R. 2018 On the interaction of an internal wavepacket with its induced mean flow and the role of streaming. *J. Fluid Mech.* **838**, R1.

Fovell, R., Durran, D. & Holton, J. R. 1992 Numerical simulations of convectively generated stratospheric gravity waves. *J. Atmos. Sci.* **49** (16), 1427–1442.

Hazewinkel, J., Van Breevoort, P., Dalziel, S. B. & Maas, L. R. M. 2008 Observations on the wavenumber spectrum and evolution of an internal wave attractor. *J. Fluid Mech.* **598**, 373–382.

Hazewinkel, J. & Winters, K. B. 2011 PSI of the internal tide on a β plane: Flux divergence and near-inertial wave propagation. *J. Phys. Oceanogr.* **41** (9), 1673–1682.

Hibiya, T., Nagasawa, M. & Niwa, Y. 2002 Nonlinear energy transfer within the oceanic internal wave spectrum at mid and high latitudes. *J. Geophys. Res. Oceans* **107** (C11), 3207.

Hurley, D. G. & Keady, G. 1997 The generation of internal waves by vibrating elliptic cylinders. Part 2. Approximate viscous solution. *J. Fluid Mech.* **351**, 119–138.

Jamin, T., Kataoka, T., Dauxois, T. & Akylas, T. R. 2020 Long-time dynamics of internal wave streaming. *J. Fluid Mech.* (*sub judice*).

Johnston, T. M. S., Rudnick, D. L., Carter, G. S., Todd, R. E. & Cole, S. T. 2011 Internal tidal beams and mixing near monterey bay. *J. Geophys. Res.* **116**, C03017.

Jouve, L. & Ogilvie, G. I. 2014 Direct numerical simulations of an inertial wave attractor in linear and nonlinear regimes. *J. Fluid Mech.* **745**, 223–250.

Karimi, H. H. & Akylas, T. R. 2014 Parametric subharmonic instability of internal waves: locally confined beams versus monochromatic wavetrains. *J. Fluid Mech.* **757**, 381–402.

Karimi, H. H. & Akylas, T. R. 2017 Near-inertial parametric subharmonic instability of internal wave beams. *Phys. Rev. Fluids* **2** (7), 074801.

Kataoka, T. & Akylas, T. R. 2013 Stability of internal gravity wave beams to three-dimensional modulations. *J. Fluid Mech.* **736**, 67–90.

Kataoka, T. & Akylas, T. R. 2015 On three-dimensional internal gravity wave beams and induced large-scale mean flows. *J. Fluid Mech.* **769**, 621–634.

Kataoka, T., Ghaemsaidi, S. J., Holzenberger, N., Peacock, T. & Akylas, T. R. 2017 Tilting at wave beams: a new perspective on the St. Andrew's Cross. *J. Fluid Mech.* **830**, 660–680.

Klostermeyer, J. 1991 Two- and three-dimensional parametric instabilities in finite-amplitude internal gravity waves. *Geophys. Astrophys. Fluid Dynamics* **61** (1-4), 1–25.

Lamb, K. G. 2004 Nonlinear interaction among internal wave beams generated by tidal flow over supercritical topography. *Geophys. Res. Lett.* **31** (9).

Lighthill, M. J. 1978 *Waves in Fluids*. Cambridge University Press.

MacKinnon, J. A., Alford, M. H., Sun, O., Pinkel, R., Zhao, Z. & Klymak, J. 2013 Parametric subharmonic instability of the internal tide at 29 °n. *J. Phys. Oceanogr.* **43** (1), 17–28.

MacKinnon, J. A. & Winters, K. B. 2005 Subtropical catastrophe: Significant loss of low-mode tidal energy at 28.9 °. *Geophys. Res. Lett.* **32** (15).

McComas, C. Henry & Bretherton, Francis P. 1977 Resonant interaction of oceanic internal waves. *J. Geophys. Res.* **82** (9), 1397–1412.

Mercier, M. J., Garnier, N. B. & Dauxois, T. 2008 Reflection and diffraction of internal waves analyzed with the Hilbert transform. *Phys. Fluids* **20** (8), 086601.

Mercier, M. J., Martinand, D., Mathur, M., Gostiaux, L., Peacock, T. & Dauxois, T. 2010 New wave generation. *J. Fluid Mech.* **657**, 308–334.

Mied, R. P. 1976 The occurrence of parametric instabilities in finite-amplitude internal gravity waves. *J. Fluid Mech.* **78** (4), 763–784.

Mowbray, D. E. & Rarity, B. S. H. 1967 A theoretical and experimental investigation of the phase configuration of internal waves of small amplitude in a density stratified liquid. *J. Fluid Mech.* **28**, 1–16.

Onuki, Y. & Tanaka, Y. 2019 Instabilities of finite-amplitude internal wave beams. *Geophys. Res. Lett.* **46**, 7527–7535.

Peacock, T., Echeverri, P. & Balmforth, N. J. 2008 An experimental investigation of internal tide generation by two-dimensional topography. *J. Phys. Oceanogr.* **38** (1), 235–242.

Richet, O., Muller, C. & Chomaz, J.-M. 2017 Impact of a mean current on the internal tide energy dissipation at the critical latitude. *J. Phys. Oceanogr.* **47** (6), 1457–1472.

Schatz, M.F., Barkley, D. & Swinney, H. L. 1995 Instability in a spatially periodic open flow. *Phys. Fluids* **7** (2), 344–358.

Scolan, H., Ermanyuk, E. & Dauxois, T. 2013 Nonlinear fate of internal wave attractors. *Phys. Rev. Lett.* **110**, 234501.

Shmakova, N. D. & Flór, J.-B. 2019 Nonlinear aspects of focusing internal waves. *J. Fluid Mech.* **862**, R4.

Sonmor, L. J. & Klaassen, G. P. 1997 Toward a unified theory of gravity wave stability. *J. Atmos. Sci.* **54** (22), 2655–2680.

Staquet, C. & Sommeria, J. 2002 Internal gravity waves: from instabilities to turbulence. *Annu. Rev. Fluid Mech.* **34** (1), 559–593.

Sutherland, B. R. 2013 The wave instability pathway to turbulence. *J. Fluid Mech.* **724**, 1–4.

Sutherland, B. R. & Linden, P. F. 2002 Internal wave excitation by a vertically oscillating elliptical cylinder. *Phys. Fluids* **14** (2), 721–731.

Tabaei, A. & Akylas, T. R. 2003 Nonlinear internal gravity wave beams. *J. Fluid Mech.* **482**, 141–161.

Thomas, N. H. & Stevenson, T. N. 1972 A similarity solution for viscous internal waves. *J. Fluid Mech.* **54**, 495–506.

YEH, K. C. & LIU, C. H. 1981 The instability of atmospheric gravity waves through wave-wave interactions. *J. Geophys. Res.* **86** (C10), 9722–9728.

YOUNG, W. R., TSANG, Y.-K. & BALMFORTH, N. J. 2008 Near-inertial parametric subharmonic instability. *J. Fluid Mech.* **607**, 25–49.